ISSN 1068-3755, Surface Engineering and Applied Electrochemistry, 2009, Vol. 45, No. 5, pp. 353–354. © Allerton Press, Inc., 2009.
Original Russian Text © V.D. Shkilev, A.N. Adamchuk, 2009, published in Elektronnaya Obrabotka Materialov, 2009, No. 5, pp. 4–5.

## ELECTRICAL PRECISION TREATMENT OF MATERIALS

# On the Uniqueness of the Set of Microapertures Obtained by the Electrodischarge Method

**V. D. Shkilev and A. N. Adamchuk**
*Ministry of Informational Development of the Republic of Moldova,*
*ul. Pushkina 42, Chisinau, MD-2012 Republic of Moldova*
*e-mail: schilov@registru.md*

Received March 23, 2009

**Abstract**—The uniqueness of a set of electrodischarge microappertures obtained by means of simultaneous processing of several target layers has been proved experimentally. The applicability of the electrodischarge process as an identification technology has been confirmed.

**DOI:** 10.3103/S1068375509050019

The use of the stochasticity of an electric discharge for the identification of paper documents of special significance [1 and 2] has been based on the idea of their reproduction failure and the uniqueness of the set of microappertures obtained. The experiments performed with various interelectrode gaps and power sources showed [3] that the phenomenon of the electric discharge stochasticity (characterized by the failure of the electric discharge hitting a preset matrix area) provides an irreproducible set of microapertures.

The identification technology requirements are very strict concerning the impossibility of reproduction. If two similar matrices can be produced by some tricks, the technique fails to be recognized as an identification one.

The theoretical probability of the matrix reproduction at individual processing has been estimated as $10^{-400}$. In papers [1 and 3], each matrix was individually processed. There remained one technological "creephole," when there could be processed not single matrices but a "pile" of two or three strictly positioned matrices. The electric discharge hitting all the "pile" at once could provide not a complete copy of the matrix but a very close similarity of the first level matrix (the nearest to the high voltage electrode) with the lower matrix. The presence of such "similar" matrices at a certain nonchalance in the positioning can cast discredit on the electric discharge identification reliability. In this case, each "similar" matrix could discredit a document of special significance and result in irretrievable losses.

The experimental methods remained the same and were almost unchanged as compared to [1]. The distinction consisted in the fact that the electric discharge hit a "pile" of three matrices instead of a single matrix. The results are presented in Figs. 1 and 2.

The following follow from the obtained results:

—The experiments proved the impossibility of the microaperture set matrix being copied by the method of simultaneous hitting of several layers with the help of electrodischarge identification.

—There were obtained significant distinctions (both in the number of microapertures of each of the layers and in their form) of the matrices.

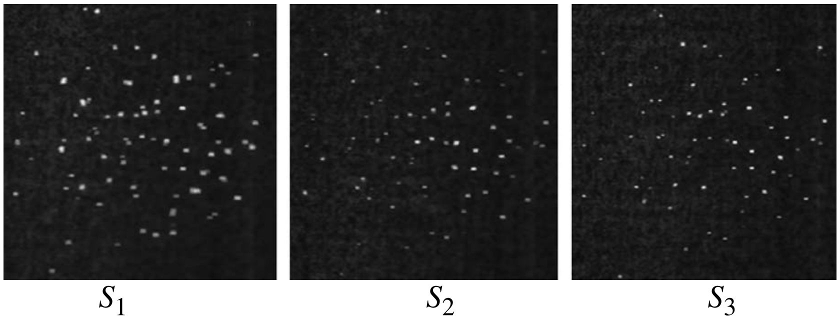

**Fig. 1.** Matrices obtained at the simultaneous hitting of three layers. $S_1$—the matrix nearest to the high voltage electrode.

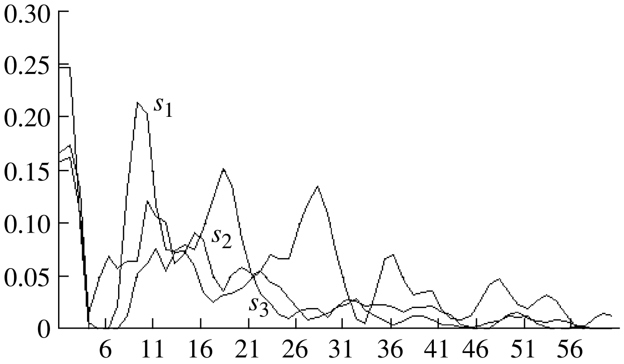

**Fig. 2.** The dependence of the relative density of the apertures in each layer.

—The divergence in a set of microapertures at different layers of a matrix can be explained by the additional “unpredictability” of the surface discharges passing between the layers.

## REFERENCES

1. Shkilev, V.D., Adamchuk, A.N., and Nedioglo, V.G., Electrodischarge Protection Technology of Special Significance Documents (of strict accounting), Surf. Eng. Appl. Electrochem., 2008, no. 2, pp. 4–10.
2. Shkilev, V.D. et al., MD Patent 3389, BOPI, 2007, no. 8, p. 51.
3. Shkilev, V.D., and Adamchuk, A.N., On New Approaches in Data Base Formation on Identification Marks, Obtained by Electrodischarge Method, Surf. Eng. Appl. Electrochem., 2009, no. 2, pp. 4–8.

*ISSN 1068-3755, Surface Engineering and Applied Electrochemistry, 2009, Vol. 45, No. 5, pp. 355–356. © Allerton Press, Inc., 2009.*
*Original Russian Text © A.I. Marinin, 2009, published in Elektronnaya Obrabotka Materialov, 2009, No. 5, pp. 6–8.*

## ELECTRICAL SURFACE TREATMENT METHODS

# High-Voltage Influence of an Electrical Discharge on the Durability of an Electrical Rod Conductor

**A. I. Marinin**
*National University of Food Technologies, ul. Vladimirskaya 68, Kiev, 01033 Ukraine*
*e-mail: a_marinin@ukr.net*

Received June 20, 2009

**Abstract**—Dissipation of energy regimes with the electric discharges have been considered, Dissipation of energy effect the deformed-stressed condition of the conducting road, and thus, determines its strenght and resources.

**DOI:** 10.3103/S1068375509050020

Designing reliable installations is connected with forecasting the durability of technical systems and revealing the qualitative and quantitative laws that depend on the behavior of the load or some conditions.

In the present publication, the regime of influence of the energy dissipation at the electrocategory in liquid on the mechanical stress change and the definition of the safety factor in electrical rod conductors of electrode systems of electrohydraulic installation is considered (EGI).

The electrical rod conductor represents a cylinder [1]. Its stress is defined by the dynamics of the electrocategory channel and following it the gas and steam space.

Let's consider the deformation of an electrical rod conductor by the plasma stress $P_a(t)$ of cylindrical channel radius $r_k(t)$. Let us accept $P_a(t)$ distributed in regular intervals on all the volume of the channel [2–4] so that the stress $\sigma(t)$ in the longitudinal loaded electrical rod conductor will be estimated according to the following formula:

$$\sigma(t) = \frac{P_a(t)\pi r_k^2(t)}{S_0}, \qquad (1)$$

where $S_0$ is the sectional area of the rod.

The regimes of the dissipation of the energy at the electrocategory is characterized by the size of the share allocated in the first half-cycle of the electrocategory $\xi$. Thus, the coupling between the varied parameters EGI and $\xi$ is defined in the monography [3]:

$$\xi^3 = \frac{\pi A L_\mathrm{p}^2}{U^2\sqrt{LC}}, \qquad (2)$$

where $A = 0.25\ \mathrm{B}^2\ \mathrm{c/m}^2$ is the lightning constant, $L_\mathrm{p}$ is the length of the interelectrode interval, $U_0$ is the stress on the condenser batteries coating of capacity $C$, $L$ is the inductance of the discharge resistor circuit, and $\xi = 0.44$ at the oscillatory regime of the energy dissipation.

The dissipation of the energy regimes of the electroexplosion affects the parameters of the intensely deformed condition of the electrical rod conductor and thus its resources and durability. It is possible to define $\mathrm{L_p}$ as the length of the digit interval from equation (2).

Taking into account Hooke's law, from formula (1), let us define the maximum permissible diameter of the electrical rod conductor $D_\mathrm{pr}$, whose reduction leads to deformations exceeding the limit of proportionality $\varepsilon_\mathrm{pr}$:

$$D_\mathrm{pr} \geq \sqrt{\frac{4P_a(t)r_k^2(t)}{E\varepsilon_\mathrm{pr}}}, \qquad (3)$$

where $E$ is Young's modulus of the rod material.

In the present publication, in comparison [2–4], the equation for the definition of the safety factor that exceeds the proportionality limit is established.

At the first approximation, we consider that the channel radius $r_k$ is equal to an edge with the rounding off radius $r_1$ (with account for the streamer increase) [5].

Then, from formula (1), it follows that

$$\sigma(t) = P_a(t)\frac{r_1^2}{R_1^2} = P_a(t)\frac{d_1^2}{D_1^2}, \qquad (4)$$

where $d_1 = \sqrt{\frac{4FK}{\pi\sigma_T}}$; and $D_1 = \sqrt{\frac{4FK}{\pi\sigma_{-1}}}$.

At this point, $K$ is the assurance factor, $F$ is the resultant force, $\sigma_T$ is the yield point of the metal, $\sigma_{-1}$ is the fatigue resistance, and $D_1$ is the diameter of the electrical rod conductor $r_1 = \frac{d_1}{2}$.

The core ratio is

$$\frac{d_1^2}{D_1^2} = \frac{\sigma_{-1}}{\sigma_T}. \qquad (5)$$

Then, from (4), we get

$$\sigma(t) = Pa(t)\frac{\sigma_{-1}}{\sigma_T}. \qquad (6)$$

The admissible stress $[\sigma] = \sigma_{\text{pr}}/K$, where $\sigma_{\text{pr}}$ is the limit stress in the case of plastic $[\sigma] = \frac{\sigma_T}{K_T}$.

At the first approximation, it is possible to consider that

$$\sigma(t) = P_a(t)\frac{K_{\text{fatique}}}{K_T}. \qquad (7)$$

This means that, for one regime, the fatigue strength is the limiting condition of the durability and, for others, it is the yield point.

The assurance factor according to the plastic yield is [5]

$$K_T = \frac{\sigma_T}{(\sigma_a + \sigma'_{\text{av}})}, \qquad (8)$$

where $\sigma'_a = \frac{\sigma_{\max} - (-\sigma_{\min})}{2}$; and $\sigma'_{\text{av}} = \frac{\sigma_{\max} + (-\sigma_{\min})}{2}$.

The development of an electric spark in time occurs by consecutive streamers' "germination" in the interelectrode interval. As a rule, the growing streamer consists not of one but of many channels with numerous branches from it. In the course of the streamers growth, a great bulk of those gaseous products from the gasvapor "shirt" of the electric spark channel is formed.

The stages of the graded development of the streamer germination have the basic processes for the moment IV–VI of the stages.

The range of the stress and the average stress are defined according to the stages of the development of the growing streamer [6] according to formula (1).

For IV stage—$\sigma_{\min}$, for VI stage—$\sigma_{\max}$.

The safety factor according to the fatigue is

$$K_{\text{fatigue}} = \frac{\sigma_{-1}}{(\sigma'_a/\varepsilon + \varphi_\sigma\sigma'_{\text{av}})}, \qquad (9)$$

where $\varphi_\sigma < 1$ is the factor of the supposed stress reduction, $\varepsilon$ is the fatigue strength, and $\varepsilon \geq 1$ at $D_1 \geq 10$ (tabular data).

From the comparison of the received safety factors, it is possible to define exactly what is more dangerous: either the breakage of the electrical rod conductor or the occurrence of plastic deformations with the deformations exceeding the strength $\varepsilon_{\text{pr}}$.

When $K_T < K_{\text{fatigue}}$, plastic deformations occur; otherwise, the approaching of the breakage of the electrical rod conductor takes place. The regime of energy dissipation from the electroexplosion differently affects the parameters of the intensely deformed condition of the electrical rod conductor and so its amount of durability.

Thus, it is necessary to consider thermal erosion to be the basic mechanism of the tip deterioration, whereby some volume of the electrode material burns off and the plasma stress deletes the fused electrolyte from the electropad and, as a result, the coverage of the discharge filament.

## REFERENCES

1. Gulyi G.A, Malyushevskii A.P., *Elektricheskii razryad v silovyh impulsnyh sistemah* Kiev: Nauk. dumka, 1977, p. 275.
2. Okun I.Z., *Issledovanie electricheskih haracteristic impulsnogo razryada v zhidkosti*, Physicists technical journal, 1969. 39. no 5. p. 850–867.
3. Krivitskii E.V., Shamko V.V., *Perehodnye protsessy pri vysokovoltnom razryade v vode,* Kiev: Nauk. dumka, 1980, p. 207.
4. Naugolnyh K.A., Roi N.A., "*Electricheskie razryady v vode"* Moscow: Nauka, 1971. p. 155.
5. Kinasoshvili R.S., *Soprotivlenie materialov,* Moscow: Nauka, 1975. p. 384.
6. Yutkin L.Ya., *Elektrogidravlicheskii effect i ego primenenie v promyshlennosti,* Leningrad, Mashonostroenie, Leningrad office, 1986, p. 253.

ISSN 1068-3755, Surface Engineering and Applied Electrochemistry, 2009, Vol. 45, No. 5, pp. 357–363. © Allerton Press, Inc., 2009.
Original Russian Text © S.O. Shiryaeva, A.I. Grigor'ev, 2009, published in Elektronnaya Obrabotka Materialov, 2009, No. 5, pp. 9–17.

## ELECTRICAL PROCESSES IN ENGINEERING AND CHEMISTRY

# On Stabilization of Capillary Instability of Dielectric Liquid Jet by Volume Electric Charge

**S. O. Shiryaeva and A. I. Grigor'ev**
*Yaroslavl State University, Sovetskaya ul. 14, Yaroslavl, 150000 Russia*
*e-mail: shir@uniyar.ac.ru*

Received April 13, 2009

**Abstract**—The dispersion equation is analyzed for axisymmetric capillary waves at the surface of a volumetrically charged cylindrical jet of ideal incompressible dielectric liquid. It is shown that, for liquids of minor dielectric permittivity, there is the possibility of total stabilization of the jet capillary instability by means of volume electric charge.

**DOI:** 10.3103/S1068375509050032

## INTRODUCTION

The phenomenon of instability of a liquid charged surface resulting in the ejection of strongly charged jets by an unstable surface, disintegrating into separate drops in a polydisperse mode at a nonlinear stage of realization of the phenomenon, has been studied by a great number of experimental and theoretical investigations in connection with numerous academic, technical, and technological supplements (see, e.g., the reviews and monographs [1–12]) which analyze the state of investigations in various spheres of application of the phenomenon in question. Despite the abundance of theoretical and experimental studies on exploration of the instability of a moving liquid jet and the phenomenon of the jet's disintegration into separate drops, many aspects in the physics of the occurring processes are still unknown and continue to attract the attention of scientists.

## PROBLEM FORMULATION

Suppose there is an infinite cylindrical jet of ideal incompressible liquid moving along the symmetry axis at a constant rate $U_0$ with a mass density ρ, dielectric permeability $\varepsilon_{in}$, and a coefficient of surface tension σ, with a radius $R$. The environment surrounding the jet is characterized by the dielectric permeability $\varepsilon_{ex}$ and a negligibly small mass density. Let us assume that the jet is charged, and that, in the framework of the model of a "frozen-in" charge, it is distributed homogeneously in the volume of μ density, with the charge $\eta \equiv \pi R^2\mu$ falling within a unit length of the jet.

Since in the present paper a finite jet is considered, then, in order to simplify the problem, let us pass to the inertial coordinate system, which moves together with the jet at the same rate of $U_0$. It is evident that, in such a coordinate system, the field of the rates of the liquid flowing in the jet $U(r, t)$ can be totally determined by the possible (e.g., having a thermal nature) capillary oscillations of its surface and is a value of the same infinitesimal order as the amplitude of oscillations. We shall seek the critical conditions of implementation of instability of capillary oscillations of such a jet surface.

All the calculations are to be performed in the cylindrical coordinate system with the $OZ$ axis coinciding with the jet symmetry axis, ort $n_z$ of which is directed along the rate vector $U_0$. In dimensionless variables where the jet radius $R$, liquid density ρ, and the coefficient of surface tension σ are used as the main scales ($R = \rho = \sigma = 1$), the equation of the free surface of the jet exposed to random oscillations of small amplitude can be written as

$$r = 1 + \varepsilon\xi(\varphi, z, t);$$

where ε is the oscillation amplitude ($\varepsilon \ll 1$), and $\xi(\varphi, z, t)$ is the disturbance of the jet surface $|\xi(\varphi, z, t)| \sim 1$ caused by the capillary waves at its surface.

The mathematical formulation of the problem for calculating capillary oscillations of the jet consists of the equations of hydrodynamics and electrostatics (on the assumption that the rate of the liquid motion is far less than the relativistic one):

$$\frac{\partial U}{\partial t} + (U \cdot \nabla)U = -\frac{1}{\rho}\nabla p; \quad divU = 0.$$

$$\Delta\Phi^{in} = -4\pi\frac{\mu}{\varepsilon_{in}}, \quad \Delta\Phi^{ex} = 0,$$

with boundary conditions

$$r = R + \xi: \frac{dF}{dt} = 0, \quad F(r, \varphi, z, t) = r - (1 + \varepsilon\xi(\varphi, z, t)) = 0;$$

$$-(P - P_{atm}) + \operatorname{div}\vec{n} - P_q = 0, \quad \Phi^{in} = \Phi^{ex};$$

$$\varepsilon_{in}\vec{n} \cdot \nabla\Phi_{in} = \varepsilon_{ex}\vec{n} \cdot \nabla\Phi_{ex};$$

$$r \longrightarrow 0\colon \Phi^{\text{in}} \longrightarrow 0; \quad |\mathrm{U}| < \infty;$$

$$r \longrightarrow \infty\colon \Phi^{\text{ex}} \longrightarrow 0.$$

$P_{\text{atm}}$ is the atmospheric pressure; $U(r, t)$ and $P(r, t)$ are the field of velocities and the field of pressures inside the jet; $P_q$ is the electrostatic field pressure on the jet surface; and $\Phi^{\text{in}}$ and $\Phi^{\text{ex}}$ are the electric potentials inside and outside the jet, respectively.

Besides the written conditions, it is necessary to fulfill the requirement of constancy of the jet segment volume, the length of which equals the wavelength $\lambda$:

$$\int\limits_{z_0}^{z_0+\lambda}\int\limits_{0}^{1+\xi}\int\limits_{0}^{2\pi} dzrdrd\varphi = \pi\lambda.$$

## DISPERSION EQUATION

The solution of the formulated problem can be presented as

$$\begin{aligned}
&\xi(\varphi, z, t) = C_1\exp[i(kz - \omega t + m\varphi)];\\
&\psi(\vec{r}, t) = C_2 I_m(kr)\exp[i(kz - \omega t + m\varphi)];\\
&\Phi_{\text{in}}(\vec{r}, t) = C_{3(2)} I_m(kr)\exp[i(kz - \omega t + m\varphi)];\\
&\Phi_{\text{ex}}(\vec{r}, t) = C_4 K_m(kr)\exp[i(kz - \omega t + m\varphi)].
\end{aligned} \tag{1}$$

$I_m(k)$ and $K_m(k)$ are modified Bessel functions of the first and second kind; $m$ is an azimuthal parameter. Omitting the procedure of finding the solution in detail described in [9, 10], let us write straightforwardly the dispersion equation of the problem for axisymmetric waves [9]:

$$\begin{aligned}
&\omega^2 = g(k)[k^2 - 1 + WF(k, \varepsilon_{\text{in}}, \varepsilon_{\text{ex}},)];\\
&F(k, \varepsilon_{\text{in}}, \varepsilon_{\text{ex}}) \equiv \frac{1}{(\varepsilon_{\text{in}} g(k) - \varepsilon_{\text{ex}} h(k))\varepsilon_{\text{in}}\varepsilon_{\text{ex}}}[(\varepsilon_{\text{in}} - \varepsilon_{\text{ex}})^2\\
&\quad \times g(k)h(k) + \varepsilon_{\text{in}}(\varepsilon_{\text{in}} - \varepsilon_{\text{ex}})g(k)\\
&\quad + 3\varepsilon_{\text{ex}}(\varepsilon_{\text{in}} - \varepsilon_{\text{ex}})h(k) + 4\varepsilon_{\text{in}}\varepsilon_{\text{ex}}];\\
&W \equiv \pi\mu^2 \equiv \eta^2/\pi; \quad g(k) \equiv kI_1(k)/I_0(k);\\
&h(k) \equiv -kK_1(k)/K_0(k).
\end{aligned} \tag{2}$$

Here, it should be noted that the charge parameter $W$ is determined as the ratio of the jet surface pressure of the electric field of self-charge to the pressure of the boundary tension forces under its cylindrical surface. Since $W$ is expressed through the charge falling within a unit length of the jet, and the mathematical formulation of the problem comprises no physical characteristics of the charge transfer, the obtained dispersion equation can also be used for investigation of waves at a homogeneously charged surface of an ideally conducting jet when performing the passage to the limit $\varepsilon_{\text{in}} \longrightarrow \infty$ in the dispersion equation.

## ANALYSIS OF RESULTS

As follows from the dispersion equation (2), when its right-hand side is positive, the frequencies are real and the axisymmetric waves at the jet surface are stable. If the right-hand side of the dispersion equation is negative, the frequencies $\omega_{1,2}$ become imaginary complex conjugate ones. To the imaginary solution of the dispersion equation with a "plus" in front of the imaginary unit according to (1) will correspond a solution exponentially increasing with time. In connection with all that was mentioned above, the analysis of the possibility of jet stabilization may be carried out on the basis of the dispersion equation.

The function $g(k)$ used as a multiplier on the right-hand side of the dispersion equation is always positive [8]. In the absence of electrical charge at the jet (at $W = 0$) in accordance with the general theory of capillary instability of the jet [11], which results in its disintegration into separate drops under the action of capillary forces, the dispersion equation has imaginary solutions within the range of the wave numbers $0 \le k < 1$. At $W \ne 0$, the sign of the right-hand side of the dispersion equation will be determined by the function $F(k, \varepsilon_{\text{in}}, \varepsilon_{\text{ex}})$ standing as a multiplier for the parameter $W$. In the region of values of physical parameters, where $F(k, \varepsilon_{\text{in}}, \varepsilon_{\text{ex}}) < 0$, the charge of the jet will destabilize it, which leads to the range extension of the wave numbers corresponding to unstable waves and to the increase in instability increments [8, 10]. In the region of values of physical parameters where $F(k, \varepsilon_{\text{in}}, \varepsilon_{\text{ex}}) > 0$, the charge of the jet will stabilize it, leading to reduction of the range of wave numbers corresponding to unstable waves and the decrease of instability increments [8, 10].

## CAPILLARY-ELECTROSTATIC AND ELECTROSTATIC-CAPILLARY INSTABILITIES OF JETS

In Fig. 1 are presented $F(k)$ dependences calculated according to (2) at $\varepsilon_{\text{ex}} = 1$ and various values of $\varepsilon_{\text{in}}$. The two upper curves are calculated for liquid helium and liquid hydrogen, respectively, and the rest of the curves refer to abstract liquids with specified dielectric permeabilities. It is easy to see that, in the wide range of dielectric permeability values of the liquid $\varepsilon_{\text{in}}$ for long waves (small $k$), the function $F(k) > 0$, and for short waves (large $k$), it is $F(k) < 0$. More detailed information on the jet stability of liquids with various dielectric permeabilities $\varepsilon_{\text{in}}$ at different values of the electric charge falling within a unit length of the jet (at various $W$), one can obtain from the curves the dependences of wave frequency squared $\omega^2$ on the wave number which are presented in Figs. 2 and 3.

In Figs. 2a and 2b, one can see the dependences of the square of capillary wave frequency at the surface of a liquid helium jet $\varepsilon_{\text{in}} = 1.048$ (a) and liquid hydrogen $\varepsilon_{\text{in}} = 1.23$ (b) on the wave number calculated at various values of the electric charge falling within a unit length

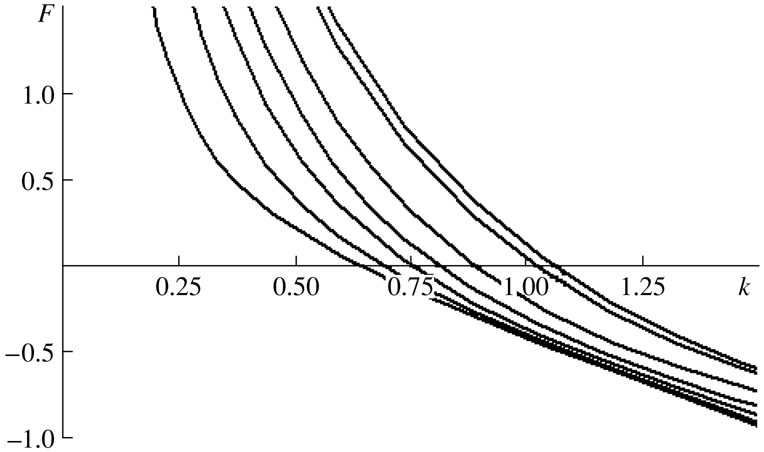

**Fig. 1.** Dependence of $F(k)$ plotted at $\varepsilon_{ex} = 1$ and different values of $\varepsilon_{in}$ (from top to bottom): $\varepsilon_{in} = 1.048$; $\varepsilon_{in} = 1.23$; $\varepsilon_{in} = 2.5$; $\varepsilon_{in} = 5$; $\varepsilon_{in} = 10$; $\varepsilon_{in} = 25$; $\varepsilon_{in} = 80$.

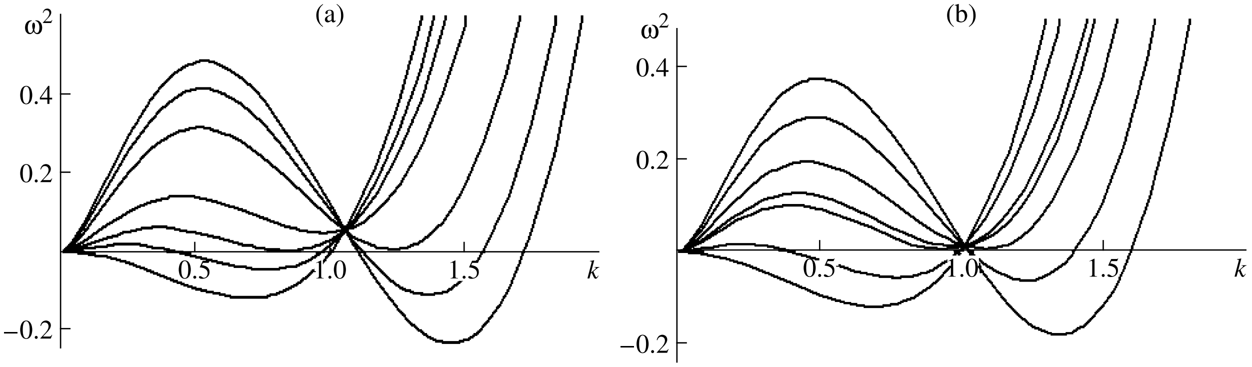

**Fig. 2.** (a) Dependence of the square of the wave frequency on the wave number calculated for liquid helium at $\varepsilon_{ex} = 1$ and various parameters of $W$ (from the bottom upward along the left side): $W = 0$; $W = 0.35$; $W = 0.615$; $W = 1$; $W = 1.77$; $W = 2.2$; $W = 2.5$; (b) Dependence of the square of the wave frequency on the wave number calculated for liquid hydrogen at $\varepsilon_{ex} = 1$ and various parameters of $W$ (from the bottom upward along the left side): $W = 0$; $W = 0.35$; $W = 0.87$; $W = 1$; $W = 1.33$; $W = 1.8$; $W = 2.2$.

of the jet (of parameter $W$). The calculations show that all the curves with $W \neq 0$ enter the origin of coordinates from above at the side of positive values of $\omega^2$, and only the curve corresponding to the uncharged jet ($W = 0$) enters the origin of coordinates from below. From Fig. 2, it is evident that, with an increase in parameter $W$ starting with the value $W = 0$, the zone of values of wave numbers $0 \leq k < 1$, in which the axisymmetric waves undergo capillary instability at $W = 0$, decreases, starting mainly from the left-hand end of the range $0 \leq k < 1$, shifting to the right-hand end, which slightly shifts toward the zone distribution. The value of the increment of wave instability, determined by the depth of the minimum on the curves, decreases in this case. At $W = 0.615$ for liquid helium (see Fig. 2a) and at $W = 0.87$ for liquid hydrogen (see Fig. 2b), the whole curve $\omega^2 = \omega^2(k)$ turns out to be in the upper positive half-plane $\{k, \omega^2\}$, and in the interval of wave number values $0 \leq k \leq 1$, the negative values of $\omega^2$ vanish. This means that, at such values of the charge parameter, there occurs complete stabilization of the liquid helium and liquid hydrogen jets by means of the volume electric charge.

There naturally arises a question concerning the jet behavior at a further increase in the charge parameter $W$ (of the volume electric charge). One can find the answer to the question in Figs. 2a and 2b. It is easy to see that, with $W$ growth at $W > 0.615$ for liquid helium (see Fig. 2a) and at $W > 0.87$ for liquid hydrogen (Fig. 2b), the dependence curve $\omega^2 = \omega^2(k)$, which lies in the upper half-plane, is deformed–there appears a bend point at it to the right of the $k = 1$ point. The left segment (with respect to the bend point) of the curve bends upward and the right one bends downward, so two extremes occur: the maximum is to the left of the bend point and minimum is to the right of it. For liquid helium at $W = 1.77$ and for the liquid hydrogen at $W = 1.33$, the minimum at the curve touches the $x$ axis at points $k \approx 1.24$ and $k \approx 1.16$, respectively. With a further increase in parameter $W$, the curve $\omega^2 = \omega^2(k)$ descends to the region of negative values of $\omega^2$; i.e., there again

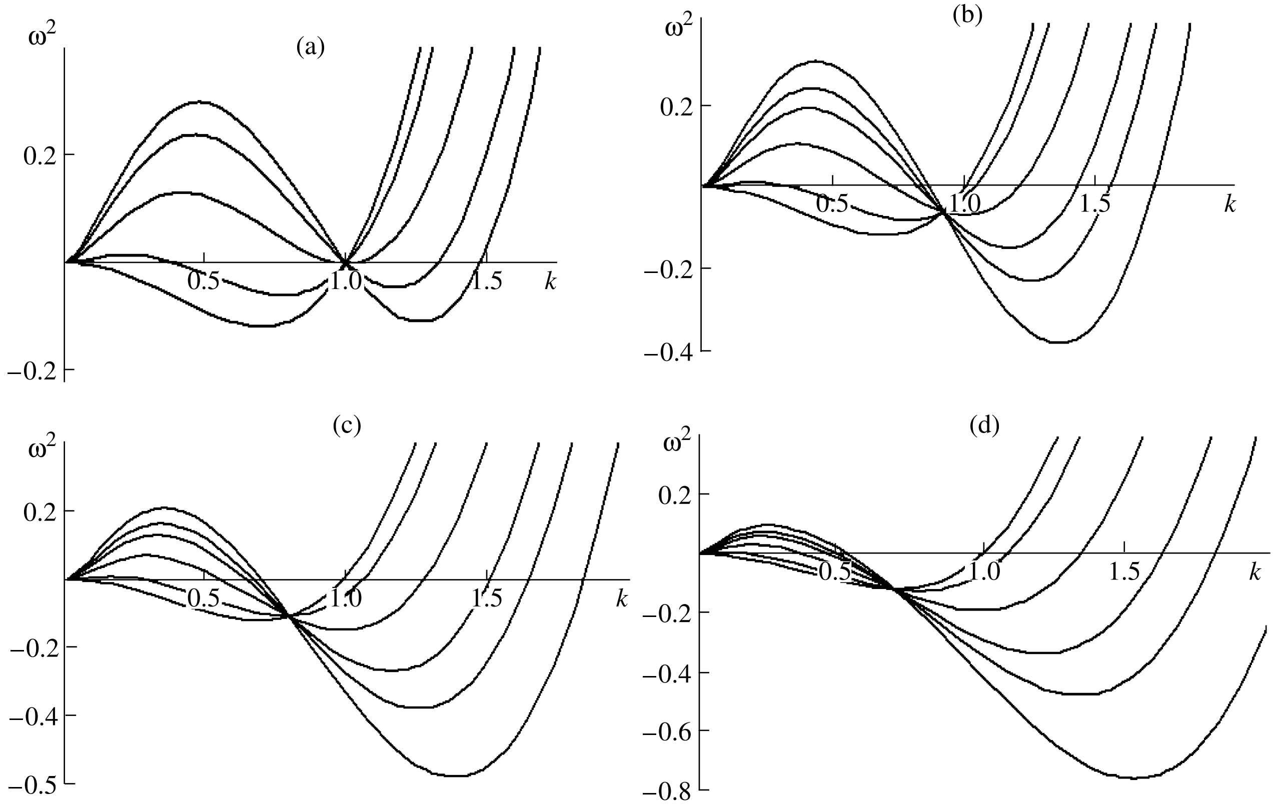

**Fig 3.** (a) Dependence of the square of the wave frequency on the wave number calculated for the liquid with $\varepsilon_{in} = 1.32$ at $\varepsilon_{ex} = 1$ and various parameters of $W$ (from the bottom upward along the left side): $W = 0$; $W = 0.35$; $W = 1.05$; $W = 1.6$; $W = 1.9$; (b). Dependence of the square of the wave frequency on the wave number calculated for the liquid with $\varepsilon_{in} = 2$ at $\varepsilon_{ex} = 1$ and various parameters of $W$ (from the bottom upward along the left side): $W = 0$; $W = 0.35$; $W = 1.05$; $W = 1.6$; $W = 1.9$, $W = 2.3$; (c) The same dependences as in Fig. 3b, but calculated for the liquid with $\varepsilon_{in} = 5$; (d) The same dependences as in Fig. 3b, but calculated for the liquid with $\varepsilon_{in} = 25$.

occur unstable waves. Thus, the liquid helium jets at $W > 1.77$ and the ones of liquid hydrogen at $W > 1.33$ become again unstable and will disintegrate into drops mainly by the electrostatic forces. Note that the sizes of drops determined by the axisymmetric capillary wave with the maximal value of instability increment (by the wave number corresponding to the position of the minimum) will be smaller than at realization of capillary-electrostatic instability [8] attained at $W < 0.615$ for liquid helium and at $W < 0.87$ for liquid hydrogen. In the ranges of the jet charge values of $0.615 \leq W \leq 1.77$ for liquid helium and $0.87 \leq W \leq 1.33$ for liquid hydrogen, the jet will be stable to any small axisymmetric wave deformations; i.e., full stabilization of the capillary instability of the jet by the electric charge will occur. It is natural to refer to the instability of the jets within the range of $W$ parameter values satisfying the conditions of $W > 1.77$ for liquid helium and $W > 1.33$ for liquid hydrogen as an electrostatic-capillary one [8]. From Figs. 2a and 2b and Figs. 3a and 3b, it can be seen that the range of values of the charge parameter $W$ (where the complete stabilization of the dielectric liquid jet by means of the volume electric charge takes place) decreases with the increase in dielectric permeability of the liquid $\varepsilon_{in}$, and at $\varepsilon_{in} = 1.32$, it degenerates to the point $W = 1.05$ (see Fig. 3a). At $\varepsilon_{in} = 1.32$ and $W = 1.05$, the curve $\omega^2 = \omega^2(k)$ lies entirely over the $x$ axis and touches it at the point $k = 1$. At $\varepsilon_{in} = 1.32$ and at any other values of the charge parameter $W \neq 1.05$, there are negative values of $\omega^2(k)$, corresponding to unstable waves. At $\varepsilon_{in} = 1.32$, the bend point on the set of curves $\omega^2 = \omega^2(k)$, corresponding to various $W$, lies on the $x$ axis (see Fig. 3a), and at $\varepsilon_{in} > 1.32$, the bend point shifts to the lower half-plane, to the region of negative values of $\omega^2(k)$ and $k < 1$ (see Figs. 3b and 3c): the value of such a shift to the bottom and to the left increases with increasing liquid dielectric permeability. From Figs. 3b and 3c, it is clear that, in the region $\varepsilon_{in} > 1.32$ with an increase in the $W$ parameter value, the range of wave numbers corresponding to unstable waves expands due to its shifting to the right, into the large $k$ region, but its left boundary also shifts to the right from the point $k = 0$. As a result, the region of values of the wave numbers in the vicinity of the $k = 0$ point, where $\omega^2(k) > 0$ and stabilization of the capillary instability takes place, grows with the increase in the charge parameter $W$. The dielectric permeability increase of the liquid decreases the width of the stabilization region, as is seen from Figs. 3b–3d plotted with similar

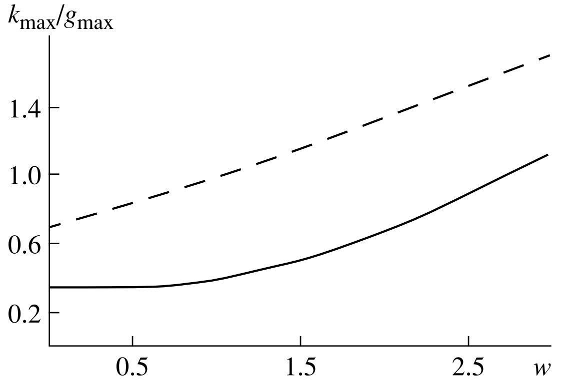

**Fig. 4.** Dependences of the wave number with the maximum increment of the wave (dashed line) on the charge parameter $W$ calculated at $\varepsilon_{\text{ex}} = 1$ for the liquid with $\varepsilon_{\text{in}} = 7$.

sets of values of the $W$ parameter, but with different dielectric permeabilities $\varepsilon_{\text{in}}$.

From Fig. 3, one can see that the increase in the parameter $W$ and liquid dielectric permeability $\varepsilon_{\text{in}}$ causes the growth of the maximum increment of instability (determined by the position of the minimum of the dependence $\omega^2 = \omega^2(k)$) and the wave number of the most unstable mode. The increase in the maximum increment of instability and the wave number of the most unstable mode with the increase in the charge parameter $W$ at a fixed value of $\varepsilon_{\text{in}}$ has been defined by a special calculation, the results of which are presented in Fig. 4.

Figures 5a and 5b illustrate the dependence of positions of the left and right boundaries of the instability region in the space of parameter values $\{k, \varepsilon_{\text{in}}, W\}$. The left boundary of the instability region corresponds to transition of the dependence $\omega^2 = \omega^2(k)$ from the region of positive values to the region of negative values. The right boundary of the instability region, on the contrary, corresponds to transition of the dependence $\omega^2 = \omega^2(k)$ from the region of negative values to the region of positive values. From Fig. 5a, it is evident that the value of $W = W_*$ (critical for the transition to the region of negative values) increases with the increase in wave number $k$ and with the growth of liquid dielectric permeability $\varepsilon_{\text{in}}$. According to Fig. 5b, the value of $W = W_*$ (critical for the transition to the region of positive values) increases with the increase in wave number $k$, but weakly decreases with the increase in dielectric permeability of the liquid $\varepsilon_{\text{in}}$.

From all the aforementioned, it follows that small electric charges at the jet stabilize it. Evidently, it is this phenomenon that was observed initially in the experimental study of the jet charging influence on its capillary instability [13, 14].

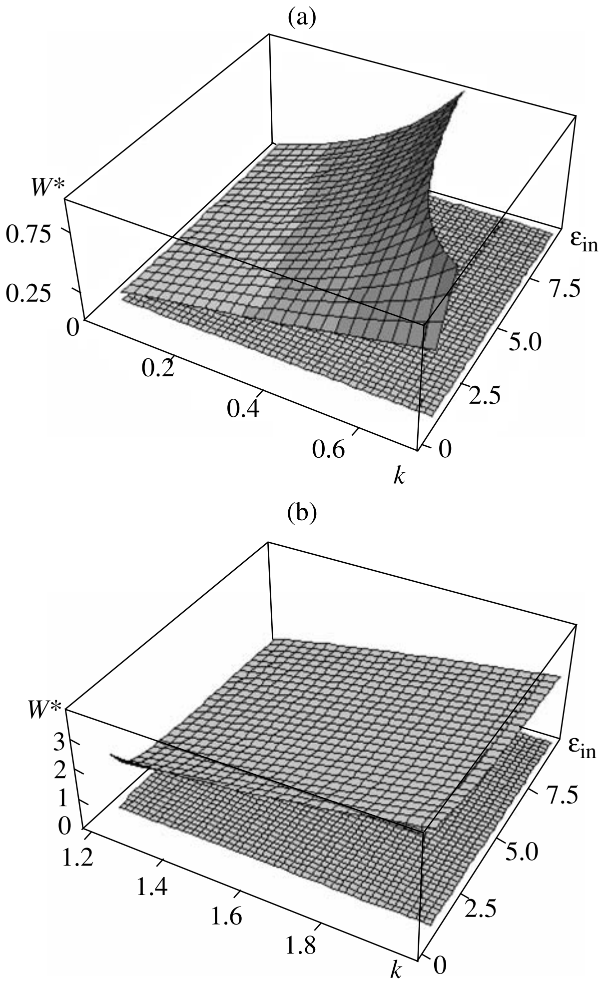

**Fig. 5.** (a) The connection between parameters $W$, $k$, and $\varepsilon_{\text{in}}$ which determine at $\varepsilon_{\text{ex}} = 1$ the position of the instability zone left boundary. The lower, more thickly crosshatched, plane indicates the level of $W = 0$; (b) The connection between parameters $W$, $k$, and $\varepsilon_{\text{in}}$ which determine at $\varepsilon_{\text{ex}} = 1$ the position of the instability zone right boundary. The lower, more thickly crosshatched, plane indicates the level of $W = 0$.

## LIMITATIONS CONNECTED WITH BREAKDOWN PHENOMENA

Large values of parameter $W$ corresponding to the development of electrostatic-capillary instability urge one to consider the question of the possibility of practical realization of such a phenomenon under real conditions, when at sufficiently high intensities of the electrostatic field at a surface jet in the environment, breakdown phenomena may be generated [15–17]. Let us examine this issue more thoroughly.

In the dimensional form, the parameter $W$ is written as follows:

$$W \equiv \pi\mu^2 R^3/\sigma. \tag{3}$$

The intensity of the electrostatic field at the surface of a volumetrically charged finite cylinder with the charge density $\mu$ and radius $R$ is found to be determined as

$$E \equiv 2\pi\mu R. \qquad (4)$$

Substituting (4) into (3), we obtain

$$W \equiv E^2 R / 4\pi\sigma. \qquad (5)$$

Let now parameter $W$ for the jet have a certain fixed value: $W = W_*$. Then from (5), it is easy to find a corresponding value of intensity of the electrostatic field at the jet surface:

$$E_* = \sqrt{4\pi\sigma W_* / R}. \qquad (6)$$

In electrodispersion experiments, liquids are used whose coefficients of surface tension $\sigma$ vary within fairly wide regions from 0.07 dyne/cm for liquid helium ($He^3$ at $T = -271$C) and 1.98 dyne/cm for liquid hydrogen at $T = -253.1$C up to ~1000 dyne/cm for inorganic substances in a liquid state [18], and the radii of jets of the liquids exposed to dispersion equal ~20–1000 μm [8, 19–22]. According to (6), for jets of liquid helium from the indicated range of radii, the jet surface electrostatic field intensity at $W_* = 1$ will vary in the range of ≈21 $CGSE$ = 6.3 $kV$/cm at $R = 2 \times 10^{-3}$ cm up to ≈3 $CGSE$ = 0.9 $kV$/cm at $R = 0.1$ cm. With an increase in the parameter $W_*$, the intensity field value at the jet surface will increase $\sim\sqrt{W_*}$. Note now that the intensity of the electric breakdown of the air under a stationary homogeneous electric field at atmospheric pressure according to [17] is ≈26 kV/cm. This means that, for the liquid helium jet with $R = 2 \times 10^{-3}$ cm, parameter $W_*$ fails to exceed $W_* \approx 17$. The comparison of $W$ parameter values with the ones obtained above, corresponding to the possibility of jet disintegration $W \sim 1$ (see Fig. 2a), signifies that the breakdown phenomena fail to be the obstacle for realization of both capillary-electrostatic instability and electrostatic-capillary instability of the jet for liquid helium.

For the liquid hydrogen jet, similar calculations lead to the values of $W_* \approx 0.6$ for $R = 2 \times 10^{-3}$ cm and $W_* \approx 29$ for $R = 0.1$ cm. This signifies that discharge processes at the surface of a thick ($R = 0.1$ cm) jet of liquid hydrogen will fail to interfere with its disintegration into separate drops, but for a thin jet ($R = 2 \times 10^{-3}$), the electrostatic-capillary instability will no longer be able to occur, and the capillary-electrostatic one will be limited from above by the value of $W_* \approx 0.6$ (see Fig. 2b). Hence, the mode of complete stabilization of the liquid hydrogen jet by the electric self-charge may be observed only with jets of $R > 5 \times 10^{-3}$ cm.

For jets of kerosene, liquid chlorine, benzol, decane, or mercury diethyl with dielectric permeabilities of $\varepsilon_{\text{in}} \approx 2$ and coefficients of surface tension $\sigma \approx$ (25–30) dyne/cm at $T = 293$K, we likewise obtain $W_* \approx 0.04$ for $R = 2 \times 10^{-3}$ cm and $W_* \approx 2.1$ for $R = 0.1$ cm. The comparison of these values with calculation results presented in Fig. 3b illustrates that the breakdown phenomena at the jet surface will lead to limitations of the admissible values of the charge parameter both for thin and for thick jets. The calculations show (see, e.g., Figs. 3c and 3d) that a similar picture will exist for other liquids as well with $\varepsilon_{\text{in}} > 2$ coefficients of surface tension measured in tens of dyne/cm.

## CONCLUSIONS

The present analysis shows that, for jets of dielectric liquids with minor values of dielectric permeability ($\varepsilon_{in} < 1.32$), small volume electrical charges produce a stabilizing effect: for liquids with such dielectric permeabilities, there exist ranges of finite width of volume charges which entirely suppress the capillary instability of the jet. At random dielectric permeabilities of the liquid $\varepsilon_{\text{in}}$ in the vicinity of point $k = 0$, there exists a region of values of wave numbers, the width of which depends on $\varepsilon_{\text{in}}$ and the value of charge parameter $W$, in which the axisymmetric waves at the jet surface are stable. The existence of this stabilization region is stipulated by the jet charge and at $W = 0$ it is absent.

## ACKNOWLEDGMENTS

This work was performed within the framework of the thematic plan of the university with support from the following grants: the governor of Yaroslavl oblast, Russian Education Foundation (no. 2.1.1/3776), and Russian Foundation for Basic Research (nos. 09-01-00084 and 09-08-00148).

## REFERENCES

1. Baily, A.G., Electrostatic Atomization of Liquids (review), Sci. Prog.,Oxford, 1974. vol. 61, pp. 555–581.
2. Kozhenkov, V.I., and Fuks, N.A., Electrohudrodynamic Dispersion of Liquid (review), Usp. Khimii, 1976, vol. 45, no. 12, pp. 2274–2284.
3. Buraev, T.K., Vereshchagin, I.P., and Pashin, N.M., Dispersion Process Investigation of Liquids in the Electric Field, in *Sil'nye elektricheskie polya v tekhnologicheskikh protsessakh* (Strong Electric Fields in Technological Processes), Moscow: Energiya, 1979, no. 3, pp. 87–105.
4. Entov, V.M., and Yarin, A.L., Dynamics of Free Jets and Films of Viscous and Rheologically Complex Liquids, VINITI, Itogi nauki i tekhniki, ser. "Mekhanika zhidkosti i gasa", 1984, vol. 17, pp.112–197.
5. Fenn, J.B., Mann, M., Meng, C.K., et al., Electrospray Ionization for Mass Spectrometry of Large Biomolecules (review), Science, 1989, vol. 246, no. 4926. pp. 64-71.
6. Ametistov, E.V., Blazhenkov, V.V., Gorodov, A.K., et al., Monodispergirovanie veshchestva: printsipy i primenenie (Monodispersion of Substance: Principles and Application), editor V.A. Grigor'eva, Moscow: Energoatomizdat, 1991, p. 336.
7. Grigor'ev, A.I., Shiryaeva, S.O, Voronina, N.V., and Egorova, E.V. . On Oscillations and Random Disintegra-

tion of Charged Liquid Jets (review), Surf.Eng.Appl.Electrochem., 2006, no. 6, pp. 15–27

8. Shiryaeva, S.O., Grigor'ev, A.I., and Volkova, M.V., *Spontannyi kapillyarnyi raspad zaryazhennykh strui* (Random Capillary Disintegration of Charged Jets), Yaroslavl: Izd-vo YarGU, 2007, p. 340.
9. Shiryaeva, S.O., Grigor'ev, A.I., and Levchuk, T.V., On Stability of Nonaxisymmetric Modes of Volumetrically Charged Jet of Viscous Dielectric Liquid, J.Techn. Phys., 2003, vol. 73. issue 11, pp. 22–30.
10. Grigor'ev, A.I. and Shiryaeva, S.O., On Influence of Jet Volume Charge of Dielectric Liquid on Position and Range Width of Wave Lengths that Cause Capillary Instability, Electronic J. "Issledovano v Rossii", 2009, no. 036, pp. 86-395. http://zhurnal ape.relarn.ru/articles/2009/036.pdf
11. Strutt, J.W. (Lord Rayleigh), On the Stability of Jets, Ttrudy mat.obshchestva (Proc. Math. Soc.), London, 1878, vol. 10, pp. 4–13.
12. Akhadov, Ya.Yu., *Spravochnik po dielektricheskim parametram chistykh zhidkostei* (A Handbook on Dielectric Parameters of Pure Liquids), Moscow: MAI, 1999.
13. Strutt, J.W. (Lord Rayleigh), On the Capillary Phenomena of Jets, Trudy korolevskogo nauch. Obshchestva (Proc. Roy. Soc.), London, 1879, vol. 28, pp. 406–409.
14. Frenkel', Ya.I., *Na zare novoi fiziki* (At the Dawn of New Physics), Leningrad: Nauka, 1970.
15. Raizer, Yu.P., *Fizika gazovogo razryada* (Physics of Gas Discharge), Moscow: Nauka, 1987.
16. Lozanskii, E.D. and Firsov, O.B., *Teoriya iskry* (Theory of Spark), Moscow: Atomizdat, 1975.
17. Aleksandrov, A.F., Bychkov, V.L., and Grachev, L.P., et al., Air Ionization in Near-Critical Electric Field, Zh. Techn.Fiz., 2006, vol.76, issue 3, pp. 38–43.
18. Nikol'skii, B.P., *Spravochnik khimika* (A Handbook of a Chemist), Leningrad: Khimiya, 1971.
19. Cloupeau, M. and Prunet, Foch B., Electrostatic Spraying of Liquids: Main Functioning Modes, J. Electrostatics, 1990, vol. 25, pp. 165–184.
20. Jaworek, A. and Krupa, A., A Classification of the Modes of EHD Spraying, J. Aerosol Sci., 1999, vol. 30, no. 7, pp. 873–893.
21. Shiryaeva, S.O., and Grigor'ev, A.I., The Semiphenomenological Classification of the Modes of Electrostatic Dispersion of Liquids, J. Electrostatics, 1995, vol. 34, pp. 51–59.
22. Shiryaeva, S.O., Grigor'ev, A.I., and Svyatchenko, A.A., Classification of Operation Modes of EHD Sources of Ions, Preprint of Inst. of Microelectronics of RAS, Yaroslavl', 1993, no. 25.

*ISSN 1068-3755, Surface Engineering and Applied Electrochemistry, 2009, Vol. 45, No. 5, pp. 364–369.*

# The Association of Electric and Optical Properties of Plasma-Solution Systems

**A. V. Khlyustova, A. M. Manakhov, A. I. Maksimov, and M. S. Khorev**
*Institute of Chemistry of Nonaqueous Solutions, Russian Academy of Sciences*
*Akademicheskaya ul. 1, Ivanovo, 153045 Russia*

Received March 25, 2009

**Abstract**—The phenomenology of the underwater “face” discharge and glow discharge under oscillatory conditions is presented. Electric and spectral features of these discharges are examined. It is shown that the afterglow duration exceeds 0.1 s, being the consequence of high chemical activation of the solution volume.

**DOI:** 10.3103/S1068375509050044

## INTRODUCTION

The greatly promising direction of practical implementation of plasma-solution systems (PSSs) is connected with initiation of chemical processes in solutions, among other things, to treat and sterilize water and various objects placed in the solution as well as to modify natural and synthetic polymer materials. We consider PSSs in which the solution plays the role of one or both electrodes of the gas discharge, there occurring two greatly different variants of the relative positions of plasma and solution. By convention, the PSSs are classified as “above-water” and “underwater” ones. In the first case (glow discharge, gliding glow discharge), the plasma zone lies above the solution surface, and chemically active particles are generated in the plasma zone (i.e., outside the solution) and in the thin solution surface layer bombarded by positive ions from the plasma.

The passage of electric current of sufficiently high voltage in electrolytic cells through diaphragms or dielectric tubes (capillaries) filled with the solution allows initiation of different underwater discharges (relatively low voltage ones—from hundreds of volts) [1]. Plasma ignited in the vapor–gas mixture and directly contacting the solution could be more successfully used in the above-mentioned cases [2].

Chemical activation of solutions is first and foremost connected with the generation of H and OH radicals in their bulk. PSS optical radiation always includes emission lines and bands of these particles. Thus, the study of PSS radiation allows one to obtain information on generation of chemically active particles and on the possibilities of their use in chemical transformations. At the same time, it is necessary to consider the relation between the PSS electrophysical properties of plasma-solution systems and their optical radiation in order to control the solution chemical activation process.

The classic glow discharge with an electrolytic cathode (Fig. 1) and also one of the underwater discharges ignited in a solution-filled dielectric tube vertically immersed in the main cell with the solution (“face” discharge) (Fig. 2) are investigated in this work.

It has been assumed that the classic glow discharge at atmospheric pressure with an electrolytic cathode scarcely participates in initiation of chemical reactions in solutions since the primary active particles ($\dot{\mathrm{H}}$, $\dot{\mathrm{O}}\mathrm{H}$, $e_{\mathrm{soiv}}$) are generated only in a very thin surface layer of the solution and are also expended in it. Only a “secondary oxidizer”—hydrogen peroxide—can react in the solution bulk. Underwater discharges, for instance, a face one, are considered a more effective way of solution chemical activation. At the same time, the analysis of electric and optical properties of the glow discharge with the flow-through electrolytic cathode shows that there are some conditions (discharge burning regimes) under which the chemical activation of solutions by the glow discharge is close to that in the case of the face discharge.

## EXPERIMENTAL SETUP

The diagram of the setup to study the PSS electric and optical properties is shown in Fig. 3.

LiCl, NaCl, and $CaCl_2$ solutions with a concentration of 0.1 mol/l were used as electrolytic cathodes in the experiments with glow discharge. The rate of the solution circulation in the cell was 60 ml/min. The discharge current was varied within the range from 40 to 75 mA.

Solutions of $Na_2SO_4$ with a concentration of 0.015 mol/l and $H_2SO_4$ with pH = 2 were used as working electrolytes in the case of the “face” discharge. The discharge current was 250–300 mA.

---

[1] Khlyustova, A.V., Manakhov, A.M., Maksimov, A.I., and Khorev, M.S., *Elektronnaya Obratotka Materialov*, 2009, no. 5, pp. 18–23

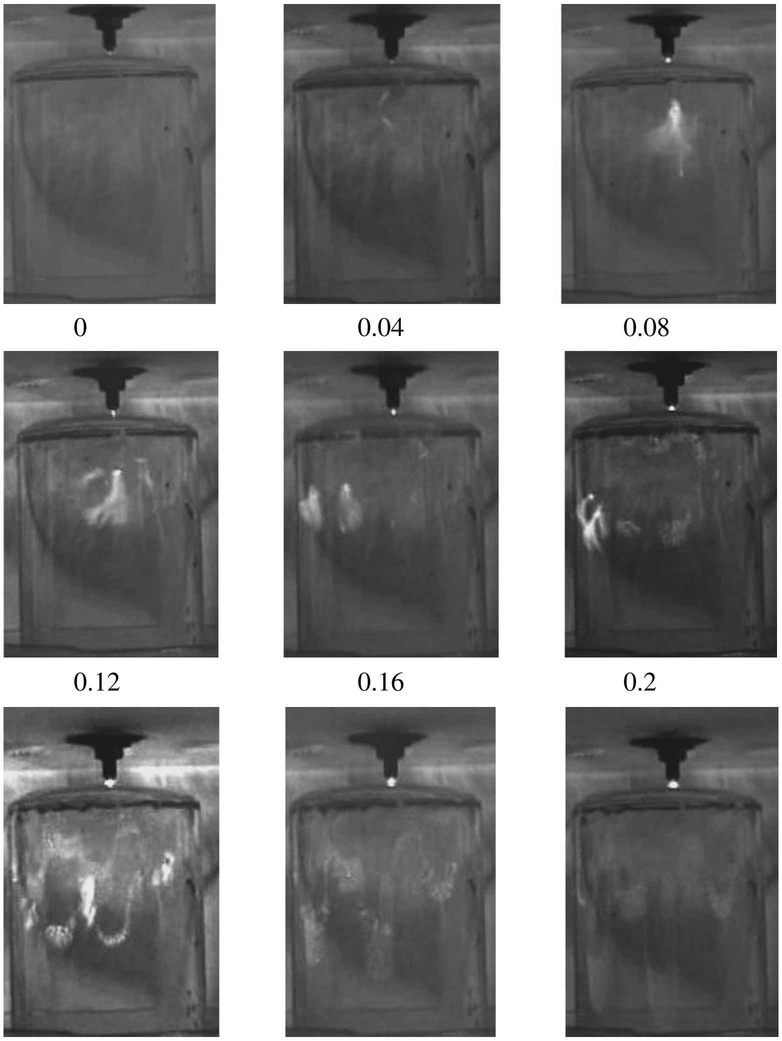

0 0.04 0.08

0.12 0.16 0.2

0.24 0.28 0.32

**Fig. 1.** Oscillating form of the glow discharge with the flow-through electrolytic cathode. Dynamics of luminous zone generation (in seconds).

## EXPERIMENTAL RESULTS AND DISCUSSION

### *1. "Oscillating Form" of Glow Discharge with Flow-Through Electrolytic Cathode*

As shown previously [3], a sufficiently long burning of the glow discharge with the flow-through electrolyte cathode causes under certain conditions its transition from the quiescent form of quasi-steady discharge into the oscillatory regime. And in the solution surface layer, there are observed luminous formations moving in radial directions from the cathode spot toward the solution flow. The lifetime of these luminous regions is sufficiently large to give them an opportunity to traverse the whole horizontal surface of the solution and even to "flow down" the vertical wall of the internal vessel of the cell with the solution. As will be shown below, this makes it possible to predict the efficiency of the solution chemical activation by such glow discharge resembling the action of the face discharge.

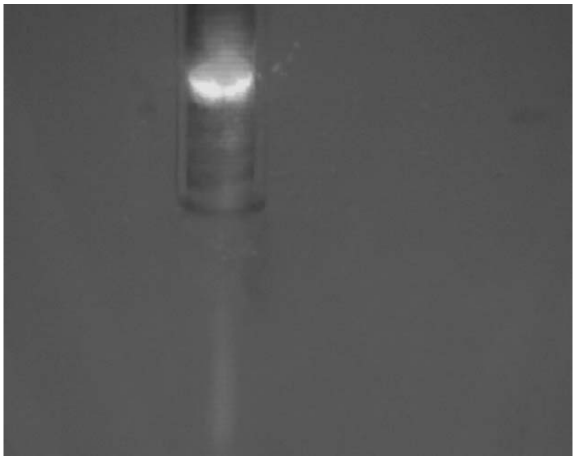

**Fig. 2.** Exterior view of the face discharge.

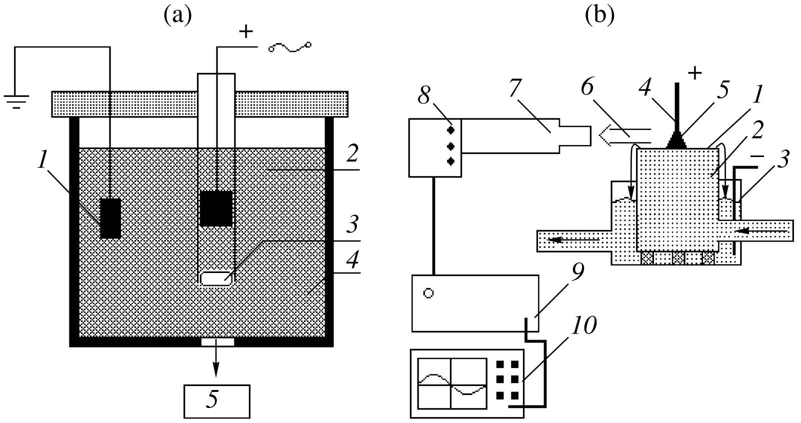

**Fig. 3.** Diagram of the setup to study PSS electric and optical properties: (a) the cell for the face discharge: (*1*) graphite cathode, (*2*) anode (graphite), (*3*) plasma zone, (*4*) solution, (*5*) photodetector; (b) for glow discharge: (*1*) working cell, (*2*) cathode, (*3*) anode, (*4*) positive column, (*5*) optical radiation direction, (*6*) UM-2 monochromator, (*7*) photoprobe unit, (*8*) signal multiplication unit, (9) recording system (OWON oscillograph).

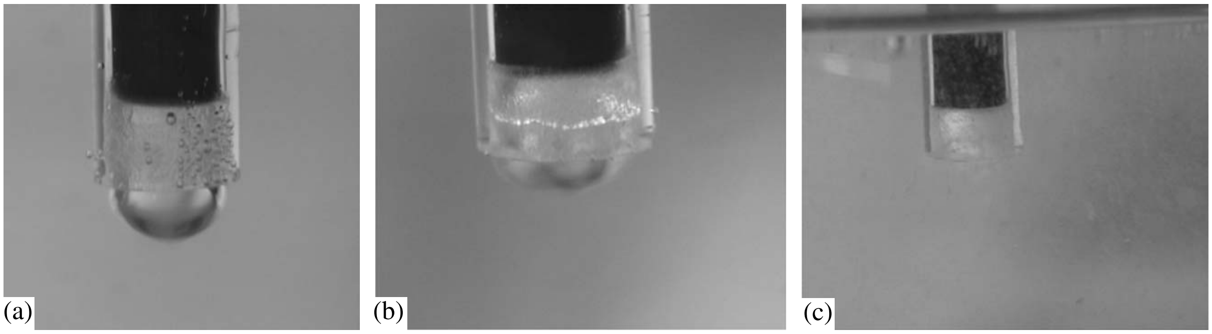

**Fig. 4.** Dynamics of breakdown in the face discharge: (a) generation of steam-and-gas bubble before electrical breakdown; (b) "silent" form of the discharge preceding the main breakdown; (c) discharge shunted by the solution.

### *2. Phenomenology of the Face Discharge*

Experience shows that the initiation of the plasma zone pictured in Fig. 2 with the distance between the electrode and the open tube end being large enough can occur in different parts of the tube with its further displacement to the open end, as is the case in the generation of plasma formations in long tubes [2]. However, since the distance between the electrode and the tube end is small, the plasma, as a rule, appears near the tube section.

According to the video filming data, the process develops in the following way. The discharge development is preceded by the generation of a bubble near the tube section (Fig. 4a). According to our estimate, the bubble content includes about 95% steam and only 5% electrolysis products. No bubble breakdown occurs because the source voltage is not high enough. The bubble executes some oscillations in its bulk and then collapses without an electric discharge. In our opinion, the bubble oscillations could be associated with the periodic accumulation and blowout of the electrolysis products into the main solution. When the voltage is higher, a discharge occurs in the form of a lot of fine luminous formations along the perimeter of the bubble contact with the tube preceding the main discharge (Fig. 4b). It is conceivable that this phenomenon is similar to corona discharge ignition before the initiation of the main diaphragm discharge observed in [3].

When the voltage is high enough, development of an intermediate form of discharge into the main discharge occurs, which does not necessarily overlap the whole tube section (Fig. 4c). Thus, the plasma zone appearing in the tube is, as a rule, shunted by a solution layer (film) and this fact should be taken into account when analyzing the equivalent scheme of the face discharge.

The changes in the current and the voltage drop across the cell observed at breakdown and initiation of the discharge depend on the relation of the electrical conductivity of the solution and the originating plasma zone. Solutions with high electrical conductivity were used in our experiments so the discharge ignition was always accompanied by the decrease in the total current in the circuit as compared to the initial electrolysis current, the voltage drop across the cell growing (Fig. 5a).

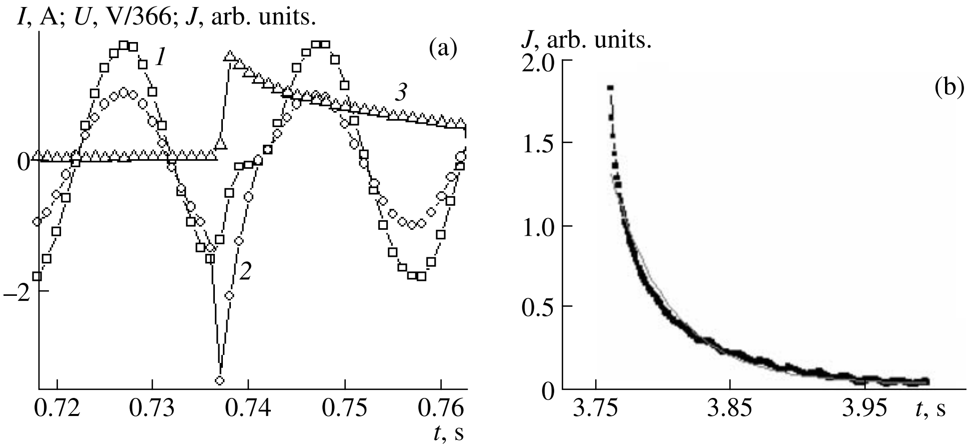

**Fig. 5.** (a) Time dependences of current in the circuit, voltage drop across the cell, and intensity of integral radiation during electric discharge (0.015 M $H_2SO_4$ solution, $T_0 = 50°C$): (*1*) current, A; (*2*) voltage drop across the cell, B/366; (*3*) integral radiation intensity, arb. units; and (b) the section of radiation intensity decay. The data on radiation intensity are taken for the violet region of the spectrum.

### *3. Electric and Optical Characteristics of the Face Discharge*

The oscillograms of the face discharge current and voltage obtained with the help of the circuit depicted in Fig. 3a support qualitatively the above conclusion on its nature (Fig. 5a). From the fact of the discharge to be shunted by the solution, it also follows that, at the high electrical conductivity of the solution, the thickness of the layer shunting the plasma (with the given current) is limited by the condition that the voltage drop across the discharge gap should be equal to the minimum voltage of the discharge burning. The latter also depends on the solution properties, at least through the coefficient $\gamma$—the emission of electrons from the solution determining the cathode potential drop. Such dependence is seen from Table 1, in which there are tabulated the values of the active face discharge ignition voltage at different characteristics of the solutions. As the data of the table show, the voltage of the discharge maintenance depends not only on the electrical conductivity but also on the chemical nature of the electrolyte.

The change in the integral radiation intensity of the plasma-solution system is shown in Fig. 5a too. The presence of the long afterglow persisting when the discharge has completely decayed should be emphasized. If discharge active phase lasts about 3 ms, the afterglow duration can in some cases be 100 ms. It should be assigned to the solution and classified as the solution chemiluminescence initiated by the discharge. The afterglow duration values obtained from the analysis of the radiation damping curves of the type presented in Fig. 5b are tabulated in Table 2.

In all cases, the afterglow duration is more than 0.1 s. It is important that it is nearly the same for the solutions of sodium sulfate and sulfuric acid in spite of the obvious difference of their glows: in the case of the sodium sulfate solution, the contribution of the resonant radiation of sodium atoms is large, naturally being absent in the case of the sulfuric acid solution. The contribution to the integral radiation of the band of the radical OH and atoms H is large in both cases.

In our opinion, the most important consequence of the long face discharge afterglow is the following. As mentioned above, the afterglow does not belong to the plasma zone (the plasma has already decayed) but to the solution. The face discharge plasma collapse causes an intense flow of the activated solution from the tube section into the main solution bulk. In about 0.1 s, the solution manages to travel several centimeters. This means that OH radicals and H atoms manage to cover this distance. Thus, the solution activation already occurs in a rather large volume, increasing the efficiency of the initiation of both homogeneous and heterogeneous reactions, particularly, treating water and modification of macromolecular compounds placed in the solution.

**Table 1.** Voltage of the main face discharge ignition at the initial temperature of the solution of 25°C

| Solution | Electrical conductivity, mCm/cm | Breakdown voltage, V |
|---|---|---|
| $Na_2SO_4$ 0.05 M | 9 | 450 |
| $Na_2SO_4$ 0.025 M | 5 | 500 |
| $Na_2SO_4$ 0.005 M | 1 | >1500 |
| $Na_2SO_4$ 0.003 M | 2 | 1200 |
| $Na_2SO_4$ 0.015 M | 9 | 950 |
| $Na_2SO_4$ 0.02 M | 15 | 550 |

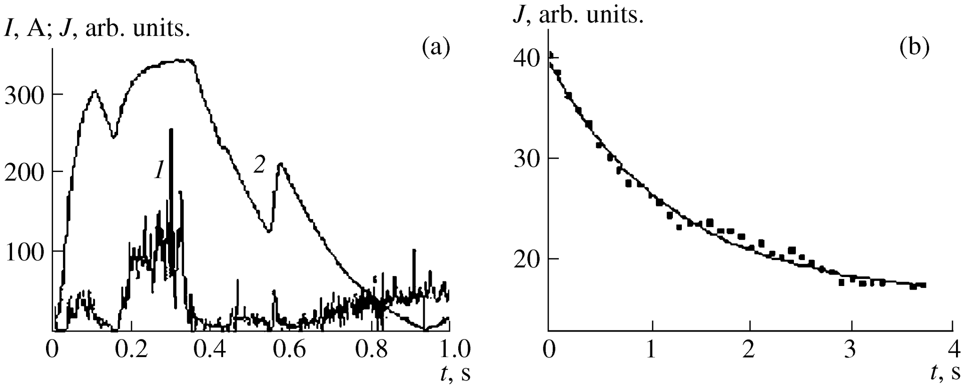

**Fig. 6.** Oscillograms of the current (*1*) and unit peak of sodium resonant line radiation intensity (*2*) in the glow discharge. (a) 0.1 M NaCl solution and (b) the section of the radiation intensity decay.

## *4. Electric and Spectral Characteristics of the Oscillating Form of Glow Discharge*

Transition to the glow discharge oscillating regime is the reason that the discharge current and voltage drop across the cell cease to be constant. Synchronous bursts are observed in the oscillograms of current and radiation intensity (recorded mainly according to the intensity of resonant lines of alkaline metal atoms). They are related to the moments of the passage of the luminous plasma formations. The characteristics of the bursts going one after another are different. This is no surprise since they belong to the sequence of the luminous regions generated by the discharge. The luminous zone passing the discharge current varies, the source emf being constant, and thus this process is accompanied by the reduction of the total resistance of the solution.

The radiation intensity growth begins simultaneously with the increase in the current. But the radiation peak width is substantially larger than the discharge current peak width. Furthermore, some conditions occur where the radiation band overlaps several current pulses and has a complicated shape which could be interpreted as a result of superposition of radiation of the luminous formations going one after another (Fig. 6a). The right branch of the radiation curve of a single pulse (or the last one in the overlapping sequence) has the shape of a damped exponential, allowing one to estimate the single plasma formation afterglow duration (Fig. 6b). The results of estimations of the afterglow duration from the curves of the intensity drop of the sodium resonant line radiation are tabulated in Table 3.

As is seen from the presented data, the afterglow duration is as a rule more than 100 ms. Thus, all conclusions made for the face discharge afterglow are applicable to the oscillating form of the glow discharge. The distribution of active zones over the large expanses of the solution is observed visually in this case.

**Table 2.** “Face” discharge afterglow duration estimated by the curves of radiation integral intensity decay

| Peak number | τ, ms | |
|---|---|---|
| | Violet region of spectrum | Yellow region of spectrum |
| 1 | 43 | 34 |
| 2 | 31 | 36 |
| 3 | 24 | 28 |
| 4 | 14 | 30 |
| 5 | 16 | 16 |
| 6 | 27 | 30 |
| 7 | 42 | |
| 8 | 44 | |
| 9 | 39 | |

**Table 3.** Duration of afterglow initiated by oscillatory glow discharge in 0.1 M NaCl solution. The number of peaks in intensity is taken from time oscillograms with a total duration of 50 s (not presented in the text)

| Peak number | τ s, by exponential decay of intensity |
|---|---|
| 1 | 1.22 |
| 2 | 0.84 |
| 3 | 1.08 |
| 4 | 0.75 |
| 5 | 0.69 |

## CONCLUSIONS

The electric and optical properties of the oscillating form of a glow discharge as well as of the discharge occurring in the section of a dielectric tube immersed in an electrolyte solution have been investigated. The existence of two forms of face discharge is shown. The duration of the active form of discharge is about 3 ms. The burning voltage and other features of the active discharge depend on the electrical conductivity and the chemical composition of the electrolyte.

The discharge initiates afterglow in the solution, its duration being more than 100 ms. The transition of the glow discharge to the oscillating regime depends on the chemical nature of the solution, the temperature, and the duration of the previous quasi-stationary discharge burning. In the discharge oscillating form, there are observed rather wide current pulses and synchronous radiation pulses, the radiation pulse duration exceeding the current pulse duration. The afterglow, as in the case of the face discharge, belongs to the solution. Its duration may last up to ~1 s. The presence of afterglow in the solution initiated by the examined types of discharge indicates a chemical activation of large volumes of solution, i.e., a high efficiency of their possible practical applications.

## REFERENCES

1. Kutepov, A.M., Zakharov, A.G., and Maksimov, A.I., *Vakuumno-plazmennoe i plazmenno-rastvornoe modifitsirovanie polimernykh materialov* (Vacuum-Plasma and Plasma-Solution Modification of Polymer Materials), Moscow: Nauka, 2004.
2. Maksimov, A.I., Physics, Chemistry and Application of the AC Diaphragm Discharge and Related Discharges in Electrolyte Solutions, *Contrib. Plasma Phys.*, 2007, vol. 46, nos. 1–2, p. 8.
3. Khlyustova, A.V., Khorev, M.S., and Maksimov, A.I., The Non-Linear Features of Transfer Processes of Solution Components into Gas Phase under Discharge Action: Effect of “Spread Discharge”, *Euras. Phys. Tech. J.*, 2008, vol. 5, no. 2(10), pp. 6–9.
4. Teslenko, V.S., Drozhzhin, A.P., and Kartashov, A.M., Generation of Self-Oscillating Processes at Diaphragm Discharge in Electrolyte, *Pis’ma v Zh. Tekh. Fiz.*, vol. 27, is. 20, pp. 83–88.

ISSN 1068-3755, Surface Engineering and Applied Electrochemistry, 2009, Vol. 45, No. 5, pp. 370–374. © Allerton Press, Inc., 2009.
Original Russian Text © S.A. Chulovskaya, S.M. Kuz'min, V.I. Parfenyuk, 2009, published in Elektronnaya Obrabotka Materialov, 2009, No. 5, pp. 24–29.

## ELECTRICAL PROCESSES IN ENGINEERING AND CHEMISTRY

# Morphological and Dimensional Properties of Ultradispersed Powders Produced by the Electrochemical Method from Electrolyte Solutions

**S. A. Chulovskaya[a], S. M. Kuz'min[a], and V. I. Parfenyuk[b]**
[a]*Institute of the Chemistry of Nonaqueous Solutions, Russian Academy of Sciences, ul. Akademicheskaya 1, Ivanovo, 153045 Russia*
*e-mail: vip@isc-ras.ru, aim@isc-ras.ru*
[b]*Ivanovo State Academy of Chemical Technology, pr. F. Engelsa 7, Ivanovo, 153000 Russia*

Received June 29, 2009

**Abstract**—Ultradispersed copper-bearing powders have been produced by the method of electrochemical cathode reduction from water–isopropanol solutions of copper dichloride. The dimensional and morphological properties of the obtained compounds have been studied using the procedure of atomic-power microscopy. It is shown that the introduction of isopropyl alcohol additions into the aqueous electrolyte composition causes a change of both the dimensional and qualitative features of the powders. The isopropyl alcohol admixture shifts the ratio between the components entering into the composition of the copper-bearing powders towards a greater content of copper oxide (I).

**DOI:** 10.3103/S1068375509050056

## INTRODUCTION

Modern materials science assigns the leading position to nanosized metal powders possessing functional properties different from the corresponding condensed phases [1–3]. The advances in scientific research and use of metal nanoparticles to a great extent depends on the potentialities of the synthesis methods, in particular, whether it is possible to produce particles meeting the requirements of a specific scientific or practical problem. From this viewpoint, there are some advantages the ecologically safe electrochemical synthesis of nanosized powders when a metal and its compounds pass from the dissolved state on a cathode in the form of loose sediments [4, 5]. To realize the electrosynthesis process, it is necessary to know the factors influencing the generation of sediments and determining their physical and chemical properties.

Nucleation on the substrate's active centers is the initial state of the sediment generation. By varying the process conditions and the electrolyte composition, it is possible to affect the course of the sediment growth: to accelerate or abruptly retard the growth of the primary formations and the buildup of other crystals on their surface. The deposition at the limiting current densities is characterized by the moderation of the stage of the metal cation diffusion to the electrode surface, thus promoting the generation of highly dispersed loose cellular sediments. The addition of surface-active agents increases the cathode polarization, reduces the powder's surface energy, and consequently contributes to the probability of nucleus generation [6].

The introduction of ultradispersed powders of metals into the composition of plastic lubrication material improves the service properties of the conjugate pairs [7]. The investigation carried out of materials modified by powders of copper and its oxides has shown the utility of the practical implementation of the manufactured powders in order to create new proficient catalysts with a large specific surface in the reaction of carbon monoxide conversion by steam [8]. The use of the produced copper-bearing powders to modify medical materials with the aim to impart to them biocidal properties [9, 10] with respect to many kinds of bacteria shows considerable promise.

The correlation of the dimensional characteristics and composition of the electrolytically deposited ultradispersed copper-bearing powders produced from aqueous and water–isopropanol solutions of copper dichloride is the purpose of this work.

## EXPERIMENTAL

Ultradispersed (nanosized) copper-bearing powders were produced by the method of cathode reduction from water–organic solutions of electrolytes [11–13]. The cathode sediments of the ultradispersed copper and its compounds entering into the composition were deposited on a previously cleaned steel cylindrical cathode at a constant electrode potential. Oxideruthenic–titanic plates served as the anode. Aqueous and water–isopropanol solutions of 0.1 m copper dichloride were used as the electrolyte.

At the close of the electrolysis, the produced sediment was separated from the electrode, carefully washed with distilled water up to a constant value of the electric conductivity in the mother residue, and dried to the powered state.

The study of the dimensional and morphological properties of the powders was conducted by the method of atomic force microscopy (AFM) using a Solver-47-Pro device. The examined specimens were first dispersed in acetone, and the prepared suspension was applied on a special-purpose substrate and dried in the air. In order for the specimen under examination to be uniformly distributed, this procedure was performed with the rotation of the substrate in a centrifuge (Fig. 1). Centrifuging causes the spreading out of the drop on the substrate and its quick evaporation, allowing one to avoid the appearance of an aureole of the substance particles around the drop on the substrate.

The treatment of the images obtained by the AFM method was carried out using a program including the mathematical leveling of the substrate surface's tilt, the construction of histograms of the particles' distribution with their height, and the analysis of the particles' shape with the help of section diagrams.

X-ray investigation was performed using a DRON-3M diffractometer using Cu$K_\alpha$ radiation. The determination of the chemical composition was carried out by correlation of the parameters of the studied object's diffraction lines with reference data [14].

## DISCUSSION OF THE RESULTS

In works [6, 11], there is pointed out the character of the size distribution of the nanoparticles obtained by electrodeposition from aqueous and water–isopropanol solutions of 0.1 m copper dichloride.

The scanning of the specimen's surface with the help of a probe allows one to gain a three-dimensional image presenting more descriptive and full information on the particles' morphological peculiarities. An example of a three-dimensional image of the substrate with ultradispersed particles of the copper-bearing powder produced by electrodeposition from a water–isopropanol solution of $CuCl_2$ is presented in Fig. 2.

It is not difficult to notice that, along with single particles, there are aggregates consisting of finer particles. The scanning results for the same specimen under the tapping mode (a) and the non-contact mode (b) are shown in Fig. 3.

It should be mentioned that the phase contrast regime has a higher resolution and allows one to obtain flat-bed dimensions with a high degree of accuracy. However, this image doesn't give any information on the sizes of the particles under study in the vertical plane (with their height). The observed particle height can be determined by the analysis of the topographic picture showing the particle section profile along the selected axis (Fig. 4).

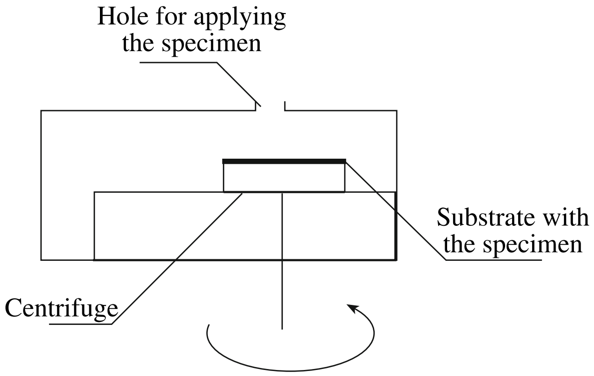

**Fig. 1.** Diagram of the setup to prepare a specimen for study on the atomic force microscope.

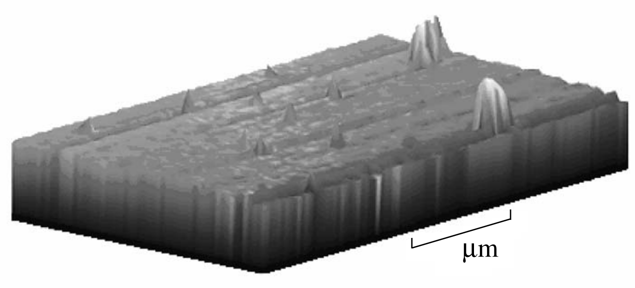

**Fig. 2.** Three-dimensional image of the substrate with ultradispersed particles of copper-bearing powder.

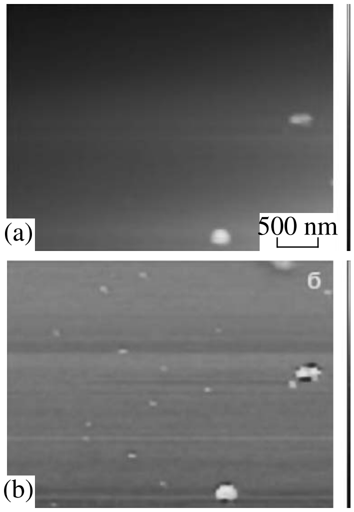

**Fig. 3.** Typical image view of the specimen produced by the AFM method.

The presented sections of a single particle (Fig. 4a) and an aggregate (Fig. 4b) show that, for single particles, the vertical size is close to the diameter, while the aggregates have a height smaller than their plane sizes.

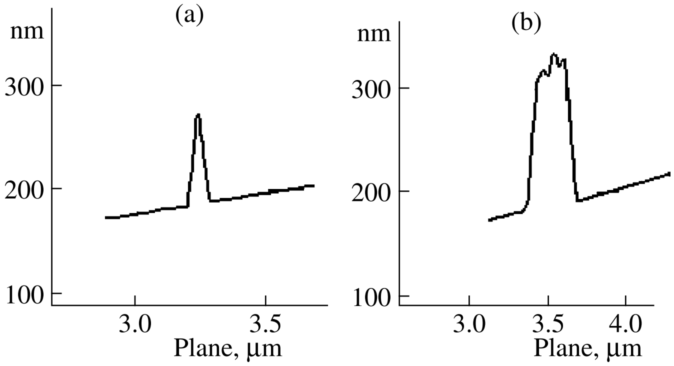

**Fig. 4.** Profiles of sections of single (a) and aggregated (b) particles.

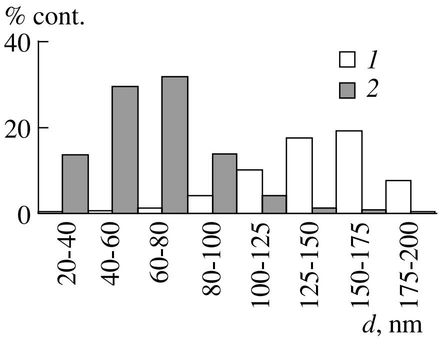

**Fig. 5.** Distribution histograms for the nanosized copper-bearing particles in the powder produced by electrodeposition from aqueous (*1*) and water–isopropanol (*2*) solutions of copper dichloride.

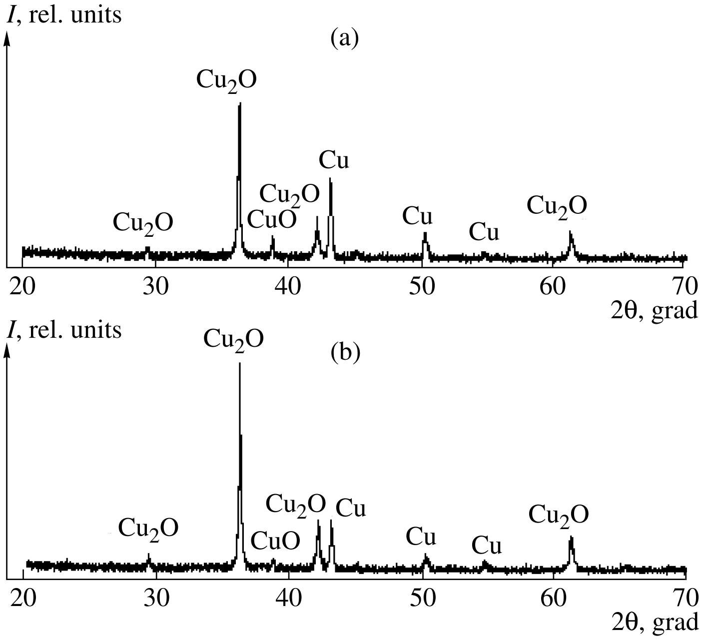

**Fig. 6.** X-ray pictures of nanosized copper-bearing powders produced from aqueous (a) and water–isopropanol (b) solutions of copper dichloride.

The histograms of the particles' distribution by sizes (Fig. 5) are constructed according to the set of the studied specimens' topographical images, where by the size the particles' mean diameter is meant. Nanosized particles from 100 up to 200 nm make up the main part (~70%) of the powder in the first case. It is largely odd-shaped aggregates formed due to the packing of fine particles. The distribution of the powders by their sizes changes in the presence of $i$-$C_3H_7OH$. Most of (~90%) the powder particles are nanoparticles with sizes of about 40–100 nm. Larger formations are less numerous.

The qualitative composition of the synthesized powders is determined by X-ray phase analysis methods. According to the data presented in Fig. 6, the obtained product is multicomponent and includes unoxidized copper and copper oxides (I, II).

The predominance of some kind of oxide in the powder is connected with the dentrite growth trend and the nature of the overvoltage accompanying the metal discharge process. There is more Cu and CuO in the powders produced from aqueous electrolytes. After $i$-$C_3H_7OH$ is added, the content of $Cu_2O$ in the powder increases as indicated by the growth of the copper monoxide line intensity with interplane distances of $d$ = 2.46, 2.12, 3.00, and 1.51 nm (Fig. 6a).

The mean particle diameter was calculated by the formula

$$D = \frac{k\lambda}{\beta\cos\theta}, \qquad (1)$$

where $D$ is the crystal size; $\theta$ is the reflex Bregg angle, grad; $k$ is the coefficient depending on the crystal shape (for spherical particles $k = 1$; for the other ones, $k = 0.9$); $\lambda$ is the wave length, nm; and $\beta$ is the width of the reflex for half of the height, rad.

The treatment of the diffraction patterns shows that the mean size of the copper crystallites in the copper-bearing powder is 70 ± 10 nm. The mean size of the crystallites of the CuO and $Cu_2O$ copper oxides is 50 ± 10 nm.

When interpreting the roentgenography experiment, it should be taken into account that the roentgen radiation scattering occurs on the bulk elements. Furthermore, the contribution of the particles making up the largest proportion in the specimen's total volume to the determination of the mean crystallographic size of the crystallite is the greatest. The volume accounted for by the particles with the mean diameter $d$ is proportional to the product of the number of particles ($N$) with the respective size and the third power of the linear size $d^3$.

In the case of spherical particles, the total volume $V_d$ of the particles with the mean diameter $d$ can be estimated from relation (2):

$$V_d = \frac{\pi}{6}Nd^3. \qquad (2)$$

To compare the powders produced under various conditions, the dependence $V_d$ on the particle diameter $d$ has been normalized. The value of the total volume of the studied powder particles (assumed to be 100%) is used as the normalization parameter. The dependence of the total volume of the particles in the powder on their size is presented in Fig. 7.

A distinctive feature of the relationships for the powders produced from both aqueous solutions and water–organic media is the appearance of peaks repeating at regular intervals.

In the case of the water-isopropanol medium, the first peak lies in the range of 75–80 nm, suggesting the presence in the powder of a noticeable amount of particles consisting of single crystallites. The periodicity of the peaks (70, 150, 225, 300, 375, and 450 nm) gives the sequence of the crystallite number growth in the particles' cross section. In the case of the electrocrystallization from the aqueous medium, the first peak is displaced to sizes of about 150 nm and repeats at a regular interval of about 120 nm corresponding to the sum of the mean sizes of the crystallites of copper and its oxide. This could be due to the fact that the electrocrystallization of copper from aqueous solutions is accompanied by more intensive oxidation processes and the generation of the oxide phase in parallel with the reduced copper. It is also indicated by the higher intensity of the reflex corresponding to the copper oxide CuO in this specimen.

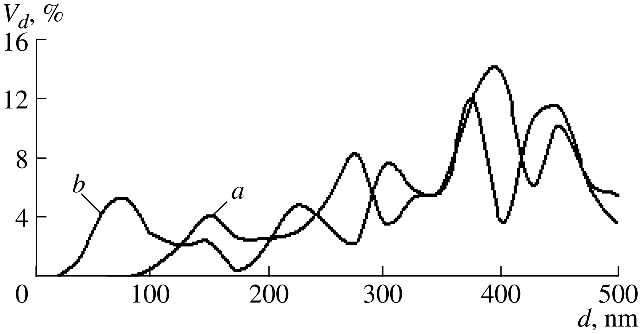

**Fig. 7.** The volume proportion of particles corresponding to the various diameters for powders produced from aqueou (*a*) and water-isopropanol (*b*) solutions of copper dichloride.

## CONCLUTION

The dimensional and morphological features of the powders synthesized by the electrochemical cathode reduction from aqueous and water-organic solutions of electrolytes have been studied by the AFM method. It is shown that the introduction of isopropyl alcohol additions into the aqueous electrolyte composition causes a change of both the dimensional and qualitative properties of the obtained powders. The additions of isopropyl alcohol shift the ratio between the components entering into the composition of the copper-bearing powders towards larger contents of copper oxide (I).

## REFERENCES

1. Andrievskii, R.A. and Ragulya, A.V., *Nanostrukturnye materialy* (Nanostructural Materials), Moscow: Akademiya, 2005.
2. Gusev, A.I., *Nanomaterialy, nanostruktury, nanotekhnologii* (Nanomaterials, Nanostructures, Nanotechnologies), Moscow: Fizmatlit, 2005.
3. Pomogailo, A.D., Rozenberg, A.S., and Ufland, I.E., *Nanochastitsy metallov v polimerakh* (Metal Nanoparticles in Polymers), Moscow: Khimiya, 2000.
4. Murashova, I.B., Taushkanov, P.V., and Burkhanova, N.G., Change of Structural Properties of Copper Loose Sediment at Galvanostatic Electrolysis, *Electrokhimiya*, (Electrochemistry) 1999, vol. 35, no. 7, pp. 835–840.
5. Chulovskaya, S.A., Lilin, S.A., Balmasov, A.V., and Parfenyuk, V.I., Electrochemical Production of Ultradispersed Copper-Bearing Particles from Water-Organic Solutions of Electrolytes, *Zashchita metallov*, (Metal Protection), 2006, vol. 42, no. 4, pp. 430–433.
6. Chulovskaya, S.A. and Parfenyuk, V.I., Influence of Electrolyte Solution Composition on the Process of Nanosized Copper Containing Powders, *Electr. Obrab. Mater.*, (Surf.Eng.Appl.Electrochem.), 2008, no.1, pp. 58–63.
7. Tesakova, M.V., Parfenyuk, V.I., and Godlevskii, V.A., Influence of Addition of Ultradispersed (Nanosized)

Copper-Bearing Powders on Tribological Properties of Industrious Lubricants, *Electr. Obrab. Mater.*, (Surf.Eng.Appl.Electrochem.), 2008, no. 6, pp. 56–62.

8. Tesakova, M.V., Parfenyuk, V.I., and Il'in, A.A., Physical, Chemical and Catalytic Properties of Ultradispersed (Nanosized) Copper-Bearing powders Produced by Electrochemical Method, *Izv. vuzov, Ser., Khim. i khim. tekhn.*, 2008, vol. 10, no. 11, pp. 22–26.
9. Garas'ko, E.V., Tesakova, M.V., Chulovskaya, S.A., and Parfenyuk, V.I., Usage of Nanosized Copper-Bearing Powders as Proficient Biocidal Preparations, *Izv. vuzov, Ser., Khim. i khim. tekhn.*, 2008, vol. 51, no. 10, pp. 116–119.
10. Alekseeva, O.V., Chulovskaya, S.A., Bagrovskaya, N.A., et al., Physical, Chemical and Anti-Microbe Properties of Film Nanocomposites on the Basis of Hydroxicellulose, *Zhidk. Krist., Prakt. Ispol.* 2007, is. 4(22), pp. 84–90.
11. Chulovskaya, S.A. and Parfenyuk, V.I., Influence of Isopropyl Alcohol on the Process of Cathode Deposition of Ultradispersed Copper-Bearing Powders from Electrolyte Solutions, *Zh. Fiz. Khim.* 2007, vol. 80, no. 6, pp. 952–955,
12. Chulovskaya, S.A., Lilin, S.A., Parfenyuk, V.I., and Girichev, G.V. Physical and Chemical Properties of Ultadispersed Copper-Bearing Powders Produced by the Method of Cathode Reduction, *Zh. Fiz. Khim.*, 2006, vol. 80, no. 2, pp. 332–335.
13. Chulovskaya, S.A. and Parfenyuk, V.I., Physical and Chemical Properties of Nanosized Copper2Bearing powders Produced from Water-Isopropanol Solutions of Copper Dichloride, *Izv. vuzov, Ser., Khim. i khim. tekhn.*, 2007, vol. 50, no. 11, pp. 49–54.
14. Mirkin, L.I., *Spravochnik po rentgenostrukturnomy analizu polikristallov*, (Handbook on X-ray Diffraction Analysis of Polycrystals), Moscow: Fizmatizdat, 1961.

ISSN 1068-3755, Surface Engineering and Applied Electrochemistry, 2009, Vol. 45, No. 5, pp. 375–381. © Allerton Press, Inc., 2009.
Original Russian Text © T.V. Bortsoi, 2009, published in Elektronnaya Obrabotka Materialov, 2009, No. 5, pp. 30–38.

## ELECTRICAL PROCESSES IN ENGINEERING AND CHEMISTRY

# Peculiarities of the Macroscopic Investigation of Multicomponent Electrochemichal Deposits on the Basis of the Comparison of Relative Deviations

**T. V. Bortsoi**

*Institute of Applied Physics, Academy of Sciences of the Republic of Moldova,*
*ul. Akademiei 5, Chisinau, MD-2028 Republic of Moldova*
*e-mail: bortzoi _tudor@yahoo.com*

Received April 14, 2009

**Abstract**—The paper presents an analysis of the available indicators of the correlation of the macroscopic distribution of the multicomponent electrochemical deposits and offers new indicators based on the principle of the comparison of the relative deviations from the average values of the sets of measurements of the dispersed parameters of electrochemical objects. The elaborated indicators reflect the correlation between the dispersed parameters with regard to the share in an aggregate (at the cathode macrolevel) of the compared feature of the relative deviations and allow for the objective checking of their estimation by other indicators. In addition, they enable a thorough investigation of the formation process of the multicomponent electrochemical deposits at the cathode macrolevel and application of their values for the purpose of the control and prediction of the functional structure of the deposits.

**DOI:** 10.3103/S1068375509050068

## INTRODUCTION

The functional properties of multicomponent electrochemical deposits largely depend on the distribution homogeneity of their composition at the cathode surface. For instance, in the case of composite deposits, the disperse phase concentration (DPHC) [1 and 2, et al.] serves as an indicator of the functional structure. However, for the purpose of the control and prediction at the macroscopic level of the distribution of the functional structure of a multicomponent deposit, there appears the necessity for a thorough investigation of the formation process with regard to the multiple acting factors. The latter are mainly characterized by the dispersed parameters (DP) of the objects of the electrochemical system.

In this connection, one of the directions of the microscopic investigation of the formation process of multicomponent electrochemical deposits is based on the estimation of the reciprocal DP distribution of the electrochemical objects [3, 4, 5, 6 and 7, etc.].

Note that the word combination "electrochemical object" implies anything that is being studied or may be studied from the viewpoint of an investigator (e.g., the physical or chemical properties of a deposit or a formation process of its structure). The dispersed parameters include the parameters of electrochemical objects in which there occur derivatives of at least one of the coordinates, but there may be of the three of them (e.g., the distribution of the potential, of the current density, and of the amount or composition of the deposit).

The study of the formation process of multicomponent deposits on the DP basis is of great practical and theoretical importance since it allows one to predict and control the conditions of the electrolysis and the functional properties of the deposits. The present research trend is based on such concepts as the principles of the comparison of the characteristics of the DP measurements sets, the methods of their comparison, and the methods of estimation of the DP correlation [6 and 7].

The category of a principle denotes the basis of the comparison of the DP values for revealing the distinguishing features of the correlation between the sets of their measurements (e.g., the average or relative characteristics of the DP sets, the deviations from the average values of a set, etc. [3, 4, 5, 6 and 7]).

The category of the way of the comparison implies the form of the comparison of the values or characteristics of the DP sets for selecting a distinguishing feature of correlation (e.g., by means of division, multiplying, etc. [3,6 and 7]).

The category of a method designates the type of quantitative measure of the relations between the values or characteristic of the DP for the estimation of a selected distinguishing feature (e.g., the estimation of the values of similar-sign relations, the relations of absolute values, similar-sign relations, etc. [3, 6 and 7].

Thus, for estimation of the correlations of the DP distributional patterns at the macrolevel of the electrode, certain methods of the given trend are based on the principle of comparison of the relative deviations of

$t_i$ calculated from the average value of a set of variations of the DP values at a macrolevel (3, 6, and 7].

The relative deviation (RD) of the DP $t_i$ is the difference between the unit of value $x_i$ and the average value $\bar{x}$ of the measurements set related to the mean-square value of this difference or

$$t_i(X) = \frac{x_i - \bar{x}}{s_x}, \tag{1}$$

where $x_i$ is the value of the $i$-measurement of the DP $X$, $\bar{x} = \sum_{i=1}^{n} x_i/n$ is the average value of the set of the DP $X$ $n$ measurements, and $s_x = \sqrt{\frac{\sum_{i=1}^{n}[x_i - \bar{x}]^2}{n-1}}$ is the mean-square deviation in the DP $X$ set of measurements.

The principle of comparison of the RD of $t_i$ allows one to establish the correlation between the regularities of the DP distribution at the macroscopic level by means of the comparison the characteristics of their sets by different ways and methods of estimation. In papers [3, 6, and 7], for estimation of the DP correlation by means of division of the RD of the DP $X_1\ldots X_k$ (e.g., $t_i(X_1)/t_i(X_{2\ldots k})$), the methods of the qualitative comparison of the RD values (more, less) were proposed, and, by means of multiplication (e.g., $t_i(X_1) \times t_i(X_{2\ldots k})$), the methods of qualitative comparison of the RD signs (coincidences, noncoincidences).

The methods of comparison of the RD values are designated by the indicators $A_B$ and $|A|_B$, which can be determined by the equations

$$A_B[X_1(X_2\ldots X_k)] = \sum_{i=1}^{n} C_i \Big/ \sum_{i=1}^{n} |C|_i; \tag{2}$$

$$|A|_B[X_1(X_2\ldots X_k)] = \sum_{i=1}^{n} C'_i \Big/ \sum_{i=1}^{n} |C'|_i, \tag{3}$$

where $|C|_i$ and $|C'|_i$ are the total amounts of the relations between the RD of the DP $X_1\ldots X_k$ sets, correspondingly, for $A_B$ and $|A|_B$, which are presented by the formulas

$$|C|_i = \left|\frac{t_i(X_1)}{t_i(X_2)} - 1\right| + \left|\frac{t_i(X_1)}{t_i(X_3)} - 1\right| + \ldots + \left|\frac{t_i(X_1)}{t_i(X_k)} - 1\right|; \tag{4}$$

$$|C'|_i = \left|\left|\frac{t_i(X_1)}{t_i(X_2)}\right| - 1\right| + \left|\left|\frac{t_i(X_1)}{t_i(X_3)}\right| - 1\right| + \ldots + \left|\left|\frac{t_i(X_1)}{t_i(X_k)}\right| - 1\right|, \tag{5}$$

where $C_i$ and $C'_i$ are the difference of the RD values of the DP $X_1\ldots X_k$ sets, correspondingly, for $A_B$ and $|A|_B$, which are presented by

$$C_i = \left(\frac{t_i(X_1)}{t_i(X_2)} - 1\right) + \left(\frac{t_i(X_1)}{t_i(X_3)} - 1\right) + \ldots + \left(\frac{t_i(X_1)}{t_i(X_k)} - 1\right); \tag{6}$$

$$C'_i = \left(\left|\frac{t_i(X_1)}{t_i(X_2)}\right| - 1\right) + \left(\left|\frac{t_i(X_1)}{t_i(X_3)}\right| - 1\right) + \ldots + \left(\left|\frac{t_i(X_1)}{t_i(X_k)}\right| - 1\right), \tag{7}$$

where $t_i(X_1)/t_i(X_{2\ldots k})$ is the main feature of the division method, and $\frac{t_i(X_1)}{t_i(X_{2\ldots k})} - 1$ and $\left|\frac{t_i(X_1)}{t_i(X_{2\ldots k})}\right| - 1$ are the major features of the comparison method of the RD values for the indicator $A_B$, which presents the difference of the relation, correspondingly, of the RD $i$-unit of the DP $X_1$ and the RD $i$-units of the sets of parameters $X_2\ldots X_k$ and the unit, as well as the difference between the absolute value of the RD relation and the unit.

The formulas $\left|\frac{t_i(X_1)}{t_i(X_{2\ldots k})}\right| - 1$ and $\left|\left|\frac{t_i(X_1)}{t_i(X_{2\ldots k})}\right| - 1\right|$ are the major features of the comparison method of the RD values for the indicator $|A|_B$ and represent, correspondingly, the absolute values of the difference of the RD relation of the $i$-measured unit of the DP $X_1$ with the RD $i$ units of the $X_2\ldots X_k$ sets of the parameters and the unit, as well as the difference of the absolute value of the RD relation and the unit.

The comparison method of the signs can be expressed by the $E_B$ indicator, which is determined by

$$E_B[X_1(X_2\ldots X_k)] = \sum_{i=1}^{n} e_i \Big/ \sum_{i=1}^{n} |e|_i, \tag{8}$$

where $e_i$ is the sum of the RD comparative products of a set of one DP ($X_1$) with the corresponding values of another DP ($X_{2,\ldots k}$) represented by the expression

$$e_i = t_i(X_1)t_i(X_2) + t_i(X_1)t_i(X_3) + \ldots + t_i(X_1)t_i(X_k); \tag{9}$$

where $|e|_i$ is the amount of the RD comparative products of a set of one DP ($X_1$) with the corresponding values of the other DP ($X_{2,\ldots k}$) being represented by the expression

$$|e|_i = |t_i(X_1)t_i(X_2)| + |t_i(X_1)t_i(X_3)| + \ldots + |t_i(X_1)t_i(X_k)|; \tag{10}$$

where $t_i(X_1)t_i(X_{2\ldots k})$ and $|t_i(X_1)t_i(X_{2\ldots k})|$ are the main features of the comparison method of the signs in the $E_B$ indicator represented by the sum of the multiplications of the *i* measured unit of the $X_1$ parameter with *i* units of the $X_2 \ldots X_k$ parameter sets and, correspondingly, its absolute value.

As follows from the analysis of formulas (2–10), the indicators $A_B$, $|A|_B$, and $E_B$ obtain values within the limits of ±1. They allow one to numerically compare the share of the set (of a cathode macrosurface) of one DP ($X_1$) and the RD comparison criterion coinciding with the corresponding values of several DP ($X_{2,\ldots,k}$) with respect to the share of the set with noncoinciding comparison criteria of its RD.

For instance, the value of the $A_B$ indicator points to the numerical difference of the set shares of the measured values (of the cathode macrosurface) in which (at which) the value of the RD of one DP ($X_1$) exceeds the corresponding values with the same sign of the other dispersed parameters ($X_{2,\ldots,k}$) and the ones of lesser values or with an opposite sign. The sign of the $|A|_B$ indicator points to the share of the RD predominant feature in a set (at the cathode surface): a positive sign for larger RD values and a negative one for minor RD values and with an opposite sign.

The value of the $|A|_B$ indicator points to the numerical difference of the set of shares of the measured values (of a cathode macrosurface) in which (at which) the RD absolute value of one DP ($X_1$) exceeds the corresponding and lesser values of the other DPs ($X_{2,\ldots,k}$). The sign of the $|A|_B$ indicator points to the share of the RD predominant feature in the set (at the cathode surface): a positive sign for larger RD values and a negative one for minor RD values.

The value of the $E_B$ indicator shows the numerical difference of the set of shares of the measured values (of the cathode macrosurface) in which (at which) the RD of one DP ($X_1$) have the signs coinciding and noncoinciding with the corresponding values of the other DP ($X_{2,\ldots,k}$). The sign of the $E_B$ indicator points to the share of the predominant feature in the set (at the cathode surface): a positive sign for the coinciding RD features and a negative one for the noncoinciding ones.

Let us point out that the presented indicators of the estimation are not entirely efficient in practice, because the correlation between the DPs is determined with respect to the difference of the shares of the RD features being compared, and, besides, in the calculation of the indicators of the multiple complexes, the principle of "nonexceedance of the minimal values of the binary complexes" (which the latter may comprise) is not always adhered to. Moreover, the values of the indicators of the compared complexes can be significantly influenced by the RD's numerical value.

Taking into consideration all that was mentioned above, the present paper is devoted to the attempts at elaborating other indicators for estimation of the DP correlation that overcome or reduce the effects of the disadvantages of the $A_B$, $|A|_B$, and $E_B$ indicators.

Let us examine in detail the possibilities and limitations of the $A_B$, $|A|_B$, and $E_B$ indicators by the example of the experimental estimation of the DP correlation of a composition iron structure.

**Table 1.** RD in DP sets of the iron composite structure

| DP value measurement points at the cathode | Relative deviations in the DP sets | | | |
|---|---|---|---|---|
| | $t_k$ | $t_m$ | $t_p$ | $t_a$ |
| 1 | ***0.394*** | 0.273 | ***0.806*** | 0.770 |
| 2 | ***–0.134*** | –0.120 | ***–0.157*** | –0.072 |
| 3 | ***0.914*** | 0.991 | ***0.282*** | 0.00024 |
| 4 | ***0.351*** | 0.422 | ***–0.076*** | –0.169 |
| 5 | ***1.231*** | 1.219 | ***0.897*** | 0.494 |
| 6 | ***0.792*** | 0.855 | ***0.259*** | 0.021 |
| 7 | ***–1.249*** | –1.218 | ***–0.991*** | –0.659 |
| 8 | ***–0.638*** | –0.971 | ***1.049*** | 1.626 |
| 9 | ***–1.661*** | –1.451 | ***–2.069*** | –2.013 |

The DP values of the composition structure were obtained on a vertical long length cathode in a flow-through cell [8] at the following electrolysis regime: pH = 0.8; $i_k = 20$ A/dm$^2$; $T = 50$°C; the dispersed phase (DPH) concentration equal to 100 g/l.

The measurements of the DP values were performed at the points homogeneously distributed along the length of the cathode. The counting of the measurement points was performed from the bottom to the top.

For the quality of the DP values for measuring the cathode surface, there were used the $V_k$ (cm$^3$) and their RD $t_{i(k)}$, the iron $V_m$ (cm$^3$) and their RD $t_{i(m)}$, the dispersed phase (DPH) of $V_p$ (cm$^3$) and their RD $t_{i(p)}$, and the volume of the concentration of the DPH $p_v$ (%) and their RD $t_{i(a)}$.

Note that, for the control and the prediction of the formation process of the composite deposits, the estimation of the correlation between the DPH concentration distributed at the cathode and the rest of the parameters of the composition structure is of the most important practical significance.

The result of the analysis of the distribution of the RD $t_i$ of the DP in the composition structure shows that their regularities at the macrolevel are of various characters (see Table 1 and the figure). Note that they make pairs ($t_k - t_m$ and $t_p - t_a$), namely, the RD of the $V_m$ volume of the iron and the RD of the $V_k$ composite deposit, and the RD of the $V_p$ DPH volume and its $p_v$ concentration. It is evident that such a character of the RD distribution points to the fact that certain DP of the composite structure reveal similar regularities of their formation at the cathode.

In order to evaluate the DP correlations by the $A_B$, $|A|_B$, and $E_B$ indicators, binary and multiple complexes of comparison were composed by us:

(1) the DPH concentration – the $K(p_v, V_k)$ composite deposit volume;

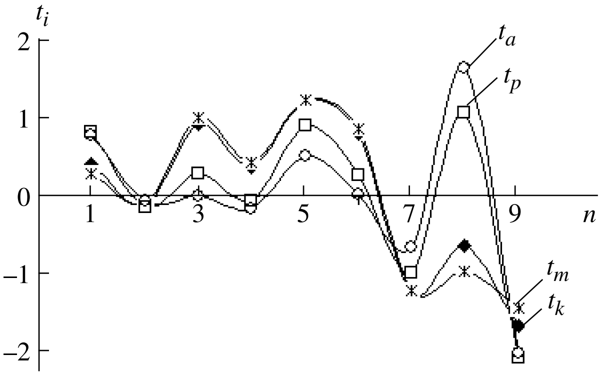

Distribution on the cathode at points $n$ of the relative deviations of the quantity of the electrochemical composition $t_k$, the iron $t_m$, the dispersion phase $t_p$, and its concentration $t_a$.

(2) the DPH concentration—the $K(p_v, V_m)$ metal deposit volume;

(3) the DPH concentration—the $K(p_v, V_p)$ DPH volume in the deposit;

(4) the DPH concentration—the $K|p_v(V_k, V_m, V_p)|$ volumes of the composite, metal, and DPH.

As a result of the correlation estimation by the $A_B$ indicator for the binary complexes of the DPH $p_v$ concentration with other DP of the composition structure, it was determined that the numerical share of the set (of the cathode surface) with a value of the RD $p_v$ exceeding the corresponding values with a similar sign of the $V_k$, $V_m$, and $V_p$ parameters concedes to various degrees with the share of the set of RD $p_v$ with a smaller value and an opposite sign. The $A_B$ indicator for the multiple $p_v$ complex is larger than the least value of its binary complex $K(p_v, V_p)$ (see Table 2).

The correlation estimation by means of $|A|_B$ for the binary complexes shows the numerical share of the set (of the cathode surface) of $p_v$ with the RD absolute value being larger than the corresponding values of the parameters $V_k$, $V_m$, and $V_p$, to a different degree, concedes with the share of the $p_v$ set of the RD with a minor value. The indicator $|A|_B$ for the multiple complex exceeds the least value of the binary complex $K(p_v, V_p)$ by 1.4 times and makes up ~0.8 of the greatest value of the $K(p_v, V_m)$ complex (see Table 2).

The estimation by the $E_B$ indicator for the binary complexes enabled us to determine that the numerical share of the set (of the cathode surface) $p_v$ of the RD with coinciding signs and corresponding values of the $V_k$, $V_m$, and $V_p$ parameters significantly exceeds the share of the RD $p_v$ with opposite signs. The $E_B$ indicator for the multiple complex is greater than the least value of the binary complex $K(p_v, V_m)$ by 1.5 times and makes up ~0.7 of the greatest value of the $K(p_v, V_m)$ complex (see Table 2).

It is evident that, for the multiple complex $K[p_v(V_k, V_m, V_p)]$, the values of the indicators $A_B$, $|A|_B$, and $E_B$ violate the principle of "nonexceedance of the least values" of the binary complexes it comprises.

In connection with the above mentioned and the analysis of the curves of the RD distributions of the composites structure (see Fig.1), the $A_B$, $|A|_B$, and $E_B$ indicators' values may be accepted for the multiple complex $K[p_v(V_k, V_m, V_p)]$ as being equal to the minimum values of the binary complexes they comprise.

We should note that, for the objective checking of the numerical values of such indicators as $A_B$ and $|A|_B$, one can also use the method of converse comparisons, i.e., estimations of the shares of the difference of the DP sets (of the cathode macrosurface) of one DP ($X_1$) with the RD values less than the corresponding values of the other DP ($X_{2,\ldots k}$).

The above problem can be solved if in (4–7) the main principles of the comparison methods are expressed by the converse relations of the denominator and numerator, that is, correspondingly

$$c_i = \left(\frac{t_i(X_2)}{t_i(X_1)} - 1\right) + \left(\frac{t_i(X_3)}{t_i(X_1)} - 1\right) + \ldots + \left(\frac{t_i(X_k)}{t_i(X_1)} - 1\right), \quad (11)$$

$$c_i' = \left(\left|\frac{t_i(X_2)}{t_i(X_1)}\right| - 1\right) + \left(\left|\frac{t_i(X_3)}{t_i(X_1)}\right| - 1\right) + \ldots + \left(\left|\frac{t_i(X_k)}{t_i(X_1)}\right| - 1\right), \quad (12)$$

$$|c|_i = \left|\frac{t_i(X_2)}{t_i(X_1)} - 1\right| + \left|\frac{t_i(X_3)}{t_i(X_1)} - 1\right| + \ldots + \left|\frac{t_i(X_k)}{t_i(X_1)} - 1\right|, \quad (13)$$

**Table 2.** Correlation estimation by the indicators $A_B$, $|A|_B$, and $E_B$ for the DP volumes of the composite deposit $V_k$, the metal $V_m$, the DPH $V_p$, and the concentration DPH $p_v$

| Correlation indicators | Comparison complexes (a slash separates their values relative to the multiple complex) | | | |
|---|---|---|---|---|
| | $K(p_V, V_k)$ | $K(p_V, V_m)$ | $K(p_V, V_p)$ | $K[p_V, (V_k, V_m, V_p]$ |
| $A_B$ | –0.76/**1.3** | –0.545/0.9 | –0.303/0.5 | –0.58 |
| $\|A\|_B$ | –0.194/0.9 | –0.166/0.8 | –0.303/**1.4** | –0.213 |
| $E_B$ | 0.655/**1.1** | 0.493/**1.5** | 1.000/0.7 | 0.731 |

**Table 3.** Correlation estimation by the indicators $a_B$, $|a|_B$ for the DP volumes of the composite deposit $V_k$, the metal $V_m$, the DPH $V_p$, and the concentration DPH $p_v$

| Correlation indicators | Comparison complexes (a slash separates their values relative to the multiple complex) | | | |
|---|---|---|---|---|
| | $K(p_v, V_k)$ | $K(p_v, V_m)$ | $K(p_v, V_p)$ | $K[p_v, (V_k, V_m, V_p]$ |
| $a_B$ | 0.997/1.0 | 0.997/1.0 | 0.998/1.0 | 0.997/1.0 |
| $\|a\|_B$ | 0.999/1.0 | 0.999/1.0 | 0.998/1.0 | 0.999/1.0 |

**Table 4.** Correlation estimation by the indicators $A_B$, $|A|_B$, $a_B$, and $|a|_B$ for the DP volumes of the composite deposit $V_k$, the metal $V_m$, the DPH $V_p$, and the DPH concentration $p_v$ calculated for the RD

| Correlation indicators | Comparison complexes (a slash separates their values relative to the multiple complex) | | | |
|---|---|---|---|---|
| | $K(p_v, V_k)$ | $K(p_v, V_m)$ | $K(p_v, V_p)$ | $K[p_v, (V_k, V_m, V_p]$ |
| $A_B$ | –0.754/**1.3** | –0.536/1.0 | –0.199/0.4 | –0.561 |
| $\|A\|_B$ | –0.169/1.0 | –0.142/0.9 | –0.199/**1.2** | –0.166 |
| $E_B$ | 0.646/**1.1** | 0.469/**1.5** | 1.0/0.7 | 0.726 |
| $a_B$ | 0.562/1.0 | 0.527/**1.1** | 0.737/0.8 | 0.568 |
| $\|a\|_B$ | 0.877/1.0 | 0.881/1.0 | 0.737/1.2 | 0.859 |

$$|c'|_i = \left|\left|\frac{t_i(X_2)}{t_i(X_1)}\right| - 1\right| + \left|\left|\frac{t_i(X_3)}{t_i(X_1)}\right| - 1\right| + \ldots + \left|\left|\frac{t_i(X_k)}{t_i(X_1)}\right| - 1\right|. \quad (14)$$

In this case, we obtain new indicators of the DP correlation estimation of the electrochemical system expressed by the equations

$$a_B[X_1(X_2\ldots X_k)] = \sum_{i=1}^{n} c_i \Big/ \sum_{i=1}^{n} |c|_i; \quad (15)$$

$$|a|_B[X_1(X_2\ldots X_k)] = \sum_{i=1}^{n} c'_i \Big/ \sum_{i=1}^{n} |c'|_i. \quad (16)$$

From the analysis of (11–16), it follows that the indicators $a_B$ and $|a|_B$ obtain values within the limits of ±1. Their value points to the numerical difference of the shares of the measured sets of values (of the cathode macrosurface) in which (at which) the RD value of one DP ($X_1$) is less than the corresponding values and of the same sign (of the absolute values for $|a|_B$) of the other DP ($X_{2,\ldots k}$) and greater values (and with the opposite sign for $a_B$). The sign of the indicators $a_B$ and $|a|_B$ shows the share of the predominant feature in the set (at the cathode surface): a positive sign shows the RD minimum values, and a negative sign shows greater values.

By estimation of the $a_B$ and $|a|_B$ indicators of the correlation for the DP composition structure, it was determined that the share of the distribution at the cathode (in the set) of the RD in the DPH concentration with the values conceding with the corresponding volume values of the compositions $V_k$, the metal $V_m$, and the DPH $p_v$ completely concedes with the share of the surpassed values. Besides, the values of the $a_B$ and $|a|_B$ indicators of the multiple complexes of comparison are within the limits of the minimum values of the binary complexes they comprise (see Table 3).

It is evident that the values of the $a_B$ and $|a|_B$ indicators feebly reflect the regularities of the reciprocal distributions of the RD (presented in Table 1 and in the figure) and the correlation with the $A_B$ and $|A|_B$ indicator values (see Table 2). The values of the $a_B$ and $|a|_B$ indicators seem to be considerably influenced by certain private relations between the RD of the DP that exceed by several orders the main multitude of the RD relations. For example, the RD value of the DPH concentration at point 3 is several orders less than the RD of the other DP (see Table 1). In connection with this, the comparative RD relations $t_i(X_1)/t_i(X_{2\ldots k})$ at the given point provide numbers that significantly prevail over all the rest of the comparative relations of the observed complexes.

Note that the above discrepancies can be partially eliminated by means of the reduction of the RD values of the DP sets to one order.

For instance, in Table 4, one can find the values of the $A_B$, $|A|_B$, $a_B$, and $|a|_B$ indicators for the RD of one order. The analysis of their values displays that they qualitatively correlate with the numerical and graphical distributions at the cathode of the RD DP composition structure (see Table 1 and the figure).

Note also that the reciprocal estimation of the DP correlations (according to the difference of the shares of the RD features being compared) creates certain difficulties in the apprehension of the numerical comparisons of their results, e.g., positive values of the $a_B$, and

**Table 5.** Correlation estimation by the indicators $+A_B$, $+|A|_B$, $+a_B$, and $+|a|_B$ for the DP quantity of the composite deposit $V_k$, the metal $V_m$, the DPH $V_p$, and the DPH concentration $p_v$

| Correlation indicators | Comparison complexes (a slash separates their values relative to the multiple complex) | | | |
|---|---|---|---|---|
| | $K(p_v, V_k)$ | $K(p_v, V_m)$ | $K(p_v, V_p)$ | $K[p_v, (V_k, V_m, V_p]$ |
| $+A_B$ | 12.3/**0.0** | 23.2/**0.0** | 40.0/**0.0** | 0.00 |
| $+\|A\|_B$ | 23.7/0.7 | 10.0/**1.6** | 12.4/**1.3** | 15.7 |
| $+a_B$ | 78.1/1.0 | 76.4/1.0 | 85.8/**1.1** | 78.3 |
| $+\|a\|_B$ | 88.6/1.0 | 87.3/1.0 | 85.8/1.0 | 87.6 |
| $+E_B$ | 82.7/0.9 | 74.1/**1.1** | 77.6/1.0 | 78.1 |

$|a|_B$ indicators and negative ones of the $A_B$ and $|A|_B$ indicators.

In this respect, the above-mentioned difficulties can be overcome if the correlation estimation is carried out with respect to the share of the RD feature being compared. Such a problem can be solved by summarizing the singular similar sign comparisons in (6), (7), (9), (11), and (12) and reflecting them relative to the total volume of the measurement sets, i.e.,

$$^{+}C_i = {}^{+}\left(\frac{t_i(X_1)}{t_i(X_2)} - 1\right) + {}^{+}\left(\frac{t_i(X_1)}{t_i(X_3)} - 1\right) + \ldots + {}^{+}\left(\frac{t_i(X_1)}{t_i(X_k)} - 1\right); \tag{17}$$

$$^{+}|C|'_i = {}^{+}\left(\left|\frac{t_i(X_1)}{t_i(X_2)}\right| - 1\right) + {}^{+}\left(\left|\frac{t_i(X_1)}{t_i(X_3)}\right| - 1\right) + \ldots + {}^{+}\left(\left|\frac{t_i(X_1)}{t_i(X_k)}\right| - 1\right); \tag{18}$$

$$^{+}c_i = {}^{+}\left(\frac{t_i(X_2)}{t_i(X_1)} - 1\right) + {}^{+}\left(\frac{t_i(X_3)}{t_i(X_1)} - 1\right) + \ldots + {}^{+}\left(\frac{t_i(X_k)}{t_i(X_1)} - 1\right), \tag{19}$$

$$^{+}|c|'_i = {}^{+}\left(\left|\frac{t_i(X_2)}{t_i(X_1)}\right| - 1\right) + {}^{+}\left(\left|\frac{t_i(X_3)}{t_i(X_1)}\right| - 1\right) + \ldots + {}^{+}\left(\left|\frac{t_i(X_k)}{t_i(X_1)}\right| - 1\right), \tag{20}$$

$$^{+}e_i = {}^{+}[t_i(X_1)t_i(X_2)] + {}^{+}[t_i(X_1)t_i(X_3)] + \ldots + {}^{+}[t_i(X_1)t_i(X_k)]. \tag{21}$$

In this case, substituting (17) into (2), (18) into (3), (19) into (8), (20) into (15), and (21) into (16), we obtain the new indicators of the correlation, which can take values from 0 to 1 (or 0–100%) and be defined by the equations

$$^{+}A_B[X_1(X_2\ldots X_k)] = \sum_{i=1}^{n} {}^{+}C_i \Big/ \sum_{i=1}^{n} |C|_i \times 100\%; \tag{22}$$

$$^{+}|A|_B[X_1(X_2\ldots X_k)] = \sum_{i=1}^{n} {}^{+}|C'|_i \Big/ \sum_{i=1}^{n} |C|'_i \times 100\%, \tag{23}$$

$$^{+}a_B[X_1(X_2\ldots X_k)] = \sum_{i=1}^{n} {}^{+}c_i \Big/ \sum_{i=1}^{n} |c|_i \times 100\%; \tag{24}$$

$$^{+}|a|_B[X_1(X_2\ldots X_k)] = \sum_{i=1}^{n} {}^{+}|c'|_i \Big/ \sum_{i=1}^{n} |c|'_i \times 100\%, \tag{25}$$

$$^{+}E_B[X_1(X_2\ldots X_k)] = \sum_{i=1}^{n} {}^{+}e_i \Big/ \sum_{i=1}^{n} |e|_i \times 100\%. \tag{26}$$

The analysis of the values of $+A_B$, $+|A|_B$, $+a_B$, $+|a|_B$, and $+E_B$ shows that, for the binary complexes, their values correspond to the graphical distribution of the RD of the composition structure, and, for the multiple complexes, they are much closer to the minimum values of the binary complexes (see Table 5 and the figure).

For example, on the basis of the analysis of the $+A_B$ indicator values, one can state that, for the coinciding signs of the RD of the DP composition, the distribution inhomogeneity of the DPH is greater than the inhomogeneity of its other components at the surface, making up from 12.3 to 40% of the cathode. However, as for the absolute values of the RD of the DPH ($+|A|_B$) concentration, the given region decreases and ranges from 10 to 23.7% of the cathode (see the figure and Table 5).

The analysis of the $+a_B$ values shows that, for the coinciding signs of the RD of the DP composition, the heterogeneity of the distribution of the DPH concentration is greater than the one of the other composition components at the cathode surface (from 76.4 up to 85.8%).

The analysis of the $+E_B$ values shows that the regularities of the DPH concentration distribution relative to its average value coincide with the corresponding regularities of the distribution for the other DP of the composition structure at the cathode region from 74.1 up to 82.7% (see the figure and Table 5).

Thus, on the basis of the correlation indicators $+A_B$, $+|A|_B$, $+a_B$, $+|a|_B$, and $E_B$, one can thoroughly examine the regularities of the formation process of the multicomponent electrochemical deposits at the macroscopic level of the cathode and apply their values for the control and prediction of the deposits' functional structure.

## CONCLUSIONS

As a result of the analysis of the available indicators of the correlation of the macroscopic distribution of the multicomponent electrochemical deposits, there are offered new indicators based on the principle of comparison of the relative deviations from the average values of the measurement sets of the dispersed parameters of objects.

The elaborated indicators reflect the correlation between the dispersed parameters with respect to the share in a set (at the cathode macrolevel) of the compared feature of the relative deviations and allow for the objective checking of their estimation by other indicators. Moreover, they enable one to thoroughly investigate the process of the formation of multicomponent electrochemical deposits at the cathode macrolevel and to apply their values for the control and prediction of the functional structure of the deposits.

## REFERENCES

1. Gur'yanov, G.V., Electroosazhdenie iznosostoikikh kompozitsii (Electrodeposition of Wear Resistant Compositions), Chisinau: Shtiintsa, 1985.
2. Bortsoi, T.V., Wear Resistance and Optimal Structure of Galvanic Composites, Surf. Eng. Appl. Electrochem., 2005, no. 4, pp. 19–23.
3. Bortsoi, T.V., Estimation of Dispersed Parameters at Electrochemical Deposit Formation, Surf. Eng. Appl. Electrochem., 2008, no. 1, pp. 14–20.
4. Vagramyan, A.T., and Solov'eva, Z.A., Metody issledovaniya elektroosazhdeniya metallov, Moscow: USSR AS, 1960.
5. Melkov, M.P., Shevtsov, A.N., and Melkova, I.M., Vosstanovlenie avtomobil'nykh detalei tverdym zhelezom (Automobile Parts Restoration by Hard Iron), Moscow: Transport, 1982.
6. Bortsoi, T.V., Statistical Methods of Estimation of Electrochemical System Parameters Correlation with Dipersed Values at the Electrode, Surf. Eng. Appl. Electrochem., 2006, no. 4, pp. 24–36.
7. Bortsoi, T.V., On possibility of Development of Statistical Methods of Estimation of Dispersed Parameters of Electrochemical Deposits at Macrolevel, Surf. Eng. Appl. Electrochem., 2007, no. 5, pp. 67–74.
8. Bortsoi, T.V., MD Inventor's Certificate no. 1674, BOPI, 2001, no. 5.

ISSN 1068-3755, Surface Engineering and Applied Electrochemistry, 2009, Vol. 45, No. 5, pp. 382–386. © Allerton Press, Inc., 2009.
Original Russian Text © N.I. Kuskova, V.Yu. Baklar', S.A. Khainatskii, 2009, published in Elektronnaya Obrabotka Materialov, 2009, No. 5, pp. 39–43.

ELECTRICAL PROCESSES
IN ENGINEERING AND CHEMISTRY

# Obtaining Ultrafine Metal Powders under Electric Explosion of Conductors in Liquid: Part III. The Optimum Mode for Explosion of Conductors in Gases; Comparison with Explosion in Liquid

**N. I. Kuskova, V. Yu. Baklar', and S. A. Khainatskii**

*Institute of Pulse Processes and Technologies, National Academy of Sciences of Ukraine,*
*Oktyabr'skii pr. 43-a, Nikolaev, 54018 Ukraine*
*e-mail: defr@iipt.com.ua*

Received May 5, 2009

**Abstract**—The electric explosion of nickel-containing conductors is experimentally studied for the optimum mode in air. The results of explosion of conductors in air and in water are compared. It is shown that explosion in air of conductors completely identical to those exploded in water leads to a change in the discharge duty. The conditions required for the optimum mode of explosion of conductors in air are determined.

**DOI:** 10.3103/S106837550905007X

It is found [1, 2] that calculated values of the mean size of particles that appear under an electric explosion of conductors (EEC) in liquid are minimal for the optimum modes of explosion; herein, they depend only on the properties of the metal instead of external controllable parameters of the discharge circuit and conductors. This fact results from the circumstance that the two most important energy parameters of explosion–specific stored energy $W_0/m$ and ratio of conductor metal sublimation energy to stored energy $W_s/W_0$ for optimum modes of EEC–do not depend either on length or diameter of the conductor or on initial voltage $U_0$, capacitor bank capacitance $C$, or circuit induction $L$ [1]. Sizes of the particles obtained in the process of EEC were calculated, as in the first part of [2], by the approximation formula for EEC in gases [3]. It is shown in this work that the number average diameter of the particles obtained by EEC in gases depends on the ratio of the density of the energy injected into the conductor to the sublimation energy of the metal.

With regard to previous results, the aim of this study is to find optimum parameters of EEC in air, to determine the nature of differences and similarity with optimum parameters of EEC in water as well as possible causes of these differences. This will allow revealing how the surrounding environment influences the particle sizes under EEC.

The technical aspects of the experiment technique were the same as in the second part of the article. The operating procedure was as follows. According to known relations [4] for a certain set of electrotechnical parameters, we found the optimum sizes for explosion of a nickel or nickel–chromium conductor in water. Subsequently, a conductor with the same parameters was exploded in the air. Finally, for the same electrotechnical parameters, we found the geometrical dimensions of the conductor for which the mode of electric explosion (EE) in air was also maximally close to the matched one. The search for the matched mode for each of the conductors was carried out by means of variation in its length at constant diameter in an *RLC* circuit with the following parameters: the initial voltage on the capacitor bank $U_0 = 9$ kV, the capacitor bank capacitance $C = 6$ μF, and the discharge circuit inductance $L = 3.32$ μH.

## EXPERIMENTAL RESULTS

Tables 1–4 present the results of explosion of conductors with completely identical sets of parameters in water and in air (herein, the mode of EEC in water is matched) and the results of EEC in air in the optimum mode. Therefore, the first column of the tables indicates metals of exploded conductors with indices corresponding to these situations. Herein, index "2" corresponds to the dimensions of a conductor exploded in water in the optimum mode for the aforementioned set of values of electrotechnical parameters; therefore, it is preserved. Index "3" denotes results of EEC for the same parameters in air; index "4" denotes EEC in air for parameters closer (with respect to oscillograms of current and voltage) to optimum ones.

Table 1 gives the calculated and experimental characteristics of exploded conductors: diameter $d$; length $l$; similarity criteria $S_1$, $S_2$, and $S_3$; ratio of the stored energy $W_0$ to the exploded conductor weight $m$. The similarity criteria, as well as values of optimum length and diame-

**Table 1**

| Metal | *d*, mm | *l*, mm | $S_1$ | $S_2$ | $S_3$ | $W_0/m$, kJ/g |
|---|---|---|---|---|---|---|
| $Ni_2$ | 0.3 | 38 | 0.149 | 0.151 | 0.04 | 10.34 |
| $Ni_3$ | 0.3 | 38 | 0.149 | 0.151 | 0.04 | 10.34 |
| $Ni_4$ | 0.3 | 50 | 0.165 | 0.151 | 0.07 | 7.86 |
| $NiCr_2$ | 0.3 | 28 | 0.7 | 2.34 | 0.02 | 15.3 |
| $NiCr_3$ | 0.3 | 28 | 0.7 | 2.34 | 0.02 | 15.3 |
| $NiCr_4$ | 0.3 | 55 | 1.27 | 23.4 | 0.08 | 7.81 |

ter, were calculated by the formulas [4] for EEC in water. For this set of parameters, according to [4], the optimum diameter $d_{opt}$ is 0.28 mm for a nickel conductor and 0.55 mm for a nickel–chromium one. According to [4], the optimum length does not depend on the conductor material; therefore, for EEC in water, at the circuit parameters selected, it is identical—38 mm. The optimum ratio of the stored energy to the conductor weight $W_0/m_{opt}$ calculated by [5] is 11.98 kJ/g for nickel and 3.325 kJ/g for nickel–chromium. Hence, for the experiments with nickel, conductors with $d = 0.3$ mm and $l =$ 38 mm were taken initially. The form of oscillograms of current and voltage, as well as the value of the stored energy to the conductor weight ratio, confirms that this mode of explosion of a nickel conductor in water is close to optimum. For a nickel–chromium conductor, the mode in which the conductor length was 28 mm appeared to be closer to optimum. This is apparently due to the great difference in values of the optimum and real ($d = 0.3$ mm) diameter of the conductor.

According to [4], the criteria $S_1$ and $S_3$ are identical for conductors of identical length; $S_2$ is identical for all conductors of the same material, because the diameter of wires was not varied in these experiments. Thus, the electrical characteristics (current and voltage) must coincide for explosion of similar conductors in water and in air and they must differ strongly for explosion of a conductor with greater length ($Ni_4$ and $NiCr_4$). In actual fact, the comparison of obtained oscillograms of current and voltage counts in favor of significant differences in the oscillograms under explosion of similar conductors in water and in air, minimal under EEC in water, and considerably longer in air. Under EE in air of a nickel conductor with the parameters fully corresponding to those of the matched mode of EEC in water, the pattern of current decrease at the instant of explosion varies; a region corresponding to the arc stage of discharge appears—the discharge becomes a decaying periodic one. On the contrary, under explosion in air of a longer conductor, the discharge mode becomes aperiodic, sufficiently close in its characteristics to the matched mode. As has already been mentioned in the first part of article [2], in the relations according to which the optimum length and diameter of a conductor are determined, as well as in similarity criteria, the parameters of the surrounding environment are absent. The experimental data given in Table 1 show that the dependence of EE characteristics on the aggregative state of the environment surrounding the conductor exists all the same; hence, it is not quite correct to use these relations for EEC in air. This is confirmed by the form of oscillograms of current and voltage.

The significant increase in the value of the criterion $S_3$ under explosion of a nickel conductor in air in a mode close to the optimum one (with respect to the form of oscillograms) and the difference of the experimental value of the $W_0/m$ ratio from the one found in the previous part of the work for the optimum mode allow us to conclude that, in order to obtain optimum parameters, we must reduce the conductor's diameter. Thus, for the determination of optimum parameters of a conductor exploded in air according to parameters of explosion in water, it is necessary to increase the conductor length by approximately a factor of 1.35 and to decrease its diameter by approximately a factor of 1.12–1.13.

The nickel–chromium conductor in general exhibited the same tendencies, although the results are not as obvious as for nickel. This is due to the circumstance that, for the experiments, we used a conductor whose diameter for the given set of parameters differed considerably from the optimum one. The found mode close to the optimum was implemented for the conductor length being twofold longer than for the similar mode in water. In addition, the $W_0/m$ ratio appeared to be almost half as much. The pattern of oscillograms for nickel–chromium conductors differs from similar modes for nickel conductors. Instead of sharp breaks at the stage of conductor melting, which are characteristic of nickel, the voltage oscillograms exhibit smooth bends under explosion of the nickel–chromium conductor; however, a region of voltage decrease is also present. On the other hand, the bend on current oscillograms at the stage of explosion is sharper. The experiments with nickel–chromium conductors confirm that, in order to obtain the optimum mode of EEC in air, similar to EEC in water, we must increase the conductor length and reduced its diameter.

The time and amplitude characteristics of the process of explosion are presented in Table 2.

The time until voltage peak $t_{expl}$ under explosion of conductors of both metals under the transition from

**Table 2**

| Metal | $t_{\text{expl}}$, μs | $I_{\text{m}}$, kA | $U_{\text{m}}$, kV | $N_{\text{m1}}$, MW | $N_{\text{m2}}$, MW | $R_{\text{m}}/R_0$ | $\bar{U}_m$ | $\bar{U}_m^e$ | $\bar{I}_m$ | $\bar{I}_m^e$ |
|---|---|---|---|---|---|---|---|---|---|---|
| $Ni_2$ | 9.56 | 8.99 | 9.45 | 40.7 | 40 | 93.4 | 3.2 | 1.05 | 0.8 | 0.74 |
| $Ni_3$ | 9.39 | 9.31 | 12.74 | 40 | 59 | 93.4 | 3.2 | 1.42 | 0.8 | 0.77 |
| $Ni_4$ | 3.39 | 8.39 | 11.64 | 36 | 22 | 41.3 | 3.85 | 1.29 | 0.8 | 0.69 |
| $NiCr_2$ | 8.05 | 7.32 | 10 | 27.6 | 55 | 4.3 | 5.04 | 1.11 | 0.4 | 0.605 |
| $NiCr_3$ | 8.55 | 7.35 | 14.6 | 30 | 69 | 5.6 | 5.04 | 1.62 | 0.4 | 0.607 |
| $NiCr_4$ | 9.6 | 6 | 16.9 | 32 | 43 | 12.2 | 7.99 | 1.88 | 0.4 | 0.496 |

water to air varied insignificantly, in fact, less than the experimental error (the oscillograph sweep in these experiments was 5 μs/div). The variations in the maximum amplitude of current pulse $I_m$, by comparison of explosion of similar conductors in water and in air, are analogous to the variations under the transition to the shorter (other conditions being equal) conductor; for the optimum mode in air, the decrease in amplitude is due to the real increase in the conductor length. The same also concerns the peak value of voltage $U_m$. This also confirms the conclusion made above.

The power injected into nickel and nickel–chromium conductors has two maxima due to the presence of breaks in the voltage oscillograms. The first maximum $N_{m1}$ is achieved at the instant of voltage break approximately corresponding to incipient melting. For the EEC in water in the optimum mode, it is comparable in value with the second ("explosion") peak $N_{m2}$; that is, the exploded conductor resistance is in agreement with the characteristic resistance of the discharge circuit, providing a maximum of power two times during the active stage of discharge. Under explosion of a similar conductor in the air, it is less by one-third; for explosion of the conductor in air in the optimum mode, it exceeds the "explosion" peak by almost 40%; that is, the matching occurs precisely at this instant (the time when the resistances are equal is very short—on the order of $10^{-8}$ s; the energy dissipation in the conductor must be maximum precisely in this short period of time). This is the feature that makes the EEC in nickel crucially different from explosion of other conductors, for example, copper and aluminum.

Under explosion of nickel–chromium conductors containing approximately 80% nickel, the ratios of peaks in the power curve are not comparable with the ones described above. The power peak, which corresponds to the melting stage with respect to time, is considerably lower (on average, half as much) than the "explosion" one. For other nickel-containing materials used by us in the experiments (VZh100 and EI868 steels), all the processes occur in approximately the same fashion as in "standard" conductors, despite the relatively high—on the order of 50–60%—content of nickel.

According to the maximum power injected into conductor, it is possible to estimate the influence of the surrounding environment on parameters of EEC. One can see from the data of Table 2 how it increases under EEC in air. For Ni, this increase is almost 50%; for NiCr, it is approximately 25%. The dynamic resistance of water to the conductor broadening in the pre-explosion stage hinders the increase in the conductor resistance owing to enlargement of its cross section, which accordingly decreases the peak of inductive overvoltage and the reactive component of the maximum power injected into the conductor. If we compare the values of power given in Table 2 with the maximum power that can be injected into the resistive load in the *RLC* circuit equal to $N_{\max} = \frac{1}{2}U_0^2C^{1/2}L^{-1/2} \cong 54.5$ MW, then the values of $N_{m2}$ for Ni and NiCr look obviously uncompensated.

The last four columns of Table 2 contain dimensionless experimental values of the overvoltage peak $\bar{U}_m^e = U_m/U_0$ and maximum current of the first half-wave $\bar{I}_m^e = \frac{I_m}{U_0}\sqrt{\frac{L}{C}}$, as well as their approximate values obtained by the similarity theory methods in [4] ($\bar{U}_m \approx 15S_2^{1/4}S_3^{1/3}$ and $\bar{I}_m \approx 0.5S_2^{-1/4}$) that allow specifying the required correction of the optimum diameter and length of the conductor as well as the criteria $S_2$ and $S_3$ under EEC in air. Thus, the comparison of $\bar{I}_m$ and $\bar{I}_m^e$ for nickel confirms the necessity to decrease the optimum diameter of the conductor by approximately a factor of 1.12 and criterion $S_2$ by a factor of 1.6. The comparison of the dimensionless values of maximum current and voltage allows us to conclude that it is necessary to increase the optimum length by a factor of 1.35 and to decrease $S_3$ by approximately a factor of 3.

For a nickel–chromium conductor, not all is as clear as for a nickel one. The presented data partially confirm the conclusions and partially do not. It is not improbable that not all table data used by us for calculations of the conductor characteristics correspond to the properties of the material of wires applied in the experiments.

**Table 3**

| Metal | $W_1$, J | | $W_2$, J | | $W_3$, J | | $W_4$, J | | $W_s$ | | |
|---|---|---|---|---|---|---|---|---|---|---|---|
| | Exp. | Theor. | Exp. | Theor. | Exp. | Theor. | Exp. | Theor. | Exp. | Theor. | |
| | | | | | | | | | | *b* | *s* |
| $Ni_2$ | 5.25 | 14.99 | 23.11 | 7.13 | 46.2 | 13.9 | 141.4 | 152.4 | 216 | 188.4 | 266.1 |
| $Ni_3$ | 13.1 | 14.99 | 8.5 | 7.13 | 15.4 | 13.9 | 172.9 | 152.4 | 209.8 | 188.4 | 266.1 |
| $Ni_4$ | 19.2 | 19.7 | 11.1 | 9.4 | 19.1 | 18.3 | 128.1 | 200.5 | 177.4 | 247.9 | 350.1 |
| $NiCr_2$ | 19.7 | 10.9 | 14.5 | 5.1 | 34.6 | 11.2 | 98.6 | 118.8 | 167.4 | 145.9 | 203.6 |
| $NiCr_3$ | 9.8 | 10.9 | 10.9 | 5.1 | 16.6 | 11.2 | 148 | 118.8 | 185.4 | 145.9 | 203.6 |
| $NiCr_4$ | 18.3 | 21.4 | 13.8 | 9.95 | 28.2 | 21.9 | 157.7 | 233.3 | 185.3 | 286.5 | 400 |

Table 3 gives experimental and calculated values of the energy released in conductors at different stages of explosion: $W_1$ is the conductor heating up to the melting temperature; $W_2$ is the melting (latent heat of melting); $W_3$ is the heating to boiling; $W_4$ is the boiling; $W_s$ is the energy required for complete evaporation of the conductor (sublimation energy). $W_s$ was calculated for two probable scenarios of the process—equilibrium evaporation (designated with letter “b”) and spinodal decomposition (designated with letter “s”).

The explosion of a nickel conductor in the air, with the parameters fully corresponding to the matched mode of explosion in water, leads to a decrease in the amount of the energy released in the conductor by the instant of explosion. Herein, the redistribution of stored energy over a region that is small with respect to amplitudes and duration (up to one period), which is usually attributed to the arc stage of discharge, takes place. The increase in the conductor length up to 50 mm leads, as is mentioned above, to the disappearance of this region; that is, the total stored energy (or most of it) is released in the first half-period of discharge. The amount of energy released in the conductor by the instant of the voltage peak decreases to values lower than is necessary for the evaporation of the total material of the conductor even under equilibrium boiling. Similar results for explosion of wires of refractory metals are described in [6]. Herein, by the instant of explosion of a nickel conductor in liquid (in the optimum mode), they release a higher amount of energy than is necessary for equilibrium boiling. One can see from the data of Table 3 that, in this case, the point corresponding to the beginning of explosion in the state diagram is situated between the liquid–vapor equilibrium curve (bimodal) and the system lability curve (spinodal). This is one more significant difference in the conditions of EEC in liquid and in gases. In terms of this work, we do not discuss the mechanism of destruction of a conductor under EE; however, the conclusion suggests itself that, in the absence (or at very low value) of dynamic resistance of the surrounding environment, the decisive role can be played by intrinsic dynamic properties of the metal “dispersed” owing to heat expansion at very rapid (up to $10^9$ K/s) Joule heating. Thereupon, the “ashy” mechanism proposed in [6] can really take place. In this case, the size of obtained particles must be considerably higher than under EEC in liquid—on the order of hundreds of nanometers. The total amount of energy released in the conductor at the active stage of discharge decreases.

Under explosion of a nickel–chromium conductor, the distribution of injected energy (conductor enthalpy) with respect to explosion phases is approximately the same. This is confirmed by the data of Table 4, which gives some energy ratios: the ratio of energy injected into the conductor by the instant of explosion (experimental and calculated) to the stored energy $W_{expl}/W_0$ and the sublimation energy $W_{expl}/W_s$ and the maximum possible ratio of the sublimation energy to the stored energy in the optimum mode for each of the conductors calculated by [5]. One can see from the last ratio that the explosion mode in which the energy equal to or higher than the sublimation energy is injected into the conductor by the instant of explosion is possible for a nickel conductor and impossible for a nickel–chromium one. However, in our opinion, the value of this ratio seems to be overestimated owing to probable inaccuracy of tabular data for it.

The last column presents the calculated value of the mean size of particles obtained under explosion. As in [1], the calculation was carried out by the relations obtained in [3]. All the calculations in Table 4 are given for one scenario of thermal destruction of the conductor, because, as is shown above, the scenario of spinodal destruction under explosion of nickel and particularly nickel–chromium conductors is of low probability. As one can see, for “optimum” modes of EEC in air, values of particle dimensions increased sharply. This cannot be due to the change in the mechanism of conductor destruction, because this mechanism is not included in relations for determination of particle dimensions [3]. Most probably, this is one more confirmation of the fact

**Table 4**

| Metal | $W_{expl}/W_0$ | | | $W_{expl}/W_s$ | | $(W_s/W_0)_{opt}$ | $\bar{a}$, $10^{-6}$ m |
|---|---|---|---|---|---|---|---|
| | Exp. | Theor. | | | | | |
| | | *b* | *s* | *b* | *s* | | |
| $Ni_2$ | 0.89 | 0.78 | 1.1 | 1.15 | 0.81 | 0.809 | 0.2 |
| $Ni_3$ | 0.86 | 0.78 | 1.1 | 1.11 | 0.79 | ″ | 0.22 |
| $Ni_4$ | 0.73 | 1.02 | 1.44 | 0.72 | 0.51 | ″ | 0.82 |
| $NiCr_2$ | 0.69 | 0.6 | 0.84 | 1.15 | 0.82 | 2.77 | 0.2 |
| $NiCr_3$ | 0.76 | 0.6 | 0.84 | 1.27 | 0.91 | ″ | 0.15 |
| $NiCr_4$ | 0.9 | 1.2 | 1.6 | 0.76 | 0.54 | ″ | 0.68 |

that, for obtaining the "real" optimum mode of EEC in the air, it is necessary to vary the dimensions of the exploded conductor with higher precision, in the first place, its diameter.

## CONCLUSIONS

It is found in the work that the aggregative state of the surrounding medium influences the mode of EEC owing to difference in densities. Thus, it is shown that the explosion in air of conductors whose dimensions exactly coincide with the optimum (for a certain set of electrotechnical parameters) dimensions for water, calculated by the relations of [4], leads to the change in the discharge duty from aperiodic (matched) to attenuated periodic.

For the optimum mode of EEC in the air, it is required to correct values of their dimensions: the length must be increased by approximately a factor of 1.35 in comparison with the calculated length for water; the diameter must be decreased by approximately a factor of 1.12–1.13. The similarity criteria which characterize the explosion and arc stages of explosion also need to be corrected. The criterion $S_2$ must be decreased by a factor of 1.6; $S_3$ must be decreased by approximately a factor of 3.

The variation in the aggregative state of the surrounding environment affects the rate and amount of energy injected into the conductor as well as, probably, the change in the mechanism of its destruction.

No direct influence of variation in the density of the surrounding environment on the mean dimensions of conductor metal particles obtained under explosion has been found by us.

## REFERENCES

1. Khainatskii, S.A., Conditions for Realization of an Optimum Regime of the Electric Explosion of Conductors in Liquid Media, *Pis'ma Zh. Tekh. Fiz.*, 2009, vol. 35, issue 7, pp. 15–20 [*Tech. Phys. Lett.* (Engl. Transl.), vol. 35, no. 4, p. 299].
2. Kuskova, N.I., Baklar', V.Yu., Gordienko, V.I., and Khainatskii, S.A., On Obtaining of Ultrafine Metal Powders at Electric Explosion of Conductors in Liquid. Part I: Peculiarities of Explosion of Conductors in Liquid, *Elektron. Obrab. Mater.*, 2008, no. 1, pp. 44–50 [*Surf. Eng. Appl. Electrochem.* (Engl. Transl.), vol. 44, no. 1, p. 36].
3. Kotov, Yu.A. and Yavorskii, N.A., Research of Particles Formed at the Electric Explosion of Conductors, *Fiz. Khim. Obrab. Mater.*, 1978, no. 4, pp. 24–29.
4. Krivitskii, E.V., *Dinamika elektrovzryva v zhidkosti* (The Dynamics of Electric Explosion in Liquid), Kiev: Naukova Dumka, 1986.
5. Khainatskii, S.A., Conditions for Realization of an Optimum Regime of the Electric Explosion of Conductors in Liquid Media, *Tech. Phys. Lett.*, 2009, vol. 35, no. 4, pp. 299–301.
6. Lebedev, S.V. and Savvatimskii, A.I., Metals in the Process of Rapid Heating by High Density Electric Current, *Usp. Fiz. Nauk*, 1984, vol. 144, issue 2, pp. 215–250.

ISSN 1068-3755, Surface Engineering and Applied Electrochemistry, 2009, Vol. 45, No. 5, pp. 387–389. © Allerton Press, Inc., 2009.
Original Russian Text © I.V. Kholodkov, 2009, published in Elektronnaya Obrabotka Materialov, 2009, No. 5, pp. 44–47.

# Energy Distribution of Ions in Near-Cathode Regions of Glow Discharge in an Argon–Oxygen Mixture

**I. V. Kholodkov**

*GOUVPO Ivanovo State Chemical and Technological University, pr. F. Engel'sa 7, Ivanovo, 153000 Russia*
*e-mail: kholodkov@isuct.ru*

Received April 23, 2009

**Abstract**—Investigation results are presented for the ion energy distribution in the cathode region of direct current discharges in argon–oxygen mixtures containing 0–100% argon at different plasma parameters (a pressure of 1.0–3.0 Pa and a discharge current of 10.0–30.0 mA). It has been shown that an argon percentage of more than 20% results in the $Ar^{2+}$ ion formation and shifting the distribution maximum to higher energies.

**DOI:** 10.3103/S1068375509050081

## INTRODUCTION

From the technological point of view, cathode discharge regions are of great importance for etching and cleaning of materials and depositing of films for different purposes. At that, the reactions induced by ion bombardment play a great role. One of the possible ways to optimize the etching and cleaning processes is the use of mixtures of chemically active gases with argon as the plasma-forming gas. To make a forecast for the effectiveness of similar technological processes, one must have information on the type of ions, the ion flow value, and the ion energy distribution function (IEDF). From this point of view, cathode discharge regions are much less studied than the positive column region [1, 2], as investigations are conducted either for pure gases [3, 4] or model systems with highly intensive ion sources [5].

## EXPERIMENTAL TECHNIQUE

The investigations were performed using the installation whose scheme is shown in Fig. 1.

To measure the ion energy distribution, a cylindrical electrostatic sector-type analyzer focused to 127° and placed directly behind the cathode was used [6]. A discharge was created in an S-52 electrovacuum molibden glass cylindrical reactor with an internal diameter of 125 mm. The near-cathode potential distribution was measured using a single probe (the overall distance between the electrodes was 250 mm).

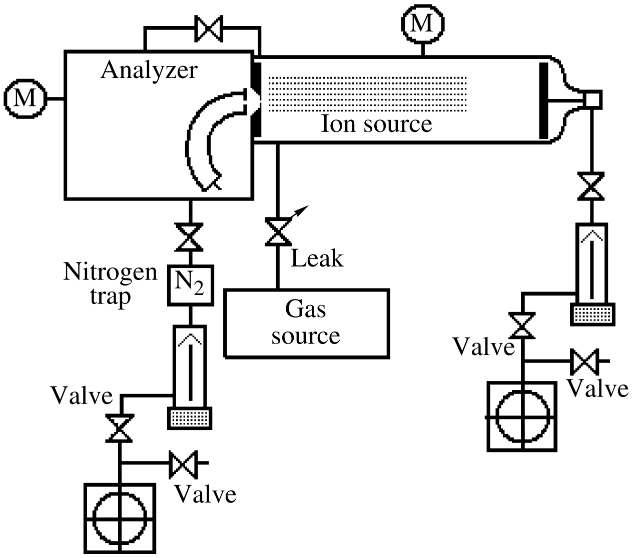

**Fig. 1.** Experimental installation scheme.

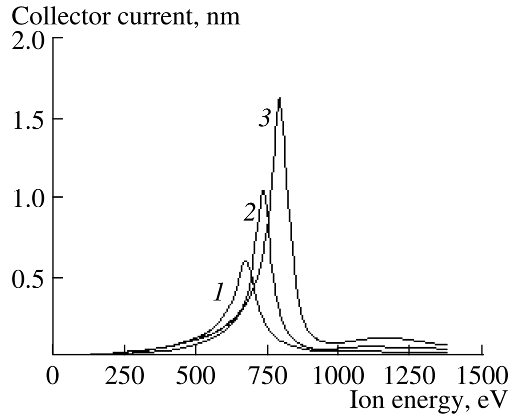

**Fig. 2.** The ion energy distribution function at 1.5 Pa and 20 mA: (*1*) 100% $O_2$; (*2*) 10% $O_2$; (*3*) 100% Ar.

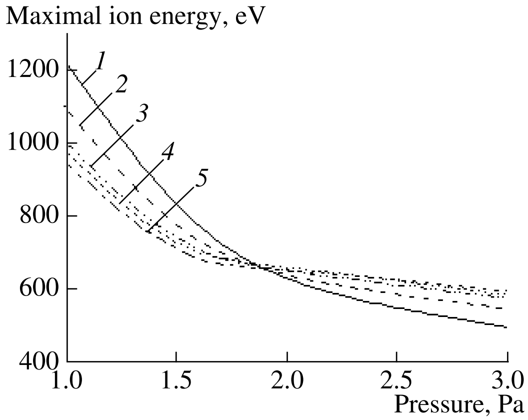

**Fig. 3.** Maximal energy dependency on the plasma-forming gas pressure at 20 mA: (*1*) 100% Ar; (*2*) 10% $O_2$; (*3*) 60% $O_2$; (*4*) 80% $O_2$; (*5*) 100% $O_2$.

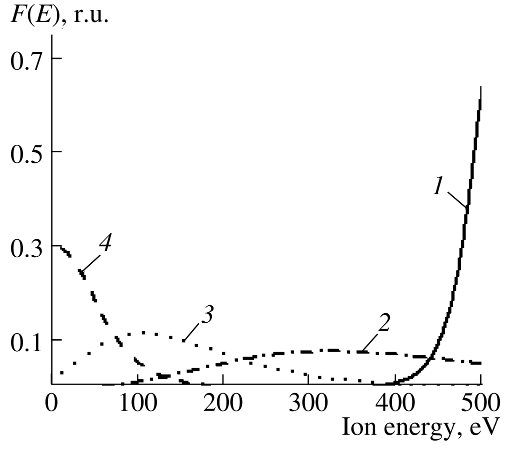

**Fig. 4.** Ion energy distribution functions calculated in the framework of the simplified model for the motion of positive ions in the cathode region at the following pressures, Pa: (*1*) 1.5; (*2*) 10; (*3*) 20; (*4*) 50. The cathode potential fall equals 500 V.

The gas mixture pressure interval was 1.0–3.0 Pa, and the discharge current was changed within the limits of 10.0–30.0 mA. The plasma-forming gas was prepared by mixing argon and oxygen in certain volumes (the gas purity was 99.9%), and the accuracy of the mixture preparation was controlled using mass spectrometry.

## MEASUREMENT RESULTS AND THEIR DISCUSSION

The obtained ion energy distribution functions looked like curves with a single maximum in the high-energy region (Fig. 2). As a result of the experiments performed, the IEDF maximum location's dependency on the pressure and plasma-forming gas composition was revealed (Fig. 3). The oxygen addition within the limit of 20% has the most essential effect. It should be noted that the maximal ion energy almost does not depend on the mixture's composition at a pressure of 1.8 Pa.

The form of the observed dependencies can be explained if it is supposed that the sharp maximum of the curve is defined by the ions that have passed the cathode potential fall region without collisions and gained the highest energy, and the smooth descending curve to the lower energies is caused by the ions that have endured collisions inside this region during the recharging processes [7]. The results of the IEDF calculations on the basis of Davis's resonance recharging model [3] and the resonance recharging section data [8, 9] under the assumption that all the ions are enclosed between two boundaries without any ions being located outside and where the total ion flow is the same are shown in Fig. 4. The cathode's potential fall value was assumed to be constant and equal to 500 V.

The calculations performed confirm that, in our case, the ions produced as a result of the recharging form a small plateau near the main maximum and the IEDF form is actually defined by the near-cathode potential distribution.

In order to draw conclusions about the ionic composition, the energies that an ion can gain passing the whole cathode region without any collisions were estimated on the basis of the potential distribution measurements in the cathode region (Fig. 5). From the comparison of Figs. 3 and 5, one can conclude that double-charged ions predominate in pure argon at a pressure of 1 Pa, while the distribution function maximum corresponds to single-charged ions in pure oxygen and its mixtures with argon at a pressure of more than 1.5 Pa.

## CONCLUSIONS

As a result of the experimental investigations performed, data were obtained on the energy distribution of the positive ions arriving at the cathode in a glow discharge in an argon–oxygen mixture. It was shown that

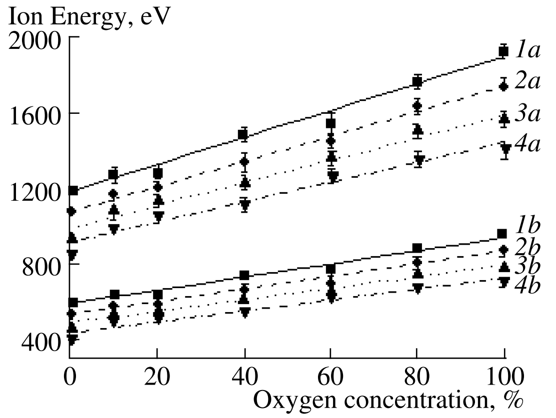

**Fig. 5.** Dependency of the energy imparted to single- and double-charged ions in the cathode region on the oxygen concentration in the mixture. Double-charged ions: (*1a*) 1 Pa, (*2a*) 1.5 Pa, (*3a*) 2 Pa, (*4a*) 3Pa; single-charged ions: (*1b*) 1 Pa, (*2b*) 1.5 Pa, (*3b*) 2 Pa, (*4b*) 3Pa; the discharge current is 20 mA.

the Davis resonance recharging model taking into account the measured potential distribution in a dark cathode space satisfactorily describes the experimental distribution functions representing curves with a single maximum at an energy of several hundred eV. From the obtained data, it follows that, in the cathode fall region, both single- and double-charged ions can be present in an argon–oxygen mixture; at that, the latter predominant at an oxygen concentration of less than 20% and at a plasma-forming mixture pressure of less than 1.5 Pa.

## REFERENCES

1. Smirnov, S.A., Rybkin, V.V., Ivanov, A.N. and Titov, V.A., The Simulation of the Process of Formation and Decay of Neutral Particles in DC Discharge Plasma in an Argon–Oxygen Mixture, *High Temperature*, 2007, vol. 45, no. 3, pp. 291–297.
2. Morscheidt, W., Hassouni, K., Bauduin, N., Arefi-Khonsari, F. and Amouroux, J., On the Use of Global Kinetics Models for the Investigation of Energy Deposition and Chemistry in RF Argon–Oxygen Plasmas Working in the Torr Regime, *Plasma Chemistry and Plasma Processing*, 2003, vol. 23, no. 1, pp. 117–140.
3. Davis, W.D. and Vanderslice, T.A., Ion Energies at the Cathode of a Glow Discharge, *Physical Review*, 1963, vol. 131, no. 4, pp. 219–228.
4. Healy, D. and Brandt, W.W., Ion Extraction from the Cathode-Fall Region of Ar, $N_2$ and $O_2$ Discharges, *Int. J. Mass. Spectrom. Ion Proc.*, 1986, vol. 70, pp. 267–275.
5. Wronski, Z., Energy Distributions of Cathode Fall Ions in the Light of Boltzmann Equation, *Vacuum*, 1990, vol. 40, no. 4, pp. 387–394.
6. Sokolov, V.F. and Sokolova, Yu.A., Energy Distribution Measurement for Positive Ions, Bombarding a Cathode, *Poverkhnost', rentgenovskie, sinkhrotronnye i neitronnye issledovaniya*, 2004, no. 8, pp. 77–80.
7. Raizer, Yu.P., Contemporary Level of Understanding Phenomena in the Cathode Parts of Glow Discharge, *Teplofisika visokikh temperature*, 1986, vol. 4, no. 5, pp. 984–994.
8. Fedorenko, N.V., Ionization at Collision of Ions with Atoms, *Uspekhi fizicheskikh nauk,* 1959, vol. 118, no. 3, pp. 481–511.
9. Thomson, J.B., Electron Energy Distribution in Plasmas. IV. Oxygen and Nitrogen, *Proc. Roy. Soc.*, 1961, vol. A 262, pp. 503–518.

ISSN 1068-3755, Surface Engineering and Applied Electrochemistry, 2009, Vol. 45, No. 5, pp. 390–396. © Allerton Press, Inc., 2009.
Original Russian Text © L.Z. Boguslavskii, 2009, published in Elektronnaya Obrabotka Materialov, 2009, No. 5, pp. 48–56.

## ELECTRICAL PROCESSES IN ENGINEERING AND CHEMISTRY

# Engineering Method of Calculating the Technological Parameters of Pulse Corona Discharge in Strong Electrolytes: I. Single-Point Electrode Systems

**L. Z. Boguslavskii**

*Institute of Pulse Processes and Technologies, National Academy of Sciences of Ukraine,*
*pr. Oktyabr'skii 43-a, Nikolaev, 54018 Ukraine*
*e-mail: iipt@iipt.com.ua*

Received June 3, 2009

**Abstract**—An engineering method is suggested for calculating the pulse corona discharge technological parameters: the maximal pressure on the boundary of the continuous plasma formation and its radius, the maximal pressure on the front of the compression wave, and the electroacoustic discharge efficiency for the external adjustable parameters selected for a pulse generator included in a technological electric-discharge installation. In the first part of the work the method of calculating the parameters for a single-point electrode system is described.

**DOI:** 10.3103/S1068375509050093

## INTRODUCTION

A pulse corona discharge (PCD) in conductive liquids under certain conditions is characterized by the rather high intensity of the hydrodynamic disturbance compared at least with that generated by an underwater spark discharge. Such a hydrodynamic feature is inherent to PCD in strong aqueous electrolytes, for which a branched corona turns into continuous plasma formation (CPF) [1–3]. At that, the possibility is opened up to form a pressure field of specified configuration in the liquid both at the expense of the electrode-point geometry and a larger number of points on which discharges are struck simultaneously [4]. This has predetermined the interest in PCD for engineers developing technological applications of electric explosions in liquids, especially where the treated object is placed in an aggressive highly conductive media [5, 6].

For PCD with CPF, a number of mathematical models consisting of complex sets of nonlinear integral and differential equations in partial derivatives that rather closely describe the processes in a discharge gap, the dynamics of the CPF and transitional plasma–liquid layer, and the nonuniform energy dissipation in the electrolyte were suggested [5, 7]. The calculation of similar models requires high computational capacities, and, as a rule, the ready software products existing today are not able to solve the posed problem in full measure. In connection with this, one has to resort to obtaining analytical dependencies, although they decrease the accuracy of the process description due to the accepted simplifying assumptions; however, the speed of the computation by these models sufficiently satisfies engineers designing electric discharge equipment.

The given article is devoted to the engineering method of calculating the PCD technological parameters: the maximal pressure on the CPF boundary and its radius, the maximal pressure on the compression wave front at the distance of the CPF, and the electroacoustic discharge efficiency for the external adjustable parameters selected for a pulse generator included in a technological electric-discharge installation. In the first part of the work, the method of calculating the parameters for a single-point electrode system is described.

## PROBLEM STATENENT

In the problem formulation, as in [7], the following assumptions are introduced.

(1) The plasma formation is a semispherical layer located on the positive point-electrode base, which can be considered as a solid wall. Redoubling the source energy in compliance with the specular reflection principle [2], one can model the process dynamics, while solving a spherically symmetric task. At that, the equivalent active resistances for the individual elements of the discharge gap–plasma region $R_a$ and the electrolyte layer $R_l$ must be calculated for the semispherical layers.

(2) The plasma formation is uniform by its pressure and temperature, as the characteristic time of their equalization $\tau_{P,T} \sim a/c_a$ (the CPF radius $a \sim 10^{-3}$ m and the sound velocity in plasma $c_a \approx 3000$ m/s) is low in comparison with that of the CPF radius change $\tau_a \sim a/\dot{a}$ ($\dot{a} < 1000$ m/s [8]).

(3) The energy losses from the CPF due to the irradiation and heat conductivity are low [2], and so these constituents will not be taken into consideration in the energy balance equations.

(4) For the plasma formation, the spark approximation [9]

$$P_a = A_s(\gamma - 1)\sigma_a, \tag{1}$$

relating the pressure $P$ and the electroconductivity $\sigma_a$ is true at the values of the spark constant $A_s$ and the effective adiabat exponent of the discharge plasma $\gamma$ corresponding to that of the underwater spark discharge [5].

(5) The expansion of the CPF occurs in an unlimited medium, and this is justified for the times $t < 2(r_s - a)/c_0$, which are less than the time necessary for a compression wave reflected from the chamber wall to reach the CPF boundary ($c_0$ is the sound velocity in the electrolyte).

(6) The process of the discharge striking is excluded from consideration, so, for the PCD with CPF, the corona striking time and the amount of electric energy expended at this stage are incommensurably low in comparison with the characteristic time and discharge energy, correspondingly [3]. Consequently, the time will be reckoned from the moment of the corona striking, and the initial conditions for the CPF radius and voltage for the discharge gap will be written in the form

$$a(0) = r_{\text{el}}, \quad U(0) = U_0, \tag{2}$$

where $r_{\text{el}}$ is the rounding-off radius for the electrode point, and $U_0$ is the condenser battery voltage.

After the CPF strikes, the pressure rises sharply inside it, and the CPF, expanding, force out the surrounding liquid. As $\dot{a}$ is less than the sound velocity in liquid, the compressibility of the latter can be taken into account in a quasi-acoustic approximation, and the equation of motion for the CPF boundary, on which the mass-transfer between the liquid and CPF contents takes place, can be written in the following way [10]:

$$a\frac{d\nu_g}{dt}\left(1 - 2\frac{\nu_g}{c_0}\right) + \frac{3}{2}\nu_g^2\left(1 - \frac{4}{3}\frac{\nu_g}{c_0}\right) + \frac{P_0 - P_a(t)}{\rho_0} - \frac{a}{\rho_0 c_0}\left(1 - \frac{\nu_g}{c_0}\right)\frac{dP_a(t)}{dt} = 0, \tag{3}$$

where $\rho_0$ is the equilibrium liquid density.

The energy balance equation taking into account the volume of the CPF in the form of the semi-spherical layer $V(t) = 2\pi(a^3 - r_{\text{el}}^3)/3$ and the accepted assumptions has been put into the following form:

$$\frac{2\pi a^2(t)}{(\gamma - 1)}\left[\gamma P_a(t)\frac{da(t)}{dt} + \frac{1}{3}a(t)\frac{dP_a(t)}{dt}\right] = N_a(t), \tag{4}$$

where the power $N_a(t) = I^2R_a$ generated in the CPF is expressed in terms of the CPF radius' function defined through equation (3), the current $I$ in the discharge circuit, and the plasma resistance $R_a$. The discharge current is given by the circuit equation

$$L\frac{dI}{dt} + \frac{1}{C}\int_0^t I dt + I(R_a + R_l) = U_0, \tag{5}$$

where the resistance $R_a$ in the approximation of the uniformity for the plasma properties along the CPF radius has the form [7]

$$R_a = \frac{1}{2\pi a\sigma_a}\left(\frac{a(t)}{r_{\text{el}}} - 1\right). \tag{6}$$

## DETERMINATION OF THE MAXIMAL PCD PARAMETERS AND THE ELECTROACOUSTIC EFFICIENCY

When the maximal power that corresponds to the maximal pressure for the PCD [5] is reached, by the time moment $t_m$, the parameters will take the following values: $a(t) = a_m$; $P_a(t) = P_{am}$; $N_a(t) = N_{am}$; $da_m/dt_m = v_{am}$. From (4) we will get

$$P_{am} = \frac{(\gamma - 1)}{2\pi\left(\gamma + \frac{1}{3}\right)}\frac{N_{am}}{a_m^2\nu_{am}}. \tag{7}$$

From the equation of the CPF boundary motion (3) under the assumptions $\frac{\nu_{am}}{c_0} < 1$ and $\frac{a_m}{t_m} \approx \nu_{am}$, one can obtain

$$P_{am} = \frac{5\rho_0 a_m\nu_{am}}{2t_m\left(1 + \frac{v_{am}}{c_0}\right)}. \tag{8}$$

Whence, substituting $a_m$ into (7), we get

$$P_{am} = \left(\frac{25(\gamma - 1)N_{am}\rho_0^2\nu_{am}}{8\pi\left(\gamma + \frac{1}{3}\right)t_m^2\left(1 + \frac{\nu_{am}}{c_0}\right)^2}\right)^{1/3}. \tag{9}$$

The power of the electrical energy that has been generated in the CPF by the moment $t_m$ is defined as

$$N_{am} = I_m^2 R_{am}, \tag{10}$$

where $I_m$ and $R_m$ are the current and resistance for the CPF at the time moment $t_m$.

The maximal discharge current that is applicable for our calculations corresponding to the maximal power is defined by the type of condenser discharge on the load. According to [11], in a circuit with the capacity $C$ and inductance $L$, it is determined by the damping decrement

$$\delta = \frac{R_n}{2}\sqrt{\frac{C}{L}}, \tag{11}$$

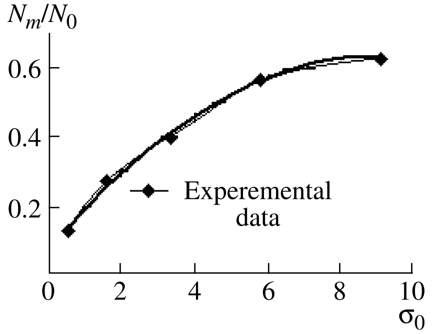

**Fig. 1.** Polynomial dependency of the negative power maximum on the electrolyte electroconductivity where $y = -0.0071x^2 + 0.1259x + 0.0739$.

where $R_n$ is the resistance of the load.

In the case of $\delta < 1$, the discharge will be oscillating, at $\delta \approx 1$ it will be critical, and at $\delta > 1$ it is aperiodic. For the PCD, the load resistance is a nonlinear value, and so the damping decrement can be approximated by the initial discharge gap resistance:

$$\delta = \frac{1}{4\pi\sigma_0 r_{\text{el}}}\sqrt{\frac{C}{L}}. \tag{12}$$

The critical and aperiodic discharge modes will be mainly realized for the PCD. For them, according to [11], when the nonlinear load resistance is linearized by the initial one, the following equation

$$I_m = \frac{U_0}{e}\sqrt{\frac{C}{L}}, \tag{13}$$

corresponds to the critical discharge and the equation

$$I_m = U_0\sqrt{\frac{C}{L}}B^{-\frac{\delta}{\sqrt{\delta^2-1}}}, \tag{14}$$

where $e$ is the natural logarithm base, $U_0$ is the charge voltage for the condenser, and $B = \delta + \sqrt{\delta^2 - 1}$, corresponds to an aperiodic discharge. The time that is necessary to attain the maximal current is $t_m = \sqrt{LC}$ for the critical discharge, and that for an aperiodic discharge is

$$t_m = \frac{\sqrt{LC}}{\sqrt{\delta^2 - 1}} lnB. \tag{15}$$

According to the latter, the time $t_m$ must shift to lower values for an aperiodic discharge. However, according to the experimental data [5], this is not observed for the maximal power due to the nonlinearity of the discharge gap resistance. Nevertheless, for engineering calculations with an error of no more than 10%, equation (15) can be accepted.

By the time moment $t_m$, the CPF resistance will assume the form

$$R_{am} = \frac{A_s(\gamma - 1)}{2\pi P_{am}a_m}\left(\frac{a_m}{r_{\text{el}}} - 1\right). \tag{16}$$

Thus, the power for a critical discharge can be represented as

$$N_{am} = \frac{A_s(\gamma - 1)U_0^2 C}{2\pi e^2 LP_{am}a_m}\left(\frac{a_m}{r_{\text{el}}} - 1\right) \tag{17}$$

and that for an aperiodic discharge can be represented as

$$N_{am} = \frac{A_s(\gamma - 1)U_0^2 C}{2\pi B^{\frac{2\delta}{\sqrt{\delta^2-1}}} LP_{am}a_m}\left(\frac{a_m}{r_{\text{el}}} - 1\right). \tag{18}$$

Substituting (17) or (18) into (9) and taking into account that $a_m/r_{\text{el}} > 1$, we get

$$P_{am} = \left(\frac{25(\gamma - 1)^2 A_s U_0^2 k\rho_0^2 \nu_{am}}{16\pi^2\left(\gamma + \frac{1}{3}\right)L^2 r_{\text{el}}\left(1 + \frac{\nu_{am}}{c_0}\right)^2}\right)^{1/4}, \tag{19}$$

where $k = e^{-2}$ for a critical discharge and $k = B^{\frac{-2\delta}{\sqrt{\delta^2-1}}}$ for an aperiodic discharge.

The analysis of the obtained equation (19) indicates a weak dependency of $P_{am}$ on the initial liquid conductivity (only through the parameter $\delta$). However, the experimental data [5] point to a rather strong dependency of the power for the Joule dissipation of the energy that is generated in the discharge gap on $\sigma_0$. In Fig. 1, the experimental maximal power dependency on the initial conductivity and its trend curve are shown. Therefore, for the correctness of the calculations, we introduce the term $k^*\sigma_0$ into Eq. (19), where, at $k^* = 0.126$ m/Sm, the maximal trend curve coefficient is taken:

$$P_{am} = \left(\frac{25(\gamma - 1)^2 A_s U_0^2 k\rho_0^2 \nu_{am} k^*\sigma_0}{16\pi^2\left(\gamma + \frac{1}{3}\right)L^2 r_{\text{el}}\left(1 + \frac{v_{am}}{c_0}\right)^2}\right)^{1/4}. \tag{20}$$

In Eq. (20), a single parameter remains undefined; it is the CPF expansion velocity $\nu_{am}$ by the time moment $t_m$. According to the experimental data [12], within the liquid electroconductivity interval of $2 < \sigma_0 < 9$ Sm/m, the CPF expansion velocity does not change (right up to the maximal current), has nearly identical values for all the cases, and equals 1000 m/s.

We determine the CPF radius by the moment when the maximal current is reached from (8) and, using the obtained equation (20), find

$$a_m = \left( \frac{(\gamma - 1)^2 A_s U_0^2 C^2 k_{am} k^* \sigma_0 \left(1 + \frac{\nu_{am}}{c_0}\right)^2}{25\pi^2 \left(\gamma + \frac{1}{3}\right) r_{\text{el}} \rho_0^2 \nu_{am}^3} \right)^{1/4}. \quad (21)$$

By analogy with the determination of the compression wave parameters from that for a plasma cavity [13] at the distance $r$ from the spherical symmetry axis (the electrode rounding-off center) in an acoustic approximation, we obtain the pressure distribution at the moment when the maximal power is reached:

$$P_m = \frac{P_{am}}{\bar{r}}, \quad (22)$$

where $\bar{r} = \frac{r}{a_m}$, and $r$ changes from $a_m$ to the object of the technological treatment.

Then, at the energy $W_0 = \frac{CU_0^2}{2}$ accumulated in the condenser, we obtain the following equation:

$$P_m = \frac{(\gamma - 1)}{2\pi r} \left( \frac{2A_s W_0 k k^* \sigma_0}{\left(\gamma + \frac{1}{3}\right) r_{\text{el}} \nu_{am} L} \right)^{1/2}. \quad (23)$$

Analysis of dependency (23) shows that the pressure on the compression wave front rises with an increase in the accumulated energy $W_0$ and the liquid electroconductivity $\sigma_0$ and with a decrease in the inductance $L$ and the initial electrode radius $r_{\text{el}}$, thus corresponding to the known experimental facts. Also, our attention is engaged by the fact that, for the spherical symmetry corresponding to the CPF at the PCD, during the expansion of the compression wave, the pressure decreases with the distance following the law $\frac{1}{r}$, and this is essentially faster than it is for the cylindrical symmetry of the underwater spark channel, which obeys the law $\frac{1}{\sqrt{r}}$ [13]. Hence, to maintain an appropriate pressure in technologies with PCD, it is necessary to bring the working electrode as close as possible to the treated object.

Checking of the obtained equation will be conducted by the results of the comparison between the calculated and experimental data [14] (Fig. 2). From the presented results, good agreement is observed for the calculated and experimental data at least at low condenser charge voltages, and this also points to the correctness of the obtained dependencies (20) and (21), which are included in (23). No reliable experimental data exist on the determination of the pressure in the near-field zone of the PCD with the CPF for voltages $U_0 \sim 50$ kV.

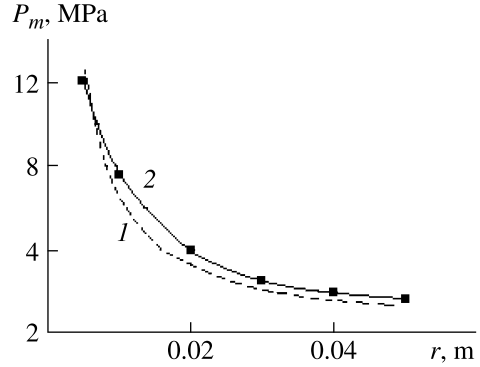

**Fig. 2.** Comparison between the experimental and calculated data on the pressure on the compression wave front for the parameters $U_0 = 15$ kV, $C = 1$ μF, $L = 2.4$ μH, $r_{\text{el}} = 5$ mm, and $\sigma_0 = 5$ Sm/m. (*1*) calculated data; (*2*) experimental data.

The PCD electroacoustic efficiency defining the fraction of energy that has been transferred to the acoustic one $W_{\text{ac}}$ is determined as [14]

$$\eta = \frac{W_{\text{ac}}}{W_0}, \quad (24)$$

where $W_0$ is the energy accumulated in the condenser. The acoustic energy is calculated by the equation

$$W_{\text{ac}} = \frac{4\pi r^2}{\rho_0 c_0} \int_0^\infty P^2(t)\,dt. \quad (25)$$

In [13], the dependency was obtained for the acoustic energy on $P_m$ for the time when the pressure decreases by 10 times:

$$W_{\text{ac}} = \frac{4\pi r^2}{\rho_0 c_0} \frac{P_m^2 0.74 \tau \sqrt[4]{r}}{2 ln(10)}, \quad (26)$$

where $\tau$ is the time of the energy generation.

Substituting (26), (21), and (23) into Eq. (24) at $\tau = \sqrt{LC}\sqrt{\delta^2 - 1}$, we get for the acoustic aperiodic PCD efficiency

$$\eta = \frac{0.32(\gamma - 1)^2 A_s k k^* \sigma_0 r^{\frac{1}{4}} \sqrt{\delta^2 - 1}}{\left(\gamma + \frac{1}{3}\right)\left(\rho_0 c_0 r_{\text{el}} \nu_{am} a_m^{\frac{1}{4}} \sqrt{\frac{L}{C}}\right)}. \quad (27)$$

## ENGINEERING CALCULATION METHOD

The initial parameters defining the PCD mode are the condenser charge voltage $U_0$, the condenser capacity $C$, the accumulated condenser energy $W_0$, the dis-

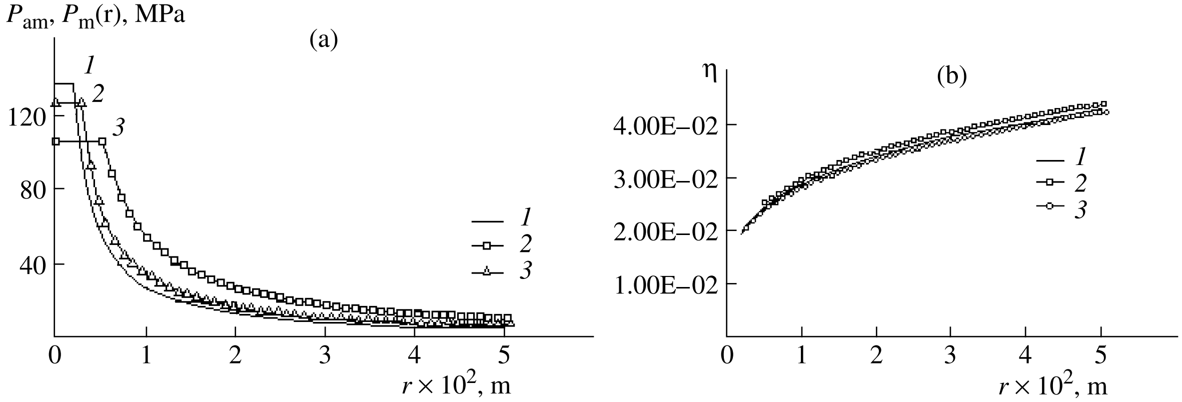

**Fig. 3.** Calculated maximal pressures on the plasma cavity wall $P_{am}$ and on the compression wave front $P_m(r)$ (a) and the PCD electroacoustic efficiency (b) for different electrode radii, depending on the distance to the CPF at $C = 2$ μF, $U_0 = 50$ kV, $L = 6$ μH, $\sigma_0 = 2.2$ Sm/m: (*1*) $r_{\rm el} = 1.75$ E-03 m, (*2*) $r_{\rm el} = 2.5$ OE-03 m, and (*3*) $r_{\rm el} = 5.0$ OE-03 m.

charge circuit inductance $L$, the electrolyte electroconductivity $\sigma_0$, the electrode rounding-off radius $r_{\rm el}$, the distance between the symmetry center and the treated object $r$, and electrolyte density $\rho_0$.

The constants and physical parameters used in the calculations are the spark constant $A_s = 10^5$ (V$^2$ s)/m$^2$, the sound velocity in water $c_0 = 1400$ m/s, the percussive adiabat exponent $\gamma = 1.26$, the coefficient taking into account the influence of the electrolyte electroconductivity $k^* = 0.126$ m/Sm, and the CPF expansion velocity by the maximal current moment $v_{am} = 10^3$ m/s.

### *Calculation of the PCD characteristics*

**Step I.** Calculating the conditions for the production of PCD with CPF from the data [16]

$$\beta = \frac{\sigma_0 U_0^2 (LC)^{\frac{2}{3}}}{\rho_0 r_{\rm el}^4}.$$

If $\beta > 0.2$, the PCD with the CPF will be obtained; if $\beta < 0.2$, it is necessary to change the external adjustable parameters $U_0$, $C$, and $r_{\rm el}$ to get a PCD with CPF.

**Step II.** Calculate the electrical discharge mode by (12)

$$\delta = \frac{1}{4\pi\sigma_0 r_{\rm el}}\sqrt{\frac{C}{L}}.$$

If $\delta \approx 1$, the coefficient $k = e^{-2}$ should be chosen, and, in the case of $\delta > 1$, one should take $k = B^{\frac{-\delta}{\sqrt{\delta^2-1}}}$, where $B = \delta + \sqrt{\delta^2 - 1}$.

**Step III.** Calculate the maximal pressure on the CPF boundary by (20)

$$P_{am} = \left(\frac{25(\gamma-1)^2 A_s U_0^2 k \rho_0^2 \nu_{am} k^* \sigma_0}{16\pi^2\left(\gamma+\frac{1}{3}\right)L^2 r_{\rm el}\left(1+\frac{\nu_{am}}{c_0}\right)^2}\right)^{1/4}. \qquad (28)$$

**Step IV.** Calculate the CPF radius corresponding to the maximal power by (21)

$$a_m = \left(\frac{(\gamma-1)^2 A_s U_0^2 C^2 k_{am} k^* \sigma_0\left(1+\frac{\nu_{am}}{c_0}\right)^2}{25\pi^2\left(\gamma+\frac{1}{3}\right) r_{\rm el}\rho_0^2\nu_{am}^3}\right)^{1/4}.$$

**Step V.** Calculate the maximal pressure on the compression wave front by (22)

$$P_m(r) = \frac{P_{am}(a_m + r_{\rm el})}{r}.$$

**Step VI.** Calculate the electroacoustic efficiency for the PCD with CPF by (27)

$$\eta = \frac{0.32(\gamma-1)^2 A_s k k^* \sigma_0 r^{\frac{1}{4}}\sqrt{\delta^2-1}}{\left(\gamma+\frac{1}{3}\right)\rho_0 c_0 r_{\rm el}\nu_{am} a_m^{\frac{1}{4}}\sqrt{\frac{L}{C}}}.$$

The results of the calculations by the suggested method are presented in Fig. 3 for the maximal pressure distribution over the PCD plasma cavity (the flat segments of the dependencies), over the compression wave front (Fig. 3a), and for the electroacoustic discharge efficiency at different point-electrode radii (Fig. 3b). The conditions $\beta > 0.2$ and $\delta >$ are met for the parameters of the discharge circuit and the medium, and this corresponds to the chosen CPF model. An increase in the point radius leads to a reduction in the amplitude of

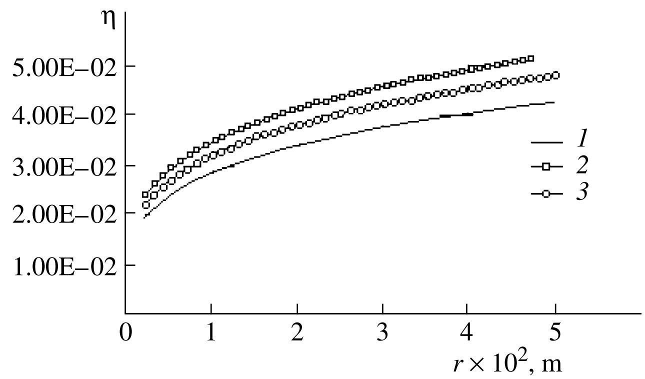

**Fig. 4.** PCD electroacoustic efficiency for different condenser capacities depending on the distance to the CPF at $r_{el}$ = 0.00175 m, $U_0$ = 50 kV, $L$ = 6 μH, $\sigma_0$ = 2.2 Sm/m. (*1*) $C$ = 2.0 OE-06 F, (*2*) $C$ = 4.0 OE-06 F, and (*3*) $C$ = 6.0 OE-06 F.

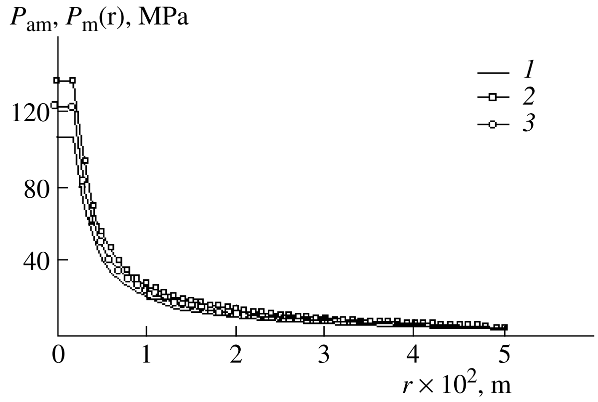

**Fig. 5.** Calculated maximal pressures on the plasma cavity wall $P_{am}$ and on the compression wave front $P_m(r)$ at $r_{el}$ = 0.00175 m, $C$ = 2 μF, $U_0$ = 50 kV, $L$ = 6 μH, $\sigma_0$ = 2.2. Sm/m for different charge voltages: (*1*) $U_0$ = 30000 V, (*2*) $U_0$ = 40 000 V, and (*3*) $U_0$ = 50000 V.

the pressure in the CPF, though, at that, a higher pressure extends for a longer distance from CPF. The electroacoustic discharge efficiency slightly depends on the electrode radius, increases with the distance from the CPF, and lies within the limits of 2–4%. The dependencies of the electroacoustic discharge efficiency on the capacity for the condensers of the pulse current generator are shown in Fig. 4. The pressure pulses almost do not depend on the condenser capacity either by their amplitude or by their extension in space. The electroacoustic efficiency is mainly determined by the condenser capacity and, at $C$ = 6 μF, can reach 8% for an electrode of small radius. The pressure dependencies at different charge voltages are presented in Fig. 5, from which it can be seen that the pressure grows with an increase in the voltage. On the whole, the character of the changes in the obtained calculated data corresponds to the known experimental dependencies [5, 14].

## CONCLUSIONS

The analytical dependencies that have been obtained in the work for the main technological parameters of the PCD with CPF—the maximal pressure on the boundary of the CPF and its radius, the maximal pressure on the compression wave front at the distance from the CPF, and electroacoustic discharge efficiency—indicate good agreement with the known experimental results. The presented engineering method of calculating the PCD characterictics using the external adjustable parameters of the pulse generator included in a technological electric-discharge installation permits one to estimate the probable results of the PCD effect on a treated object.

## REFERENCES

1. Ostroumov, G.A., *Vzaimodeistvie elektricheskikh i gidrodinamicheskikh polei* (Interaction of Electric and Hydrodynamic Fields), Moscow: Nauka, 1970.
2. Naugol'nykh, K.A. and Roi, N.A., *Electricheskie razryady v vode* (Electric Discharges in Water), Moscow: Nauka, 1971.
3. Boguslavskii, L.Z., Krivitskii, E.V., Petrichenko, V.N., Electrohydrodynamic Phenomena at Pulse Corona Discharge in Strong Aqueous Electrolytes, *Electronnaya obrabotka materialov,*, 1991, no. 5, pp. 51–54.
4. Boguslavskii, L.Z., Bristetskii, E.V., Krivitskii, E.V. and Petrichenko, V.N., Investigations of Multisteamer Corona Discharge Striking in Weakly Conductive Electrolytes, *Teoriya, eksperiment, praktika electrorazryadnikh tekhnologii*, 2002, issue 4, pp. 7–15.
5. Boguslavskii, L.Z., Kucherenko, V.V. and Krivitskii, E.V., Dynamics of Pulse Corona Discharge in Aqueous Electrolytes, *Preprint of Institute of Pulse Processes and Technologies, National Academy of Sciences of Ukraine*, Nikolaev, 1993, no. 22, p. 41.
6. Petrichenko, S.V., Extensive Corona Discharge in Strong Aqueous Electrolytes, *Electronnaya obrabotka materialov*, 2005, no. 2, pp. 58–63.
7. Shamko, V.V. and Boguslavskii, L.Z., Mathematical Modeling of Corona Discharge in Strong Aqueous Electrolytes, *Teoriya, eksperiment, praktika electrorazryadnikh tekhnologii*, 2002, issue 4, pp. 34–44.
8. Boguslavskii, L.Z., Khainatskii, S.A. and Scherbak, A.N., Optical Studies of the Plasma–Liquid Transition Layer in Pulsed Corona Discharges in Strong Water Electrolytes, *Zh. tekhnicheskoi fiziki*, 2001, vol. 71, no. 2, pp. 43–47 [*Tech. Phys.* (Engl. Transl.), vol. 46, no. 2, pp. 174–178].
9. Krivitskii, E.V. and Shamko, V.V., *Perekhodnye protsessy pri vysokovol'tnom razryade v vode* (Transitional Processes at High-Voltage Discharge in Water), Kiev: Naukova dumka, 1979.

10. Akulichev, V.A., *Kavitatsiya v kriogennykh I kipyaschikh zhidkostyakh* (Cavitation in Cryogenic and Boiling Liquids), Moscow: Nauka, 1978.
11. *Tekhnika ta electrofizika visokikh napryh* (Engineering and Physics of High Voltages), Brzhezits'kii, V.O. and Mikhailov, V.M., Eds., Kharkiv: NTU KhPI-Tornado, 2005.
12. Khainatskii, S.A., Shamko, V.V. and Boguslavskii, L.Z., Determination of Pulse Corona Strike Velocity in Strong Electrolytes, *Elektronnaya obrabotka materialov*, 2005, no. 5., pp. 42–47.
13. Shamko, V.V. and Kucherenko, V.V., Theoretical Foundations of Engineering Calculations of Energy and Hydrodynamic Parameters for Underwater Spark Discharge, *Preprint of Institute of Pulse Processes and Technologies, National Academy of Sciences of Ukraine*, Nikolaev, 1991, no. 18, p. 51.
14. Kucherenko, V.V., Ischenko, Zh.N., Sidoruk, V.V. and Boguslavskii, L.Z., Determination of Hydrodynamic Characteristics in the Near-Field Zone of Spark and Corona Discharges in Liquids. Physical Model, *Elektronnaya obrabotka materialov*, 2001, no. 3, pp. 17–22.
15. Kalinin, A.B., Kalinin V.V. and Pivovarov, B.L., *Seismoakusticheskie issledovaniya na akvatoriyakh* (Seismoacoustic Investigations on Aquatories), Moscow: Nedra, 1983.
16. Shamko, V.V., Krivitskii, E.V. and Kucherenko, V.V., Approximate Similarity of Electrophysical and Kinematic Processes during Pulsed Corona Discharges in Strong Electrolytes, *Zh. tekhnicheskoi fiziki*, 1999, vol. 69, no. 5, pp. 30–34 [*Tech. Phys.* (Engl. Transl.), vol. 44, no. 5, pp. 506–510].

ISSN 1068-3755, Surface Engineering and Applied Electrochemistry, 2009, Vol. 45, No. 5, pp. 397–403. © Allerton Press, Inc., 2009.
Original Russian Text © S.A. Khainatskii, 2009, published in Elektronnaya Obrabotka Materialov, 2009, No. 5, pp. 57–64.

## ELECTRICAL PROCESSES IN ENGINEERING AND CHEMISTRY

# Investigations on Optimal Mode of Electric Explosion of Conductors in Water and Air

**S. A. Khainatskii**

*Institute of Pulse Processes and Technologies, National Academy of Sciences of Ukraine,*
*pr. Oktyabr'skii 43-A, Nikolaev, 54018 Ukraine*
*e-mail: defr@iipt.com.ua*

**Abstract**—In this work, it is established that the ratio of the stored energy to the conductor weight $W_0/m$ can be used as a similarity criterion for the electrical characteristics of conductor explosion. It is shown that the specific stored energy $W_0/m$ and the ratio of the sublimation energy of the conductor metal to the stored energy $W_s/W_0$ for the optimal modes of electric explosion of conductors in air do not depend on externally driven parameters in the same way as for an explosion in water. The conditions providing a high rate of energy release in a discharge gap during EEC in air are determined. The relation between the optimal parameters of conductor explosion in water and air is found.

**DOI:** 10.3103/S106837550905010X

## INTRODUCTION

An electric explosion of conductors (EEC) has continued to be intensively studied during the last several decades. Interest in this phenomenon is caused by rapid development of high energy density physics, investigation of the extreme states of a compound under high pressures and temperature, a series of practical applications connected with current investigations in power engineering, inertial thermonuclear fusion, space engineering, and nanotechnologies, in particular, the technology of production of nanosized powders of pure metals and their compounds [1, 2]. In general, the mechanism of decomposition of a conductor upon flow of current of different density is quite well studied. A number of models that can provide a qualitatively full image of a discharge through exploding fine metallic wires and subsequent MHD evolution of a system are developed. However, some phenomena occurring during EEC appear to be rather difficult for strict theoretical investigations. Therefore, the problem of derivation of relations describing the interconnection of the character of energy release in a conductor during an explosion with its physical properties on the basis of methods of similarity theory is topical. Among a variety of publications on this problem, special attention should be drawn to a monograph [3], including both a review of publications and the author's results devoted to the similarity of EEC in water. Also presented are the relations obtained by the author for determining the so-called optimal parameters for the conductors exploding in water which provide the maximal rate of energy release in a conductor. These relations, in our opinion, remain to this day the most appropriate and accurate. On the basis of these relations, we established [4] that, for the optimal modes of EEC, when all the energy stored in a capacitor is introduced into the conductor during the first half-period of a discharge, the ratio of the stored energy $W_0 = CU_0^2/2$ to the weight $m$ of the conductor exploding in water does not depend on its dimensions and the parameters of the discharge circuit. Since this ratio serves as a sort of "integral" of the conductor properties, it is not improbable that it can be a dimensional similarity criterion for the EEC characteristics. This is indirectly confirmed by application of the ratio $W/m$ within the classification of EEC modes, which is based on the rate of introduction of energy into a conductor [5]. It will be shown below that the ratio $W_0/m$ can in fact be used as an approximate similarity criterion for the electric characteristics of EEC in an *RLC* chain.

Moreover, it is known that the relations for the optimal length and diameter of a conductor [3] and, correspondingly, the ratio $(W_0/m)_{\text{opt}}$ obtained on their basis [4] do not contain in an explicit form the parameters of the surrounding medium. Therefore, the goal of present work is to establish similar relations for an explosion in air and to compare them with the results previously obtained for water.

## SIMILARITY OF ELECTRICAL CHARACTERISTICS OF EEC IN WATER

The similarity of the electric characteristics of EEC in water, as we have already mentioned, is described by relations (4.11), (4.15), and (4.16) from the monograph [3]. Presented in the same paper on p. 129 are dimensionless curves of the discharge current (see Fig. 43) for the cases of an explosion of copper and aluminum conductors under the similarity criteria $\Pi_2$ and $\Pi_3$ = idem. Although all the dimensional constants which characterize both the discharge circuit and the sample under

**Table 1**

| Conductor material | $d$, mm | $l$, mm | $U_0$, kV | $C$, μF | $L$, μH | $\Pi_2$ | $\Pi_3 \times 10^2$ | $U_{\text{peak}}/U_0$ | $W_0/m$, kJ/g | $(W_0/m)_{\text{opt}}$, kJ/g |
|---|---|---|---|---|---|---|---|---|---|---|
| Cu | 0.30 | 116 | 40 | 3.0 | 2.26 | 0.38 | 3.17 | 3.2 | 32.78 | 20.56 |
| Cu | 0.51 | 100 | 18 | 34.6 | 2.53 | 0.35 | 3.30 | 3.7 | 30.73 | 20.56 |
| Cu | 0.66 | 100 | 14 | 99.0 | 3.0 | 0.35 | 3.30 | 3.6 | 31.76 | 20.56 |
| Cu | 0.33 | 67 | 8 | 48.0 | 10.6 | 0.35 | 3.05 | 3.7 | 30.02 | 20.56 |
| Al | 0.41 | 68 | 8 | 47.6 | 11.8 | 0.38 | 3.14 | 3.3 | 62.84 | 44.35 |

investigation differ significantly (see Table 1), the normalized ($\bar{i} = \frac{I}{U_0}\sqrt{\frac{L}{C}}$, where $I$ is the measured current, $U_0$ is the initial voltage, and $L$ and $C$ are the circuit inductance and capacity; $\bar{t} = t/\pi\sqrt{LC}$, where $t$ is the "physical" time) curves of the discharge current virtually coincide. The overvoltage peaks in these experiments also coincide satisfactorily. We refer to these data because this experiment is rather time consuming: it is necessary to adapt each time the measuring chain to the significantly differing parameters of the discharge circuit. Table 1 presents the main electrical parameters ($U_0$, $C$, $L$) of these tests, the parameters of the exploding conductor ($d$ is diameter, $l$ is length), the values of the similarity criteria $\Pi_2$ and $\Pi_3$, and the magnitude of the relative inductive peak of the overvoltage $U_{\text{peak}}/U_0$ given in Table 11 of the monograph [3] (p. 130).

Besides the materials of Table 11 from [3], Table 1 includes the values of the ratio of the stored energy to the conductor weight $W_0/m$ for each given explosion mode, as well as the calculated values of this ratio for the optimal explosion mode of the conductors from these metals $(W_0/m)_{\text{opt}}$ [4] computed using tabular data. As can be seen from Table 1, the ratio $W_0/m$ for the copper conductor is kept practically constant for every presented mode. The discrepancies between different modes do not exceed the discrepancies for the other calculated parameters. For the second and third conductors, upon full coincidence of $\Pi_2$ and $\Pi_3$, this discrepancy is about 3%. Taking into account the experimental error, which exceeds 5%, and the approximate character of $\Pi_2$ and $\Pi_3$ criteria, it can be stated that, for all modes of explosion of the copper conductors chosen in [3], the ratio $W_0/m$ describes them with the same accuracy as the indicated similarity criteria. In this case, the simplicity and convenience of application of the ratio $W_0/m$ versus a set of similarity criteria are incomparable.

To estimate how versatile an approach based on the ratio $W_0/m$ can be, let us calculate the ratio of these values for the fourth copper and aluminum conductors having fuller coinciding current oscillograms [3]. Then we obtain 2.09. The same ratio of the values $(W_0/m)_{\text{opt}}$ calculated using tabular data for the same metals is 2.16; i.e., the discrepancy is also 3%. Thus, it is possible to define similar explosion modes for conductors from any material using a simple parameter $W_0/m$ and, let us say, the data for copper and aluminum or any other metal. An algorithm for application of this ratio is rather simple. If it is necessary to reproduce any explosion mode, for example, the explosion mode of a copper conductor for a nickel one, we take the ratio $W_0/m$ from the experiment with copper, divide the tabular value of $(W_0/m)_{\text{opt}}$ for nickel by the value for copper, and multiply by the known value of the ratio $W_0/m$ for copper. Hence, we obtain the required ratio of $W_0/m$ for nickel. Proceeding from this ratio, it is not difficult to choose the explosion parameters for an available nickel conductor with similar character of the current and voltage curves.

## OPTIMAL PARAMETERS FOR CONDUCTORS UPON EXPLOSION IN AIR

A classical work devoted to application of similarity theory for the calculation of the characteristics of EEC in air is [6]. Two similarity criteria were obtained for the electrical characteristics of the initial step of conductor explosion in air. The first one, namely, $\Pi_1$, characterizing the approximate similarity of the initial step of explosion, i.e., the first current impulse, fully coincides with the criterion of conductor explosion in water given in a later work [7]. The second one, namely, $\Pi_2$, providing the explosion stage, includes some constant of the exploding conductor material $h^*$ not determined by the author that has the dimension of the specific action. Comparison of this $\Pi_2$ value with the second criterion given in [7] allows one to suggest that this constant is most likely to be determined within a constant factor as $h^* = \rho\sigma_0(\lambda + \gamma)$, where $\rho$is the density, $\sigma$ is the specific electrical conductivity, and $\lambda$ and $\gamma$ are the specific heat of melting and evaporation of a conductor material. This can follow from the solution of energy-balance equation upon conductor explosion presented in [8] in the form

$$\frac{de}{g(e)} = \frac{R_0 i^2}{m} dt, \tag{1}$$

where $e$, $R_0$, and $m$ are the specific energy, resistance of the conductor in a cold state and its weight, and $i$ is the current at the moment of time $t$. Integration of (1) before the moment of explosion gives an “action integral” on the right side, and the Stieltjes integral that depends only on the conductor material properties and on application of the normalization accepted in [3] will give the corresponding expression on the left side. Then, the second criterion for the explosion of the conductor in air will have the form

$$\Pi_2 = \frac{CU_0^2}{zd^4\rho\sigma_0(\lambda+\gamma)}, \tag{2}$$

where $z = \sqrt{L/C}$ is the wave resistance of a chain, and $d$ is the diameter of the exploding conductor.

The third criterion “responsible” for similarity of the electric characteristics of the conductor explosion during the arc stage was suggested for the first time, and to the best of our knowledge, only in [7]:

$$\Pi_3 = \frac{Al^2}{U_0^2\pi\sqrt{LC}}. \tag{3}$$

Here, $A$ is the spark constant and $l$ is the length of the conductor. For metal conductors regardless of the material, $A = 10^4$ V$^2$ s/m$^2$. An accurate and experimentally confirmed form of the criterion $\Pi_3$ for air can somewhat differ from (3) but only by a constant factor, since the methods of similarity theory were used to obtain it and the initial equations describing the explosion process in both cases are almost identical. The procedure for determining the optimal parameters, as will be shown below, is based on the analysis and processing of the array of experimental data, so that this circumstance cannot influence the result.

Based on the criteria $\Pi_2$ and $\Pi_3$, we can obtain the relations for determining the optimal parameters of the conductor exploding in air. Search for the optimal parameters of the conductor is based on the determination of the maximal rate of release of energy into the conductor $\overline{N}_{\max} = f(\Pi_1,\Pi_2,\Pi_3)$; finding the optimal conditions for EEC is the solution of the problem of the extremum for this function. Here $\overline{N}_{\max}$ is the dimensionless rate of release of energy into the conductor determined experimentally for different $\Pi_1$, $\Pi_2$, and $\Pi_3$. Taking the values of the similarity criteria for conductor explosion in air, the corresponding optimal conditions for explosion as some constants $\Pi_1 = a_1$, $\Pi_2 = a_2$, and $\Pi_3 = a_3$, the normalized value of the maximal rate of energy introduction can be presented as

$$\overline{N}_{\max} = f(\Pi_1,\Pi_2,\Pi_3)\big|_{\Pi_1 = a_1;\Pi_2 = a_2;\Pi_3 = a_3} = a. \tag{4}$$

Taking into account the normalization coefficients for time ($2/T_0$), current ($1/I_0$), voltage ($1/U_0$), and power ($1/U_0I_0$ or $T_0/4\pi W_0$), it is not difficult to obtain (in a dimensional form) for the maximal rate of energy introduction $N_{\max} = a\frac{4\pi W_0}{T_0}$. The geometrical sizes of the conductor corresponding to the optimal conditions of an explosion can be found from the expressions for $\Pi_2$ and $\Pi_3$

$$\begin{cases} d_{\text{opt}}\sqrt{\dfrac{CU_0^2}{a_2 z\sigma\rho(\lambda+m)}}; \\ l_{\text{opt}} = \sqrt{\dfrac{a_3U_0^2\pi\sqrt{LC}}{A}}. \end{cases} \tag{5}$$

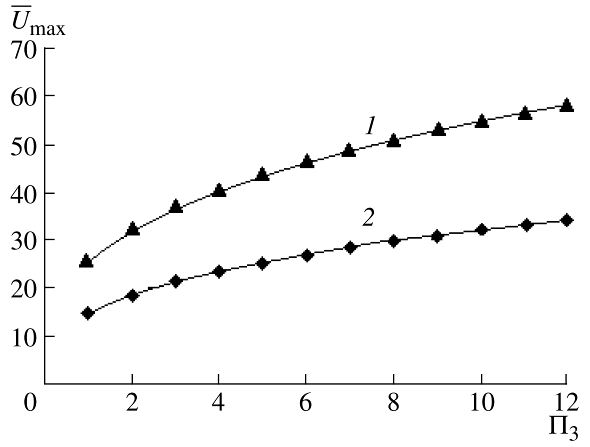

Experimental dependence $\overline{U}_{\max} = f(\Pi_3)$ for parameter values $\Pi_2$ = 0.5 (upper curve) and 0.1.

To determine the maximal rate of release of energy into the conductor and to obtain $d_{\text{opt}}$ and $l_{\text{opt}}$ by (5), we used the array of experimental data of EE of the copper and aluminum conductors produced earlier by V. Skorykh and V. Sholom at the Institute of Pulse Processes and Technologies, National Academy of Sciences of Ukraine. In the analyzed experiments, we used predominantly a storage unit of IM-50-3 capacitors, the capacitance was varied from 3 to 99 μF, and the inductance was varied using a multiturn coil from 1 to 10 μH. On the current and voltage oscillograms recorded with OK-21 and OK-25 oscillographs, we measured the voltage at the peak and the value of current corresponding to this moment, determining in this way the value of $\overline{N}_{\max}$. We imposed the same restrictions on the choice of the modes as in [7]: only oscillograms of the modes without intervals for which the time for attainment of the first current peak did not exceed a quarter of the period of the natural oscillation frequencies of the circuit were analyzed.

The figure presents the dependence $\overline{U}_{\max} = f(\Pi_3)$ for the parametric values $\Pi_2 = 0.5$ (upper curve) and 0.1. Approximation of the dependence $\overline{U}_{\max} = f(\Pi_3)$

by an exponential function $y = cx^b$ makes it possible to obtain the value of the exponent $b = 1/3$ for all $\Pi_2$. Processing of a large array of experimental data showed that the parameter $c$ is the function of the criterion $\Pi_2$: $c = 32\Pi_2^{1/3}$. Thus, the empirical dependence of the amplitude of the voltage impulse acquires the form $\overline{U}_{\max} = 32\Pi_2^{\frac{1}{3}}\Pi_3^{\frac{1}{3}}$.

Finding the dependence of the current value corresponding to the voltage peak from the similarity criteria was carried out in two steps. At the first one, the dependenc $\bar{I}_{\max} - \bar{I}_{\text{peak}}/\bar{I}_{\max}$ was analyzed. Here $\bar{I}_{\text{peak}}$ is the current value corresponding to the voltage peak. The analysis of the experimental current oscillograms for $\bar{I}_{\text{peak}}$ using the same approximation as above mentioned gave the expression $\bar{I}_{\text{peak}} = \bar{I}_{\max} = (1 - 5\Pi_3^{3/4})$. Then, for the functional dependence of the amplitude of the first current impulse from the similarity criteria upon approximation of the experimental dependence $\bar{I}_{\max}$ from $\Pi_2$ by the function of form $y = cx^{-b}$, we obtained $\bar{I}_{\max} = 0.47\Pi_2^{-1/3}$. Taking this into account, for the dependence of the maximal power from the similarity criteria, it is not difficult to obtain

$$\overline{N}_{\max} = \overline{U}_{\max}\bar{I}_{\text{peak}} = 15\Pi_3^{1/3}(1 - 5\Pi_3^{3/4}). \tag{6}$$

Attention is directed to the fact that $\overline{N}_{\max}$ depends only on $\Pi_3$, i.e., among the geometrical parameters, only the length of the conductor influences the rate of energy introduction into the conductor. Actually, this is not the case; the obtained expressions are true only for the modes of explosion limited by the two aforementioned conditions. These conditions impose some restrictions on the diameter of the exploding conductors, therewith both on the one hand (modes without intervals) and on the other.

Building the experimental dependence of $\overline{N}_{\max}$ from $\Pi_3$ makes it possible to determine the peak of this curve and the value of the optimal $\Pi_3 = a_3 \cong 2.43 \times 10^{-2}$ corresponding to this peak. The corresponding value of the maximal rate of energy introduction is $\overline{N}_{\max} = a \cong 3$.

Selection of an optimal value of the similarity criterion $\Pi_2$ is based on the above-indicated restrictions on the discharge mode (absence of intervals and maximal current for a time less than $T/4$). Although within these limits ($\Pi_2 > 0.074$) the rate of energy introduction does not change, we suggest the recommended value $\Pi_2 = a_2 = 0.2$. From here, using the obtained values $a_2$ and $a_3$, we find the final expressions for the optimal diameter and length of the conductor upon EEC in air

$$\begin{cases} d_{\text{opt}}^a = (10)^{1/4}\left[\dfrac{W_0}{z\rho_n\sigma_{n0}(\lambda_n + \gamma_n)}\right]^{1/4} \\ l_{\text{opt}}^a = \sqrt{\dfrac{2.3\pi}{10^2 A}}U_0\sqrt[4]{LC}. \end{cases} \tag{7}$$

Here, the upper indices $a$ denote the belonging of the parameters to an explosion in air. The corresponding parameters for an explosion in water can be denoted by an index $l$. The value $10^2 \times A = 10^6 \times \text{V}^2\ \text{s/m}^2$ in the denominator of the expression for $l_{\text{opt}}^a$ (the subduplicate expression) in [3] is replaced by its numerical value; therefore, the dimension of the optimal length of the conductor is false.

## COMPARISON OF OPTIMAL PARAMETERS OF CONDUCTOR UPON EXPLOSION IN WATER AND IN AIR

Comparing the established relations with the optimal parameters for conductor explosion in water presented in [3], we find that

$$\begin{aligned} d_{\text{opt}}^a &= d_{\text{opt}}^l\sqrt[4]{10}/2, \\ l_{\text{opt}}^a &= l_{\text{opt}}^l\sqrt{2.3\pi}/2, \end{aligned} \tag{8}$$

i.e., the optimal diameter for conductor explosion in air is approximately 12% lower ($d_{\text{opt}}^a \approx d_{\text{opt}}^l \times 0.889$ or $d_{\text{opt}}^l \approx d_{\text{opt}}^a \times 1.125$), and the optimal length is 25% greater ($l_{\text{opt}}^a \approx l_{\text{opt}}^l \times 1.344$ or $l_{\text{opt}}^l \approx l_{\text{opt}}^a \times 0.744$) than those in water.

Taking into account that the established optimal parameters $d_{\text{opt}}^a$ and $l_{\text{opt}}^a$ for EEC in air differ by constant factors from similar parameters for water obtained in [3], we can suppose that the ratio $W_0/m$ can serve as an approximate criterion also for an explosion in air.

The obtained relations (7) for determining the conditions providing the maximal rate of energy release in a discharge gap during EEC in air make it possible to establish the character of the dependence of the ratio of the stored energy $W_0$ to the conductor weight $m$ for an optimal explosion mode. For water, we developed [4] $(W_0/m)_{\text{opt}}^l = \sqrt{10^2 A}\left[\dfrac{\sigma_0(\lambda + r)}{8\pi^2\rho}\right]^{1/2}$ J/kg, $(W_0/m)_{\text{opt}}^l = k_1\left[\dfrac{\sigma_0(\lambda + r)}{8\pi^2\rho}\right]^{1/2}$ J/kg, where $k_1 = 1\ \text{V s}^{1/2}/\text{m}$. Now,

**Table 2**

| Metal | Ag | Al | Au | Cr | Cu | Fe | Mo | Ni | Sn | Pb | Ta | Ti | W | Zn |
|---|---|---|---|---|---|---|---|---|---|---|---|---|---|---|
| $(W_0/m)_{\text{opt}}$, kJ/g | 13.7 | 44.4 | 7.1 | 8.1 | 20.1 | 9.8 | 12.4 | 12 | 5.8 | 2.2 | 5.2 | 6.9 | 7.4 | 7.6 |

**Table 3**

| Metal | Ag | Al | Au | Cr | Cu | Fe | Mo | Ni | Sn | Pb | Ta | Ti | W | Zn |
|---|---|---|---|---|---|---|---|---|---|---|---|---|---|---|
| $(W_0/W_s)_{\text{opt}}$ | 4.3 | 3.1 | 3.3 | 0.94 | 3.2 | 1.3 | 1.5 | 1.4 | 1.8 | 1.9 | 0.95 | 0.6 | 1.3 | 3.2 |

using (7), it is not difficult to obtain a similar expression for air:

$$(W_0/m)^a_{\text{opt}} \approx \sqrt{10^2 A}\sqrt{\frac{2.7826}{\pi}}\left[\frac{\sigma_0(\lambda + r)}{8\pi^2\rho}\right]^{1/2} \text{J/kg},$$
$$\text{or } (W_0/m)^a_{\text{opt}} \approx k_2\left[\frac{\sigma_0(\lambda + r)}{8\pi^2\rho}\right]^{1/2} \text{J/g}, \tag{9}$$

where $k_2 = k_1\sqrt{\frac{2.7826}{\pi}}$. As can be seen, the values of the ratio of the stored energy to the conductor weight for water or air for an optimal mode of an explosion differ insignificantly; for air, this value is approximately 0.94 times lower. As well as for water, this ratio does not depend on the parameters of the discharge circuit and the conductor dimensions. Table 2 presents the values of $(W_0/m)_{\text{opt}}$ for some metals upon conductor explosion in water (the choice of metals was not of purposeful character, except for some conductors, such as Al, Cu, Ni or W often used for explosion). The reference data on mechanical, thermodynamic, and electrical properties of the metals were taken from [9].

The values of $(W_0/m)_{\text{opt}}$ for an explosion in air can be easily obtained using (9).

On the basis of the data from Table 2, it is difficult to predict the character of an explosion of the conductors from the presented materials in a concerted mode, although, as will be shown below, there exist differences, and rather significant ones. Moreover, there is no direct correlation between the affiliation of the metal to one group or another according to the classification [10] and the values of $(W_0/m)_{\text{opt}}$. This parameter has an abnormally high value for aluminum, and high value for copper and silver. Abnormally low values are typical of lead, tin, and tantalum; low values are typical of tungsten, titanium, gold, and zinc. Intermediate values are characteristic of nickel and iron. In general, the amount of energy per unit mass of conductor that is necessary to realize the "single" modes of explosion both in water and in air is not the same for different metals and depends only on their properties and does not depend on externally driven parameters.

## CONDITIONS FOR REALIZATION OF A "SINGLE" EXPLOSION AND MECHANISM OF CONDUCTOR DECOMPOSITION

Let us consider now the ratio of the stored energy to the energy necessary for evaporation of the entire substance of the conductor $W_s$ upon explosion of the conductor in air in an optimal mode. Using the same simplifications as in [4], we obtain

$$\left.\frac{W_0}{W_s}\right|^a_{\text{opt}} = 10\sqrt{\frac{2.78A\sigma_0}{8\pi^3\rho}}\left[\frac{(\lambda + r)^{1/2}}{c_p(T_b - T_0) + (\lambda + r)}\right],$$
$$\text{or } \left.\frac{W_0}{W_s}\right|^a_{\text{opt}} = k_2\left.\frac{W_0}{W_s}\right|^l_{\text{opt}}. \tag{10}$$

Here $c_p$ is the thermal capacity of the metal conductor, $T_b$ is the boiling point, and $T_0$ is the room temperature. Thus, the relation between $(W_0/W_s)_{\text{opt}}$ for water and air is the same as for $(W_0/m)_{\text{opt}}$, their values differ by approximately 0.94 times. Consequently, for the optimal modes of explosion in air, the ratio of the stored energy to the conductor sublimation energy is also a constant of the conductor material and does not depend either on its geometrical dimensions or on the parameters of the discharge circuit. Table 3 presents the values of $(W_0/W_s)_{\text{opt}}$ for a series of metals upon EEC in an optimal mode in air.

The data given in Table 3 indicate that, according to this value, metals can be divided into at least two groups. High values of $(W_0/W_s)$, i.e., two or higher, are typical just of the metals of the first group of this classification. For them, the energy required for complete evaporation of the conductor is several times lower than the stored energy; therefore, it should be expected that destruction of these conductors upon the concerted mode of explosion will proceed owing to "thermal" processes, namely, equilibrium evaporation or spinodal decomposition depending on the value of this constant. For the second group, other processes should be more typical, and evaporation will be of local character. Particular attention should be drawn among this series to the nickel conductor, the decomposition character of which was assumed to be similar to that of the copper one [7], and to the conductors for which this parameter is less than unity. As for the peculiarities of thermal

**Table 4**

| Metal | Ag | Al | Au | Cr | Cu | Mo | Ni | Fe | Pb | Sn | Ta | Ti | W |
|---|---|---|---|---|---|---|---|---|---|---|---|---|---|
| $j_{\mathrm{opt}}$, $10^{12}$ A/m$^2$ | 13.2 | 7.8 | 9.4 | 1.1 | 12.5 | 3.5 | 3.1 | 2.2 | 1 | 1.6 | 1.7 | 0.38 | 3.8 |
| $j_{\mathrm{cr}}$, $10^{11}$ A/m$^2$ | 2.2 | 3 | 1.8 | 2.7 | 3.5 | 4.9 | 3.4 | 3.2 | 0.6 | 0.3 | 2.5 | 1.5 | 5.5 |

decomposition of conductors in a concerted mode, the metals for which $(W_0/W_{\mathrm{s}})_{\mathrm{opt}} \geq 2.5$ will undoubtedly decompose with explosion accompanied by intense peaks of overvoltage ($U_{\mathrm{m}} \geq 1.5U_0$) and the stored energy to the moment of explosion $W_{\mathrm{ex}} \approx 2W_s$. The conductors with $(W_0/W_{\mathrm{s}})_{\mathrm{opt}} \leq 1$ are likely to decompose in the mode of a fuse [11]. The other metals can hold an intermediate position. In any case, the EEC process in an optimal mode has a self-consistent character at which the amount of energy released to the moment of explosion is strictly determined by the properties of the conductor material. Realization of such a “single” mode of EEC, when by the moment of explosion the amount of the released energy is equal to the sublimation energy, is possible not for all conductors but only for those for which the ratio $(W_0/W_{\mathrm{s}})_{\mathrm{opt}}$ is somewhat greater than unity.

Let us consider one more aspect of possible influence of the surrounding medium on the character of conductor decomposition. In [4], we showed that, for most metals, the initial current density upon conductor explosion in an optimal mode at the circuit inductance $L = 3.32$ μH, circuit capacitance $C = 3$ μF, and voltage $U_0 = 30$kV exceeds the critical value [12] that defines the character of their decomposition by an order of magnitude or more. We recall that, according to [12], if by the moment of explosion the current density is less than some “critical” value, then decomposition of the conductor proceeds owing to formation of MHD fluctuations, and if the current density is greater than this critical value, then the thermal processes prevail. Table 4 presents the initial (see [4]) and critical current densities for optimal modes of explosion of different conductors upon explosion in air.

As can be seen from Table 4, under the chosen circuit parameters for almost all presented metals, the initial current density upon explosion of the conductor in an optimal mode exceeds by an order of magnitude or more the critical value that determines the character of their decomposition. The only exception is the titanium conductor, for which these values are comparable. It should be taken into account that the ratio $j_{\mathrm{opt}}/j_{\mathrm{cr}}$ depends in an explicit form on the capacitance of the capacitor bank and in implicit form on the circuit inductance and initial voltage. The increase in any parameter or all of them for each metal may completely change the situation from $J_{\mathrm{opt}}/J_{\mathrm{cr}} \gg 1$ to $j_{\mathrm{opt}}/j_{\mathrm{cr}} < 1$, i.e., changing the explosion mechanism. The analysis of the experimental materials [13] shows that, under certain conditions (circuit parameters), the explosion, for example, of the nickel conductor in an optimal mode in air occurs at the moment when the energy released in it is less than the value necessary for its complete evaporation, which is not possible upon explosion in water. This indicates that expressions (7) and (9) are true for an explosion in air for a narrower range of the circuit parameters than the corresponding expressions for water.

## CONCLUSIONS

Hence, we have established that, in a certain range of values of the conductor explosion parameters, the ratio of the stored energy to the conductor weight $W_0/m$ can serve as a sufficient similarity criterion of the electrical characteristics. This range is located in some vicinity of the optimal parameters of EEC. The limits of the range where this statement is valid should be defined more exactly either using the same approach based on the similarity of the electrical characteristics of EEC or invoking some physical laws of explosion.

In this paper, it has been shown that two important energy parameters of explosion, namely, the specific stored energy $W_0/m$ and the ratio of the sublimation energy of the conductor metal to the stored energy $W_s/W_0$ for the optimal modes of EEC in air, also do not depend on externally driven parameters in the same way as for explosion in water. The conditions providing the maximal rate of energy release in a discharge gap upon EEC in air are determined. The obtained dependences of the optimal parameters of conductors are close in their form to those which were developed for EEC in water [3] and differ from them only by a constant factor. This also results from the fact that, in both cases, the same approach based on the similarity theory methods was used. The consequence of the obtained relations is that decomposition of metal conductors upon EEC in an optimal mode in air, as well as in water, proceeds mostly by means of thermal processes.

## REFERENCES

1. Sedoi, V.S., Ivanov, Yu.F., Particles and Crystallites under Electrical Explosion of Wires, *Nanotechnology*, 2008, no. 19, 145710 (6pp).
2. Kuskova, N.I., Baklar’, V.Yu., Gordienko, V.I., and Khainatskii, S.A., O poluchenii ul’tradispersnykh poroshkov metallov pri elektricheskom vzryve provodnikov v zhidkosti. Chast’ I. Osobennosti vzryva provodnikov v zhidkosti (On Production of Fine-Dispersed Metal Powders Upon Electric Explosion of Conductors in a Liquid. Part I. The Peculiarities of Explosion of Conductors in a Liquid), *Elektr. obrabotka materialov*, 2008, no. 1, pp. 44–50.

3. Krivitskii, E.V., *Dinamika electrovzryva v zhidkosti* (The dynamics of Electric Explosion in a Liqiud), Kiev: Naukova dumka, 1986, 206 p.
4. Khainatskii, S.A., Usloviya realizatsii optimal'nogo rezhima elektricheskogo vzryva provodnikov v vode (The Conditions for Realization of an Optimal Mode of Electric Explosion of Conductors in Water), *Pis'ma v Zh. Tekh. Fiz.*, 2009, vol. 35, issue 7, pp. 15–20 [*Tech. Phys. Lett.* (Engl. Transl.)].
5. *Exploding Wires*, Chace, W.G., Moor, H.K., Ed., N.Y.: Plenum Press, vol. 1, 1959; vol. 2, 1964; vol. 3, 1965; vol. 4, 1968.
6. Azarkevich, E.I., Primenenie teorii podobiya k raschetu nekotorykh kharakteristik elektricheskogo vzryva provodnikov (Application of Similarity Theory to Calculation of Some Characteristics of Electric Explosion of Conductors), *Zh. Tekh. Fiz.*, 1973, vol. 43, issue 1, pp. 141–145.
7. Krivitskii, E.V., Sholo, V.K., O priblizhennom podobii elektricheskikh kharakteristik podvodnogo vzryva provodnikov (On Approximate Similarity of the Electric Characteristics of Underwater Explosion of Conductors), *Zh. Tekh. Fiz.*, 1974, vol. 44, issue 6, pp. 1271–1276.
8. Benett, F.D., First Pulse in Exploding Wires, *Rev. Sci. Instrum.*, 1967, vol. 38, no. 2, pp. 293–294.
9. *Tables of Physical Parameters*, handbook, Kikoin, I.K., Ed., Moscow: Atomizdat, 1976, 1006p.
10. Webb, F., Hilton, G., Levin, P., Tollestrop, E., Electric and Optical Characteristics of Rapid Explosion of Wires, in *Elektricheskii vzryv provodnikov* (Electric Explosion of Conductors), Moscow: Mir, 1965, pp. 47–95.
11. Burtsev, V.A., Kalinin, N.V., Luchinskii, A.V., *Eleck-tricheskii vzryv provodnikov i ego primenenie v elektrofizicheskikh ustanovkakh* (Electric Explosion of Conductors and Its Application in Electrophysical Equipment), Moscow: Energoatomizdat, 1990, 288 p.
12. Kolgatin, S.N., Lev, M.L., Peregud, B.P. et al., Razrushenie mednykh provodnikov pri protekanii po nim toka plotnost'yu, bol'shei $10^7$ A/sm$^2$ (Decomposition of Copper Conductors upon Flow of the Current with Density Higher than $10^7$ A/cm$^2$), *Zh. Tekh. Fiz.*, 1989, vol. 59, issue 9, pp. 123–133.
13. Lebedev, S.V., Savatimskii, A.I., Metally v processe bystrogo nagrevaniya elektricheskim tokom bol'shoi plotnosti (Metals in Process of Rapid Heating by Electric Current with High Density), *Usp. Fiz.Nauk*, 1984, vol. 144, issue 2, pp. 215–250.

*ISSN 1068-3755, Surface Engineering and Applied Electrochemistry, 2009, Vol. 45, No. 5, pp. 404–410. © Allerton Press, Inc., 2009.*
*Original Russian Text © T.Ya. Datsko, V.I. Zelentsov, 2009, published in Elektronnaya Obrabotka Materialov, 2009, No. 5, pp. 65–73.*

## ELECTRICAL PROCESSES IN ENGINEERING AND CHEMISTRY

# Dependence of the Surface Charge and the Fluorine Adsorption by γ-Aluminum Oxide on the Solution Temperature

**T. Ya. Datsko and V. I. Zelentsov**

*Institute of Applied Physics, Academy of Sciences of Moldova, ul. Academiei 5, Chisinau, MD-2028 Republic of Moldova*
*e-mail: tatianadatsko@phys.asm.md*

Received May 22, 2009

**Abstract**—The dependence of the surface charge of the γ-aluminum oxide and the fluorine adsorption on the solution temperature (20, 30, and 40°C), the pH (3.5–10), and the equilibrium concentration of fluorine in the solution (from $1.0 \times 10^{-3}$ to $1.5 \times 10^{-1}$ M/l) is studied by the method of potentiometric titration and adsorption variations with the view to elucidate the nature of the processes that take place upon the removal of fluorine with the use of ECDM sludge of an aluminum alloy that was calcined at a temperature of 800°C. The adsorption isotherms were processed using the Freundlich, Langmuir, and BET equations. The best coincidence with the experimental data is obtained with the use of the Langmuir equation. It is shown that both the solution temperature increase and the amount of fluorine adsorbed by the sample surface shift the $pH_{PZC}$ to a more acid range. The fluoride adsorption occurs due to the exchange of the $OH^-$-groups of the hydrated oxide surface for fluorine ions due to the interaction of the charged $AlOH_2^+$ centers of the surface with $F^-$ ions and due to the formation of hydrogen bonds of $F^-$ and uncharged AlOH centers.

**DOI:** 10.3103/S1068375509050111

## INTRODUCTION

Adsorption from solutions is applied with increasing intensity in recent years for the removal of fluorine from potable and waste water [1–5]. The attention of scientists is focused on searching for low cost materials that can be efficient sorbents of fluorine [6–8]. The authors of [9, 10] have studied the sludge of the electrochemical dimensional machining (ECDM) of an aluminum alloy.

The value of the fluorine adsorption is affected most of all by such parameters as the solution pH, the initial content of fluorine, and the solution temperature. The study of the temperature dependence of the adsorption properties of oxides is of particular significance under the regeneration of sorbents, because an increase in the temperature leads to an enhancement of the adsorbent solubility and to a change in the stability of the surface complexes [11–13].

Many researchers have reported the conditions and mechanism of fluorine adsorption by aluminum oxides; for example, the optimum experimental pH of fluorine removal ranges within 5 to 7 [3, 11, 14]; its adsorption occurs due to the ion exchange on the active surface centers of the aluminum oxide [12–15]. However, the mechanism of fluorine adsorption from aqueous solutions by porous aluminum oxides has not been completely elucidated.

The influence of the solution temperature on the fluorine adsorption by aluminum oxides is studied in [1, 14, 16]; it is shown there that, as it grows, the fluorine adsorption decreases; it also influences the electric surface properties of the sorbent and the composition of the surface complexes [12, 16].

The adsorption from the solution at the solid surface/electrolyte solution interface also depends on the electric boundary characteristics of the surface. These characteristics can be estimated by studying the variation of the density of the surface charge with the varying pH and temperature. Such an important characteristic of the oxide/aqueous electrolyte solution interface surface, which represents its electric nature, as the point of zero charge (PZC) can be determined by means of potentiometric titration at different ionic strengths (and, accordingly, at different thicknesses of the double electric layer). In the case of oxides, the PZC is given by such conditions in the solution under which the surface charge induced by the adsorption of $H^+$ or $OH^-$ ions is 0 ($\sigma_0 = 0$). The point at which the surface charge ceases to depend on the ionic strength is the point of intersection of three curves of the potentiometric titration obtained at different ionic forces; the pH corresponding to this point is the $pH_{PZC}$ [17].

In this work, by the application of potentiometric titration, we studied the influence of the solution temperature, the pH, and the amount of fluorine adsorbed by the surface on the surface charge at the $\gamma$-$Al_2O_3$/aqueous fluoride solution interface with the view to elucidate the mechanism of the adsorption.

## EXPERIMENTAL[1]

For the experiments on the adsorption and potentiometric titration, we used a sample of the product of the ECDM of an aluminum alloy that was calcined at 800°C (hereinafter, A800). The A800 sample, according to the XRD phase analysis data, is $\gamma$-$Al_2O_3$ (up to 95%) with characteristic lines with interplanar distances of 2.39, 1.98, 1.95, 1.395, and 1.14 Å. The sample composition is 0.022 mol$H_2O$/mol$Al_2O_3$. The specific surface area according to the BET (adsorption of $N_2$, "Autosorb1") is 145.6 $m^2/g$, the sorption volume of the pores is 0.221 $cm^3/g$, and the effective radius of the pores is 3.0 nm

The adsorption experiments were carried out using an acetate buffer; the initial concentration of the fluorine was varied from $1.0 \times 10^{-3}$ to $1.5 \times 10^{-1}$ M; and, in the course of measuring the isotherms, the solution temperature was 20, 30, and 40°C.

The potentiometric titration was performed by the technique described in [17]. The surface charge density was calculated by the formula

$$\sigma_0 = \frac{FC\Delta V}{mS_{\rm sp}}, \qquad (1)$$

where $\sigma_0$ is the surface charge density, $\mu K/cm^2$; $F$ = 96500 K/g-equiv; $C$ is the concentration of HCL or KOH, g-equiv/$cm^3$; $\Delta V$ is the volume of the admixed HCl or KOH, $cm^3$; $m$ is the sorbent weight, g; and $S_{\rm sp}$ is the specific surface area, $m^2/g$.

## RESULTS AND DISCUSSION

On the hydrated surface of the aluminum oxide, the hydroxyl ions are coordinated to the aluminum cations in different ways, forming active functional groups. In general, it is possible to distinguish more than one type of the surface $OH^-$-groups; these different groups exhibit properties that make them different from the $OH^-$-groups in the bulk of the mineral structure. The number and type of each surface group depend on the following: which crystal planes are predominantly bare, and how the aluminum ions are distributed over the surface [18]. For example, a gibbsite crystal cleaves mostly along the 001 plane; this occurs only due to the breaking of weak hydrogen bonds, which hold the layers in the structure. The surface hydroxyl ions in this plane look like a close-packed pseudohexagonal matrix with each OH coordinated with a pair of overlapping aluminum ions. This basal plane constitutes the primary surface of gibbsite. Aluminum ions with potentially unsaturated positive charges can be situated at the edges (the 100 and 110 planes). On these centers, OH ions are coordinated with only one aluminum ion; these groups are more reactive. For $\gamma$-$Al_2O_3$, mainly the 001 plane of a defective spinel matrix is found. The surface of the $\gamma$-$Al_2O_3$ is hydrated when water becomes chemically bound with oxygen ions, which have broken bonds along the cleavage plane. The hydrated surface confines 12.5 water molecules per $nm^2$ of surface after 100-h evacuation at a temperature of 25°C. Although most of the water is chemisorbed and is contained in the form of OH-groups, the IR studies proved that a certain amount of it, being strongly adsorbed at 25°C, remains in the form of molecular water. In an ideal model of the hydrated surface of aluminum oxide, one can differentiate two types of surface hydroxyl groups: those coordinated with one aluminum ion and those coordinated with two aluminum ions. The hydroxyl groups coordinated with one aluminum ion are more basic and more readily participate in ligand exchange reactions [19]. Since the OH-groups on the edge planes of gibbsite can only be one-coordinated, it is possible to expect a certain correlation of the surface chemistry of the $\gamma$-$Al_2O_3$ with the chemistry of the edge surfaces of the gibbsite. The two-coordinated hydroxyl groups are more acidic due to the strong polarization induced by the aluminum ions on the oxygen atom; the one-coordinated hydroxyl groups must be less acidic by their nature.

The hydrated surface of aluminum oxide exhibits an amphoteric behavior in water; that is, it is capable of adsorbing or evolving protons. This behavior is attributed, in general, to amphoteric hydroxyl groups instead of independent acid or basic surface hydroxyl groups. For a hypothetical system that consists of only pure water and the aluminum oxide surface introduced into it, the reactions of ionization of the surface hydroxyl (aluminol) groups depending on the solution pH can be presented as follows [20]

$$\mathrm{AlOH} + \mathrm{H}^+ = \mathrm{AlOH}_2^+; \qquad (2)$$

$$\mathrm{AlOH} = \mathrm{AlO}^- + \mathrm{H}^+, \qquad (3)$$

where AlOH is the aluminol group.

These reactions lead to the development of an electric charge and potential on the surface. For the validity of the electroneutrality, an equivalent number of counterions must accumulate near the $Al_2O_3$/water interface. In the case of electrolytes, the charge of the counterions can consist of a diffuse atmosphere of the counterions, a compact layer of bound counterions, or their combination.

The balance of the surface charge of aluminum oxide in an aqueous solution can be presented in the following form [21]:

$$\sigma_{\rm H} + \sigma_{is} + \sigma_{os} + \sigma_d = 0, \qquad (4)$$

where $\sigma_H$ is the total charge of the protons determined from the relation $\sigma_{\rm H} = F(\Gamma_{\rm H} - \Gamma_{\rm OH})$, where $\Gamma$ is the surface excess of the concentration; $\sigma_{is}$ is the inner-sphere complex charge formed by the inner-sphere complexes between the adsorbed ions (other than $H^+$ and $OH^-$) and the surface aluminol groups; $\sigma_{os}$ is the outer-sphere complex charge obtained by the formation of outer-

---

[1] Leading engineer E.E. Dvornikova took part in this work.

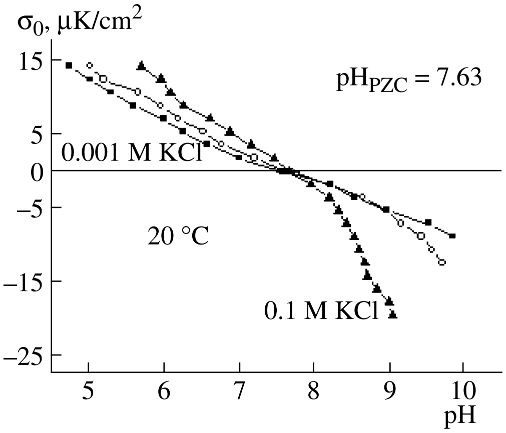

**Fig. 1.** Density of the surface charge of A800 at 20°C as a function of the pH.

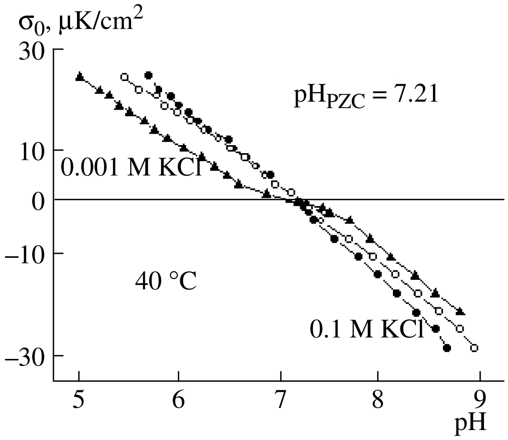

**Fig. 2.** Density of the surface charge of A800 at 40°C as a function of the pH.

sphere complexes between the adsorbed ions and surface aluminol groups or ions from the inner-sphere complexes; and $\sigma_d$ is the dissociated charge equal with a negative sign to the surface charge neutralized by the electrolyte ions in the solution, which do not form adsorbed complexes with the surface aluminol groups.

The PZC is the values of the pH attributed to the specific requirements on the surface charge. This is the solution pH, where the total charge of a particle is 0 (equation 4). In the conditions of the absence of specific adsorption, expression (4) resolves itself into

$$F(\Gamma_H - \Gamma_{OH}) = 0. \tag{5}$$

The PZC for hydroxides is the point at which the densities of the negatively charged centers on the surface are equal to the densities of the positively charged centers. This point is correlated with the solution pH at which the given hydroxide exhibits the lowest solubility. According to the data of the author of [12], who theoretically calculated the pH of the minimal solubility in the $\alpha$-$Al_2O_3$–$H_2O$ system, the lowest solubility for $\alpha$-$Al_2O_3$ is found at the pH of approximately 7.5.

The density of the surface charge of the $\gamma$-$Al_2O_3$, which was determined in an indifferent KCl electrolyte as a function of the pH and temperature of the solution, is depicted in Fig. 1, which shows the point of intersection of the three curves of the titration at three ionic strengths of the solution, which corresponds to the zero charge of the surface at pH = 7.63. The value of the $pH_{PZC}$ determined by us for the A800 ($\gamma$-$Al_2O_3$) ranges within the limits obtained by different authors by the method of potentiometric titration for pure phases of $\gamma$-$Al_2O_3$, and it is 7.0–8.3 [22].

### *The Dependence of the $pH_{PZC}$ on the Solution Temperature*

Figures 1 and 2 show the PZC dependence on the solution temperature. One can see the left shift of the $pH_{PZC}$ from 7.63 to 7.21 as the temperature increases from 20 to 40°C. A similar temperature effect of the $pH_{PZC}$ decrease with increasing solution temperature in the $Al_2O_3$–$H_2O$ system was reported by many authors [23–25]. It is assumed that an increase in the temperature contributes to the desorption of protons by the following surface reactions:

$$AlOH_2^+(s) = AlOH(s) + H^+; \tag{6}$$

$$AlOH = AlO^- + H^+. \tag{7}$$

It is known that the solubility of metal oxides increases with increasing temperature and decreasing pH; therefore, for the interpretation of the data on the $pH_{PZC}$ shift, it should be taken into account that an increase in the temperature causes an increase in the solubility of the studied sample with the formation of hydrated compounds on its surface.

If we have the temperature dependence of the $pH_{PZC}$, we can calculate the standard thermodynamic functions of the process of charging of the oxide surface in an aqueous solution by the equation given in [26], which relates the water constant, the $pH_{PZC}$, and the thermodynamic functions of the process for the oxides:

$$4.6R[1/2pK_W - pH_{PZC}] = \frac{\Delta H^*}{T} - \Delta S^*, \tag{8}$$

where $\Delta H^*$ and $\Delta S^*$ are the standard heat and the standard entropy of the transition of the potential-determining ions $H^+$ and $OH^-$ from the solution bulk to the surface at the $pH_{PZC}$; $pK_w$ is the negative logarithm of the dissociation constant of water; and $pH_{PZC}$ is the pH of the surface PZC.

The $[1/2\,pK_w - pH_{PZC}]$ diagram on $1/T$ is a straight line; from its inclination and the point of intersection with the coordinate axis, it is possible to calculate the values of $\Delta H^*$ and $\Delta S^*$. The results of this work for $\gamma$-$Al_2O_3$ are in agreement with the thermodynamic relations derived in [26]; we obtained the values of –18 kJ/mol

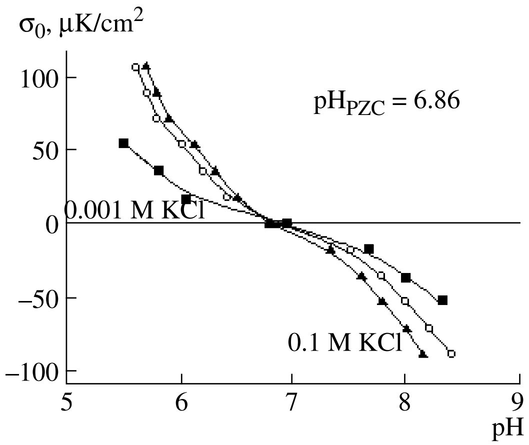

**Fig. 3.** Point of zero charge of the A800 sample with adsorbed fluorine at the solution temperature of 20°C.

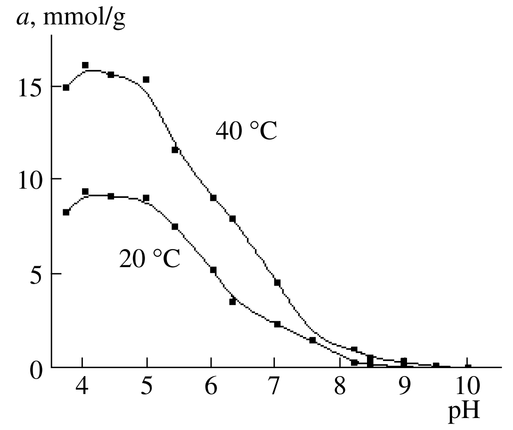

**Fig. 4.** Influence of the solution pH on the fluoride adsorption on A800 at 20 and 40°C.

and –0.042 kJ/mol for $\Delta H^*$ and $\Delta S^*$, respectively. A negative value of the enthalpy is characteristic of an exothermal process; it counts in favor of the spon taneous transition of charges to the surface and vice versa. The obtained values of $\Delta H^*$ range within the limits reported for $\alpha$-$Al_2O_3$ (–18.36 kJ/mol) [23] and for $\gamma$-$Al_2O_3$ (–50 kJ/mol) [24].

### *Dependence of the Surface Charge Density of the A800 on the Adsorbed Fluorine*

The densities of the surface charge of the sample without and with the adsorbed fluorine as functions of the solution pH determined by the potentiometric titration are shown in Figs. 1 and 3. These results are indicative of the $pH_{PZC}$ shift towards lower values under the fluorine adsorption. This behavior is characteristic of systems with specifically adsorbed ions. According to the studies of NMR spectroscopy of $^{19}F$ on aluminum oxides in a fluoride solution [27], in our conditions, the case in hand involves free fluoride ($F^-$) capable of competing with the $OH^-$-groups of the surface of the hydrated aluminum oxide for the internal coordination sphere of the aluminum ions. The fluoride ions interchange with the surface hydroxyls by the following reactions with the formation of ion pairs with the Broensted acidic site of the $AlOH_2^+$; otherwise, the reaction proceeds with the formation of a complex on the Lewis acidic site by ligand exchange [22]:

$$AlOH_2^+ + F^- = AlOH_2{}^+F^-; \qquad (9)$$

$$AlOH_2^+ + F^- = Al^+F^- + H_2O. \qquad (10)$$

### *Dependence of the Fluorine Adsorption by the A800 Sample on the Temperature and pH*

The influence of the pH on the fluorine adsorption on the aluminum oxide at 20 and 40°C is shown in Fig. 4. The values of the fluoride adsorption were calculated by the difference between the fluoride amount admixed and the remainder in the solution after the added. The fluorine adsorption maximum ranges within the pH interval of 4–5, which is in agreement with numerous data [2–5, 12, 14, 16, 28, 29]. The maximum adsorption decreases sharply at pHs higher than 6, because these conditions are less favorable for exchange reactions (9) and (10) between the hydroxyl groups and the adsorbing fluoride ions; however, even at pH above 7.5, the adsorption preserves a certain value. The decrease in the adsorption at $pH > 6$ can be explained by two factors: the enhancement of the stability of the alumo-hydroxo-complexes on the surface and the increase in the electrostatic repulsion between the negatively charged surface and the $F^-$. The maximum adsorption also decreases slightly at pHs below 4, which can be attributed to the high solubility of the oxide in these conditions. A sharp increase in the solubility of $\gamma$-$Al_2O_3$ at pH below 4 was observed in the diagram [12].

The dependence of the fluoride adsorption by the A800 sample surface at pH = 5 and pH = 7.5 (the pH close to the $pH_{PZC}$) on the solution temperature is shown in Fig. 5, where one can see that, as the temperature grows, the adsorption increases. The $pH_{PZC}$ shift to a more acid range with increasing temperature (Figs. 1, 2) is accompanied by an increase in the density of the positive charge on the surface from 12.3 to 24.6 μK/cm$^2$, which leads to an increase in the electrostatic component of the free energy of the fluorine adsorption by the A800 surface and, accordingly, to an increase in the value of the adsorption.

The adsorption isotherms were analyzed with the use of Freundlich, Langmuir, and BET equations; it was revealed that the Langmuir equation gives the best correlation (Fig. 6). The Langmuir isotherm is described by the equation

$$a = a_m kC_e/(1 + kC_e), \qquad (11)$$

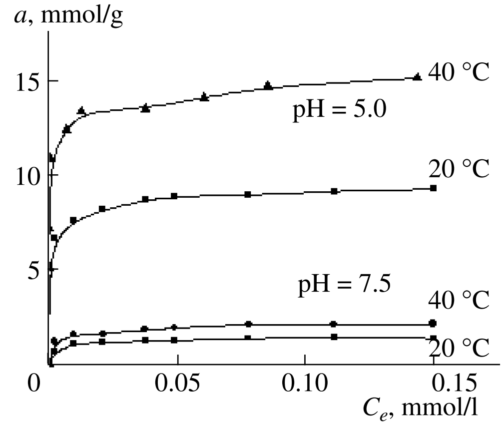

**Fig. 5.** Influence of the solution temperature on the fluoride adsorption by the A800 sample surface.

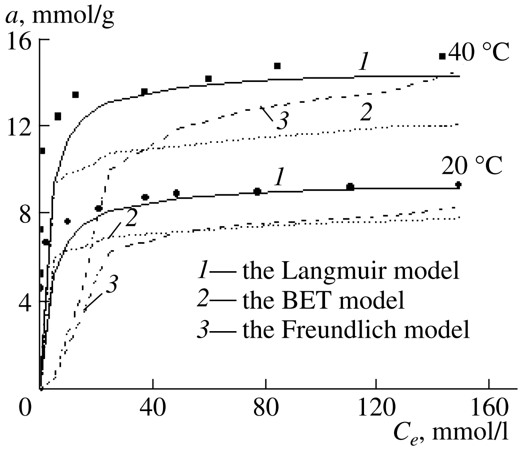

**Fig. 6.** Experimental (dots) and calculated isotherms of the fluorine adsorption by the A800 sample at pH = 5 and at two temperatures of the solution.

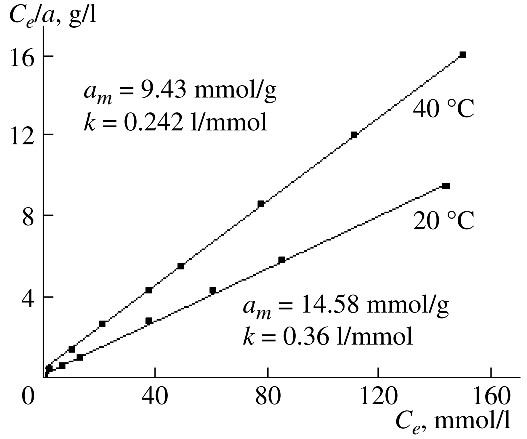

**Fig. 7.** Isotherms of the fluorine adsorption by the A800 sample at pH of 5 and 7.5 in the Langmuir equation coordinates.

where $a$ is the fluorine adsorption (mmol/g) on the A800 at the equilibrium concentration of fluorine $C_e$ (mmol/l) in the solution, $a_m$ is the monolayer capacity (mmol/g), and $k$ is the equilibrium constant of the adsorption process (l/mmol).

In the linear form, this equation is as follows:

$$C_e/a = 1/a_m k + C_e/a_m. \quad (12)$$

The diagram plotted in the coordinates $C_e/a$ on $C_e$ is a straight line (Fig. 7); by the ordinate intercept and the slope ratio of it, we calculated the values of $a_m$ and $k$ given in the table.

The density of the surface charge of the A800 sample at pH = 5 in the 0.001 M KCl indifferent electrolyte is approximately 0.12 K/m$^2$ (Fig. 1). The density of the fluorine adsorption at pH = 5 in charge units is 6 K/m$^2$, which is significantly higher than the density of the surface charge of the oxide. Hence, the adsorption of fluorine ions is performed not only by the positively charged $AlOH_2^+$ centers according to equations (11) and (12) but also by the neutral AlOH centers due to the formation of hydrogen bonds:

$$AlOH + F^- = AlOH\cdots F^-. \quad (13)$$

At pH = 7.5, which is very close to the $pH_{PZC}$, the fluorine adsorption density is 10 μmol/m$^2$, which corresponds to 1 K/m$^2$ in charge units. In addition, the density of the surface charge is about 0.002 K/m$^2$, the electrostatic contribution to the free energy of the adsorption is very low, and the fact that the adsorption is nonzero counts in favor of the fluorine adsorption through the hydrogen bond with the surface hydroxyl groups of uncharged AlOH centers. At pH higher than the $pH_{PZC}$, the fluorine adsorption on the negative surface of the sample can also be explained by the formation of hydrogen bonds through the interaction with uncharged AlOH groups that exist in equilibrium with negative $AlO^-$ groups, as one can see from equations (2) and (3). At pH above 10, when the adsorption is almost absent, the electrostatic repulsion between the negatively charged surface and fluoride ions exceeds the interaction caused by the formation of hydrogen bonds.

The density of the surface $OH^-$ groups calculated by the loss of ignition 1100°C of a sample of the composition $Al_2O_3 \cdot 0.022$ mol $H_2O$ is 1.2 μmol/m$^2$ (0.7 $OH^-$ groups/nm$^2$), or 0.12 K/m$^2$ in charge units. If we compare this value with the adsorption density of fluorine, being 65 μmol/m$^2$ or 39 $F^-$-ion/nm$^2$, which amounts to 6 K/m$^2$ in charge units, we can see that, at pH = 5, the density of the adsorbed fluoride ions considerably exceeds the density of the surface centers. This allows us to assume the polynuclear nature of the adsorption [4].

However, it would be incorrect to use the value of the density of the surface $OH^-$ groups calculated in this way, because, under the hydration of the surface, the number of hydroxyl groups in the aqueous solution must be significantly higher. By means of the technique of potentiometric titration from the acid range [30], we

Values of the maximum sorbent capacity $a_m$, the adsorption density $a_p$, and the constant $k$ of the Langmuir adsorption isotherm for fluorine on A800

| pH | $a_m$, mmol/g | $a_p$, µmol/m$^2$ | $k$, l/mmol |
|---|---|---|---|
| 5 | 9.43 | 65 | 0.242 |
| 7.5 | 1.44 | 10 | 0.833 |

calculated the adsorption of protons on the $OH^-$ groups of the surface capable of exchanging for fluoride ions. The number of hydrogen ions adsorbed on the surface of the suspension particles (in mmol/g) was calculated on the basis of the condition of the preservation of the mass balance of the hydrogen ions at each point of the titration curve by the equation

$$n_b(\mathrm{pH}) = \frac{(c_{\mathrm{HA}}V_0 - c_{\mathrm{BON}}V) - [\mathrm{H}^+](V_0 + V)}{m}, \quad (14)$$

where $c_{\mathrm{HA}}$ is the molar concentration of the strong monoacid in the initial suspension aliquot, $V_0$ is the aliquot volume (cm$^3$), $c_{\mathrm{BOH}}$ is the molar concentration of the adsorbent added, $V$ is its volume (cm$^3$), and $m$ is the adsorbent mass in the aliquot (g).

The density of the hydroxyl groups calculated by the adsorption of protons is 35 µmol/m$^2$, which corresponds to 21 $OH^-$ groups/nm$^2$ and to 3.4 K/m$^2$ in charge units. Although these values are comparable with the respective values for fluoride ions, the OH groups are in an amount insufficient for the equivalent exchange for fluorine; therefore, the assertion of multilayer adsorption holds true.

## CONCLUSIONS

Thus, the temperature affects the surface charge at the aluminum oxide/aqueous solution of sodium fluoride interface in such a way that the $\mathrm{pH_{PZC}}$ decreases as the temperature grows. The temperature dependence of the $\mathrm{pH_{PZC}}$ allowed determining the standard enthalpy and entropy of the formation of the surface charge.

The adsorption of fluoride ions by the A800 sample surface is the maximum at pH = 4–5; above this value, it decreases sharply. Near $\mathrm{pH_{PZC}}$ of 7.5, the adsorption is insignificant. The shift of the $\mathrm{pH_{PZC}}$ of the sorbent surface to a more acid range after the fluorine adsorption shows that the fluorine is adsorbed on the A800 specifically by the mechanism of the replacement of the $OH^-$ from positively charged surface $AlOH_2^+$ centers by $F^-$ and due to the electrostatic attraction, as well as owning to the formation of hydrogen bonds with uncharged surface AlOH centers at the pH being close to and above the $\mathrm{pH_{PZC}}$. At high adsorption values, the formation of polynuclear surface complexes is possible.

## REFERENCES

1. Choi, W.-W. and Chen, K. Y. The Removal of Fluoride from Waters by Adsorption, *J. Am. Water Works Assoc.*, 1979, vol. 71, p. 562.
2. Krishna Biswas, Sanat Kumar Saha, and Uday Chand Ghosh*, Adsorption of Fluoride from Aqueous Solution by a Synthetic Iron(III)–Aluminum(III) Mixed Oxide, *Ind. Eng. Chem. Res.*, 2007, vol. 46, no. 16, p. 5346.
3. Subhashini Ghorai and Pant, K.K., Equilibrium, Kinetics and Breakthrough Studies for Adsorption of Fluoride on Activated Alumina, *Sep. Purif. Technol.*, 2005, vol. 42, no. 3, p. 265.
4. Hao, O.J. and Huang, C.P., Adsorption Characteristics of Fluoride onto Hydrous Alumina, *J. Environ. Eng.*, 1986, vol. 112, no. 6, p. 1054.
5. Nagendra Rao, C.R. and Karthikeyan, J., Adsorption of Fluoride by Gamma Alumina, *XII Int. Water Technol. Conf. IWTC12,* Alexandria, Egypt, 2008, p. 141.
6. Srimurali, M., Pragathi, A., and Karthikeyan, J., A study on Removal of Fluorides from Drinking Water by Adsorption onto Low-Cost Materials, *Environ. Pollut.*, 1998, no. 99, p. 285.
7. Fan, X., Parker, D.J., and Smith, M.D., Adsorption Kinetics of Fluoride on Low Cost Materials, *Water Res.*, 2003, no. 37, p. 4929.
8. Sujana, M.G., Thakur, R.S., and Rao, S.B., Removal of Fluoride from Aqueous Solution by Using Alum Sludge, *J. Colloid Interface Sci.*, 1998, vol. 206, pp. 94–101.
9. Zelentsov, V.I., Datsko, T.Ya., and Dvornikova, E.E., Fluorine Adsorption by Aluminum Oxyhydrates Subjected to Thermal Treatment, *Surf. Eng. Appl. Electrochem.*, 2008, vol. 44, no. 1, p. 64.
10. Zelentsov, V.I., Datsko, T.Ya., and Dvornikova, E.E., The Effect of Temperature on Equilibrium and Kinetics of Fluoride Adsorption by Thermo Treated AI Oxyhydrates, *Surf. Eng. Appl. Electrochem.*, 2008, vol. 44, no. 3, p. 39.
11. Young Ku and Hwei-Mei Chiou, The Adsorption of Fluoride Ion from Aqueous Solution by Activated Alumina, *Water, Air, Soil Pollut.*, 2002, vol. 133, no. 1, p. 349.
12. Bahena J. L. Reyes, Cabrera A. Robledo, Valdivieso A. Lopez, and Urbina R. Herrera, Fluoride Adsorption onto-$Al_2O_3$ and its Effect on the Zeta Potential at the Alumina–Aqueous Electrolyte Interface, *Sep. Sci. Techn.*, 1987, vol. 37, no. 8, p. 1973.
13. Schoeman, J.J. and Botha, G.R., Evaluation of the Activated Alumina Process for Fluoride Removal from Drinking Water and Some Factors Influencing This Performance, *Water SA*, 1985, vol. 11, no. 1, p. 25.
14. Yeun C. Wu and Anan Nitya, Water Defluoridation with Activated Alumina, *J. Environ. Eng. Div.*, 1979, vol. 105, no. 2, p. 357.
15. Berendeeva, V.L., Vakhnin, I.G., and Goronovskii, I.T., The Use of Activated Alumina A-1 for Defluorination of Water, *Khim. Tekhnol. Vody*, 1985, vol. 7, no. 3, p. 87.
16. Valdivieso A. Lopez, Bahena J.L. Reyes, Song, S., and Urbina R. Herrera, Temperature Effect on the Zeta Potential and Fluoride Adsorption at the $\alpha$-$Al_2O_3$/Aqueous Solution Interface, *J. Colloid Interface Sci.*, 2006, vol. 298, no. 1, p. 1.

17. Parks, G.A., and de Bruyn, P.L., The Zero Point of Charge of Oxides, *J. Phys. Chem.*, 1962, no. 66, p. 967.
18. Peri, J.B. and Hannan, R.B., Surface Hydroxyl Groups of $\gamma$-Alumina, *J. Phys. Chem.*, 1960 vol. 64, p.1526.
19. Peri, J.B., Infrared and Gravimetric Study of the Surface Hydration of $\gamma$-Alumina, *J. Phys. Chem.*, 1965, vol. 69, p. 211.
20. Peri, J.B., A Model for the Surface of $\gamma$-Alumina, *J. Phys. Chem.*, 1965, vol. 69, p. 220.
21. James, R.O. and Parks, G.A., Characterization of Aqueous Colloids by Their Electrical Double-Layer and Intrinsic Surface Chemical Properties, in *Surface and Colloid Science*, Matijevic, E., Ed., New York: Plenum Press, 1982, vol. 12, p. 119.
22. Goldberg, Sabine, Davis, James A., and Hem, John D., The Surface Chemistry of Aluminum Oxides and Hydroxides, in *The Environmental Chemistry of Aluminum*, Sposito, Garrison, Ed., Berkeley: Lewis Publ. Univ. California, 1996, p. 271.
23. Halter, W.E., Surface Acidity Constants of Alpha $Al_2O_3$ between 25 and 70°C, *Geochim. Cosmochim. Acta*, 1999, vol. 63, nos. 19–20, p. 3077.
24. Tewari, P.H. and McLean, A.W., Temperature Dependence of Point of Zero Charge of Alumina and Magnetite, *J. Colloid Interface Sci.*, 1972, vol. 40, no. 2, p. 267.
25. Mustafa, S., Dilara, B., Neelofer, Z., Naeem, A., and Tasleem, S., Temperature Effect on the Surface Charge Properties of $\gamma$-$Al_2O_3$, *J. Colloid Interface Sci.*, 1998, vol. 204, no. 2, p. 284.
26. Berube, Y.G. and de Bruyn, P.L., Adsorption at the Rutile–Solution Interface. I. Thermodynamic and Experimental Study, *J. Colloid Interface Sci.*, 1968, vol. 27, no 2, p. 305.
27. Duke, Catherine V. A., Miller, Jack M, Clark, James H., and Kybett, Adrian P., $^{19}F$ Mas NMR and FTIR Analysis of the Adsorption of Alkali Metal Fluorides onto Alumina, *J. Mol. Catal.*, 1990, vol. 62, no. 2, p. 233.
28. Savinelli, E.A. and Black, A.P., Defluoridation of Water with Activated Alumina, *J. Am. Water Works Assoc.*, 1958, vol. 50, no. 1, p. 33.
29. Lounici, H., Belhocine, D., Grib, H., Drouiche, M., Pauss, A., and Mameri, N., Fluoride Removal with Electro-Activated Alumina, *Desalination*, 2004, vol. 161, no. 3, p. 287.
30. Ryazanov, M.A. and Dudkin, B.N., Acid–Base Properties of $\gamma$-$Al_2O_3$ Suspension Studied by pK-Spectroscopy, *Kolloidn. Zn.*, 2003, vol. 65, no. 6, pp. 831–836 [*Colloid J.* (Engl. Transl.), vol. 65, no. 6, p. 761].

ISSN 1068-3755, Surface Engineering and Applied Electrochemistry, 2009, Vol. 45, No. 5, pp. 411–414. © Allerton Press, Inc., 2009.
Original Russian Text © A.M. Gashimov, E.D. Kurbanov, 2009, published in Elektronnaya Obrabotka Materialov, 2009, No. 5, pp. 74–79.

## ELECTRICAL PROCESSING OF BIOLOGICAL OBJECTS AND FOOD PRODUCTS

# The Influence of High-voltage Impulse Treatments on Biological Cells

**A. M. Gashimov and E. D. Kurbanov**

*Azerbaijan Institute of Physics, National Academy of Sciences of Azerbaijan,*
*avenue Dzhavid 33, Baku, Az-1143 Republic of Azerbaijan*
*e-mail: e_qurbanov@physics.ab.az@*

Received May 27, 2009

**Abstract**—Present article to influence of high pulsed electrical fields on microorganisms in water-containing medium is dedicated. A spherical model of organule by two-layer dielectric membrane is considered. The accounts and diagrams of dependence of field intensity on organule membrane from its geometrical and dielectric parameters are given. The necessity of influence by nanosecond high voltage pulses on microorganisms for their full inactivation is shown.

**DOI:** 10.3103/S1068375509050123

Strong electric pulse fields of short duration are widely used in the technological processing of materials and foodstuffs, in ozone creation, in the treatment of liquid and gas wastes, in medicine, and in agriculture. Each technology is constructed taking into account the features of the physical processes proceeding in the object that is exposed to the influence of pulse fields. In turn, the creation of high-voltage pulse installations that allow creating fields with an intensity ~100 kV/sm and more at a time of ~1ns or less is an actual problem for many electrotechnologies. From the point of view of working out liquid foodstuff processing technologies and water processing by means of high-voltage impulses for the purpose of the inactivation of the microorganisms that are in them, it is a rather actual and prospective problem. Besides, in comparison with traditional thermal pasteurization, pulse inactivation of microorganisms in the aqueous sphere is energy-conservative, while preserving the initial biological and nutritional value of the foodstuffs.

The influence of an electromagnetic field on living cells and their response to this influence is an extremely complicated process. At the present stage of the theoretical description of this process, simple models are sufficient. They are useful for making decisions and providing a mathematical description of the complicated processes in real cells and cellular systems on exposure to external electric fields.

In the present article, a biological cell model is considered and some calculations describing the influence of nanosecond impulses of high voltage on the inactivation of cells are discussed.

Single-layered and multilayered dielectric covers [1] can be cell models, inside and outside of which there is a polarizable sphere. In Fig. 1, a two-layer model of a biological cell is shown. The sphere with dielectric permeability out of the cell $\varepsilon_1$ is the processed product. The external cover of the cell corresponds to the cellular membrane [2] with dielectric permeability $\varepsilon_2$, and the dielectric area under it is the cytoplasm [3] $\varepsilon_3$. The internal cover of the cell corresponds to the nuclear membrane $\varepsilon_4$, and the area under it corresponds to the procariotic chromosome $\varepsilon_5$. The electrical breakdown of the cover serves as one of the causes of the cell's death [4]. Therefore, the electric field intensity and stress drop on

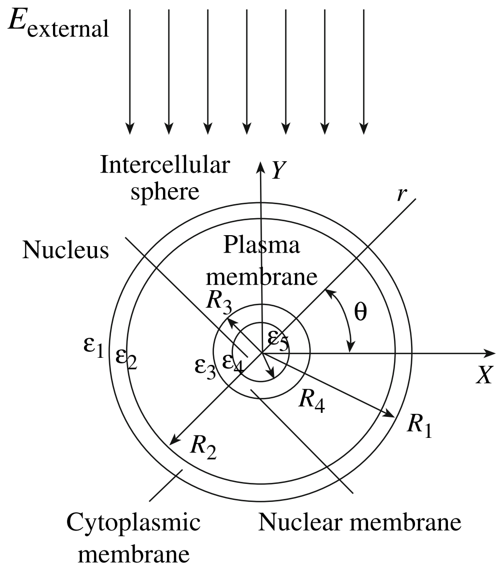

**Fig. 1.** Construction of the double-layer cover of a biological cell: $R_1$ is the external radius of the biological cell; $R_2$ is the inside radius of the outward cover; $R_3$ is the external radius of the nuclear membrane; $R_4$ is the inside radius of the nuclear membrane; $r$, $\Theta$ are the radius and angular data.

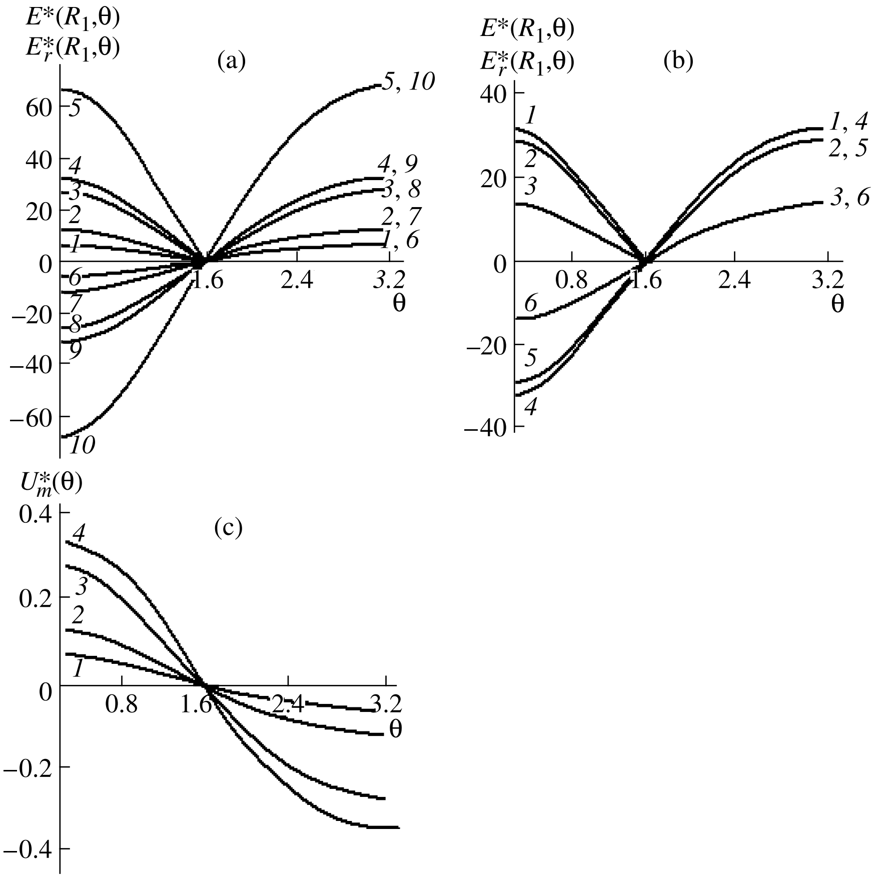

**Fig. 2** Distribution of the module $E^*$ (contours *1–5*) and the radial component $E_r^*$ (contours *6–10*) of the electric field intensity on the external surface of the cellular membrane in the model with a single-layered spherical dielectric cover. (a) 1–3 and 7–9 is $\varepsilon_3 = 60\varepsilon_0$; *4*, *6* is $81\varepsilon_0$; *5*, *10* is with a cover on the conducting sphere; *1*, *6* is $\varepsilon_2 = 10\varepsilon_0$; 2, *7* is $5\varepsilon_0$; *3–5* and *8–10* is $2\varepsilon_0$. (b). Distribution of the module $E^*$ (contours *1–3*) and the radial component $E_r^*$ (contours *4–6*) on the external surface of the cellular membrane in the model with a single-layered spherical dielectric cover at $\varepsilon_1 = \varepsilon_3 = 81\varepsilon_0$, $\varepsilon_2 = 2\varepsilon_0$, $\varepsilon_4 = 10\varepsilon_0$: *1*, *4* is $R_4 = 0.2R_1$, *2*, *5* is $R_4 = 0.5R_1$, *3–6* is $0.9R_1$. (c). Voltage drop on the membrane in the model with a single-layered spherical dielectric cover: *1–3* is $\varepsilon_3 = 60\varepsilon_0$; *4* is $81\varepsilon_0$; *1* is $\varepsilon_2 = 10\varepsilon_0$; *2* is $5\varepsilon_0$; *3–4* is $2\varepsilon_0$.

the membrane and are important characteristics of the influence of a strong electric field on a cell.

The intensity vector of the composite electric field and its components is defined by means of the known parity $\vec{E} = -\text{grad}\,\varphi^{(k)}$ underlying the basis of Laplace's equation:

$$\Delta\,\varphi^{(k)} = 0, \quad k = \overline{1, n}, \qquad (1)$$

where φ is the scalar potential of the electromagnet field, $n$ is the number of spheres with different characteristics, and $k$ is the sphere index with the given characteristics.

The solution for the homogenous dielectric blob and cylinder component is given in [5]; for a single-layered cover, it is given in [5, 6]. For an $n$-layered cover, the equation (1) appears as follows:

$$\varphi^{(k)}(r, \theta) = \left(A_k r + \frac{B_k}{r^s}\right)\cos\theta, \quad k = \overline{1, n}, \qquad (2)$$

where $A_k$ and $B_k$ are constants, $r$ and Θ are the radius and angular data, and $s$ is an indicator depending on the form of the cover.

For spherical coordinates, $s = 2$; for cylindrical coordinates, $s = 1$

The stress drop on the membrane $U_m$ is defined by the integration along the radial coordinate according to the membrane thickness. For the biological cell description, let us accept the following characteristics [3]: the relative dielectric membrane permeability is from 2 to 10; the relative dielectric cytoplasm permeability is from 60 to 81; the internal radius of the membrane $R_2 = 0.99\ R_1$. In Fig. 2, schedules of the relative module distribution and the radial component of the electric field intensity on the external surface of a spherical membrane (a, b) and the resulting stress drops (c) at various values are presented. The relative dielectric permeability of the sphere that surrounds a cell is accepted equal 81. The considered distributions are characterized by dimensionless values:

$$E_r^*(R_1, \theta) = E_r(R_1, \theta)/E_0,$$

$$E^*(R_1, \theta) = E(R_1, \theta)/E_0, \quad U_m^*(\theta) = U_m(\theta)/(E_0R_1).$$

The calculations indicated that, at the characteristics for a biological cell, the values of the relations $\varepsilon_2/\varepsilon_1$ and $\varepsilon_3/\varepsilon_2$ for the radial component of the electric field intensity in the membrane are much more than tangential. The right contour branches $E_r^*$ and $E^*$ at $\theta > \pi/2$ coincide (Fig. 2a). At $\varepsilon_2 \le 5\varepsilon_0$, the field intensity in the membrane surpasses $E_0$ by tens of times and increases with the reduction of $\varepsilon_2$ (contours 2, 4, 7, 8). The same tendency takes place at an increase of $\varepsilon_3$ (contours 4, 9).

It is known that a biological cell has a complicated nonuniform structure (in particular, procariotic cells contain chromosomes and eukaryotic cells nucleases). At the fixed value $\varepsilon_3 = 81\varepsilon_0$, we change the nuclear radius $R_3$ within $(0.2–0.9)R_1$. At $R_3 \le 0.5R_1$, the nuclear presence slightly affects the electric field in the membrane and, at $R_3 \le 0.9R_1$, leads to its easing (contours 4, 9). The dielectric permeability reduction of nuclear type leads to strengthening of the intensity of the electric field in it, especially at great values of $R_3$. In the table, the $E/E_0$ values for the nuclear model of a biological cell with a two-layer spherical dielectric cover (Fig. 2b) are presented.

Thus, the relative value of the intensity does not exceed 1.5, as well as in the case of an isolated dielectric sphere [5]. Recognizing that the cell membrane is broken through at a pressure on it of ~1 volt ([4, 7] and the data in Fig. 2), we reach the conclusion that the maximum relative values of the stress drop on the membrane, depending on the characteristics of the cell model, are in the limits of 0.1–0.3. The external electric field intensity $E_0$ = 67–200 kv/sm corresponds to these values and the specified pressure of the membrane breakdown at $R_1 = 0.5 \times 10^{-6}$.

Considering the results of the analytical calculations for the elementary cell models, let us estimate the real time of the presence of the electric pulse field in a real cell (in the cytoplasm and organelles). The qualitative situation of the influence of a strong electric field is presented in Fig. 3 (a), and distribution schemes of the power lines of the field in a microbic cell are presented in Fig. 3 (b, c). At short fronts (high frequencies), the field gets into the cell.

The boundary conditions for $t = t_1$, taking into account the essential prevalence of the currents of the displacement density over the density of the conductivity currents, during this moment for intensities on the spherical cell diameter that passes through the point A (b, c) are the following: $\varepsilon_1E_1 = \varepsilon_2E_2$; $\varepsilon_2E_2 = \varepsilon_3E_3$; $\varepsilon_3E_3 = \varepsilon_4E_4$;

$$j_i = \gamma_iE_i + \varepsilon_0\varepsilon_i\frac{\partial E_i}{\partial t}, \tag{3}$$

where $\varepsilon_0 = 8.85 \times 10^{-12}$ F/m, $i$ = 1–4, and $j_1 \ge j_2 \ge j_3 \ge j_4$ in the general case. The part of the current proceeding in the ambient space cannot proceed through the membrane and the part of the current proceeding through the membrane cannot proceed through the cytoplasm, etc. If the current density $j_i$ because of the external sources becomes equal to zero, the process of the intensity reduction of $E_i$ in the $i$ layer can be defined from the following expression:

**Table**

| $R_3/R_1$ | $E/E_0$ | |
|---|---|---|
| | $\varepsilon_4/\varepsilon_0 = 2$ | $\varepsilon_4/\varepsilon_0 = 10$ |
| 0.2 | 1.18 | 1.13 |
| 0.5 | 1.21 | 1.15 |
| 0.9 | 1.39 | 1.30 |

$$E_i(t) = E_i(t_0)e^{\frac{t_i}{\varepsilon_0\varepsilon_i/\gamma_i}}. \tag{4}$$

The constant characteristic of the time is $\tau_i$, and the field reduction from the moment of the current termination is defined by the expression from the external sources:

$$\tau_i = \frac{\varepsilon_0\varepsilon_i}{\gamma_i}. \tag{5}$$

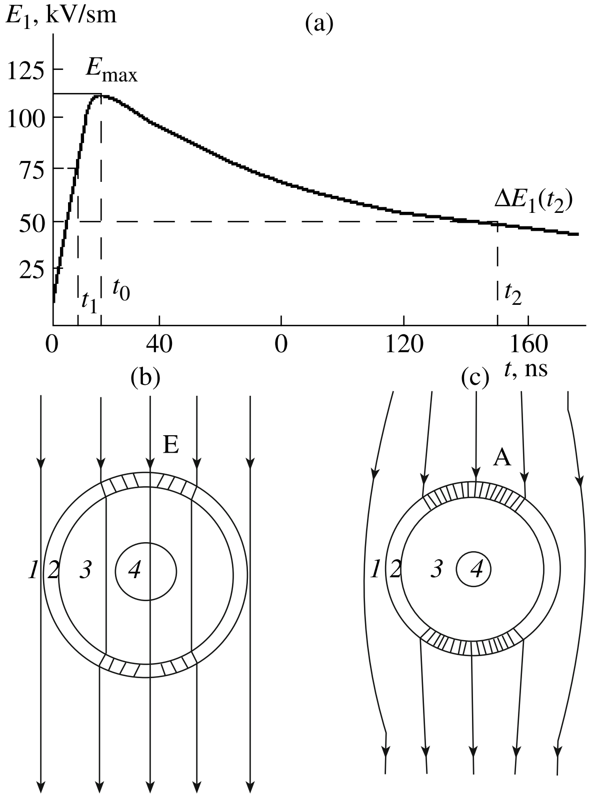

**Fig. 3.** Qualitative situation of the external electric impulse field's influence on the microbic cell in a water-containing sphere on the front ($t_1$) and on the pulse drop ($t_2$). *1*—Ambient space; *2*—cytoplasmic membrane of cell; *3*—cytoplasms; *4*—nucleus.

The following typical data for $j_i$ and $\varepsilon_1$ are obtained:

ambient: $j_1 = 10^{-1}$ (Ohm m)$^{-1}$; $\varepsilon_1 = 81$; $\tau_1 = \dfrac{\varepsilon_0\varepsilon_1}{\gamma_1} = 7.17 \times 10^{-9}$ (s),

membrane: $j_2 = 10^{-7}$ (Ohm m)$^{-1}$; $\varepsilon_2 = 2$; $\tau_2 = \dfrac{\varepsilon_0\varepsilon_2}{\gamma_2} = 1.77 \times 10^{-4}$ (s),

cytoplasm: $j_3 = 10^{-1}$ (Ohm m)$^{-1}$; $\varepsilon_1 = 81$; $\tau_3 = \dfrac{\varepsilon_0\varepsilon_3}{\gamma_3} = 7.17 \times 10^{-9}$ (s),

nuclear or procariotic chromosome: $j_4 = 10^{-7}$ (Ohm m)$^{-1}$; $\varepsilon_4 = 10$; $\tau_4 = \dfrac{\varepsilon_0\varepsilon_4}{\gamma_4} = 8.85 \times 10^{-4}$ (s).

The current density at $t = t_1$ and $t = t_2$ has approximately equal conductivity:

$$j_1E_1(t_1) = 10^{-1}\ (\text{Ohm m})^{-1} \times 75 \times 10^5\ (\text{V/m}) = 7.5 \times 10^5\ (\text{A/m}^2);$$

$$j_lE_1(t_2) = 10^{-1}\ (\text{Ohm m})^{-1} \times 50 \times 10^5\ (\text{V/m}) = 5 \times 10^5\ (\text{A/m}^2);$$

$$j_2E_2(t_1) = 10^{-8}\ (\text{Ohm m})^{-1} \times 81/2 \times 10^5\ (\text{V/m}) = 3.04\ (\text{A/m}^2);$$

$$\varepsilon_0\varepsilon_1(\partial E_1/\partial t)_{t=t1} = 8.85 \times 10^{-12} \times 81 \times (75 \times 10^5/10^{-8}) = 5.38 \times 10^6\ (\text{A/m}^2);$$

$$\varepsilon_0\varepsilon_1(\partial E_1/\partial t)_{t=t2} = 8.85 \times 10^{-12} \times 81 \times (5 \times 10^5/15 \times 10^{-8}) = 2.4 \times 10^3\ (\text{A/m}^2);$$

$$\varepsilon_0\varepsilon_2(\partial E_2/\partial t)_{t=t1} = \varepsilon_0\varepsilon_2(\varepsilon_1/\varepsilon_2)(\partial E_1/\partial t)_{t=t1} = 8.85 \times 10^{-12} \times 81 \times (75 \times 10^5/10^{-8}) = 5.38 \times 10^6\ (\text{A/m}^2).$$

From the formula resulting above, it is obvious that, because of the low specific membrane conduction, the current density of the conductivity is small in comparison with the current density of the displacement even at the maximum amplitudes of the field intensity:

$$E_2 \approx \frac{\varepsilon_1}{\varepsilon_2}E_1 \neq \frac{81}{2}100\frac{\text{kV}}{\text{cm}} \approx 4050\frac{\text{kV}}{\text{cm}}.$$

At a sharp reduction of the speed of the change of the external field intensity ($t = t_2$), the full density of the current through the membrane and, hence, in the cell decreases. If we now accept the moment of the achievement of the intensity $E_1$ at the point A to have the maximum value $E_1(t_0) = E_{1\max}$ (Fig. 3), during the time interval

$$\Delta t \geq 3 \times \tau_3, \qquad (6)$$

the field intensity in the cell cytoplasm becomes negligibly small.

The time $t_n$ during which the field rests in the cell (in the cytoplasm and organelles) for impulses with abrupt front and flat recession can be estimated by means of the following formula:

$$t_n \leq t_0 + \frac{3\varepsilon_0\varepsilon_3}{\gamma_3}, \qquad (7)$$

where $t_0$ is the duration of the impulse's abrupt front, and $\varepsilon_3$ and $\gamma_3$ are the relative dielectric permeability and specific cytoplasm conductivity.

In the considered variant (Fig. 3), $t_n = 2 \times 10^{-8} = 4.15 \times 10^{-8}$ (s). It is necessary to notice that the residence time of the field in the cell (7) depends not on its size and form but on the front steepness of the external impulse and the dielectric permeability and specific conductivity of the cell cytoplasm.

Thus, as a result of the calculations and the analysis of the influence of strong pulse fields on a biological cell, it is revealed that, with the reduction of the dielectric permeability of the cover and the increase of the dielectric permeability of the sphere, the intensity of the field and the stress on the cell membrane increase. It is established that, to influence the internal cell content, a field of high frequency is necessary; that is, complex high-voltage pulse processing should be conducted by impulses with a short front ($t_f \leq 20$ ns) and duration ($t_i \geq 100$ ns). The optimum impulse duration is connected with the sizes of the cells that are subject to inactivization. It is longer for larger characteristic cell sizes. Impulses of a field with a long front ($t_f > 20$ ns) poorly enter a cell or do not get in at all.

Consequently, according to the offered concept, it is the most expedient for the maximum inactivization effect on the microorganisms to carry out the processing by impulses with fronts of the minimum possible duration at impulses of the optimum duration (for microorganisms with the typical size $r \sim 1$ micron, $t_{i\text{opt}} \sim 0.1$–1 micron) at the maximum intensity of the amplitude that does not lead to the sphere breakdown (suspension).

## REFERENCES

1. Boiko, N.I., Bondina, N. N., and Mihailov, V.M. *Modelirovanie vozdeistviya electricheskogo polya na obecty, imeushchie mnogosloinuyu structuru* Electronnoe modelirovanie, 2002, vol. 24, no 1, p. 70–82.
2. Hulsheger, H., Potel, J., and Niemann E.G., *Killing of bacteria with electric pulses of high field strength* Radiation and Enviromental Biophysics, 1981, vol. 20. p. 53–65.
3. Volkenshtein, M.V., *Biofizika* Moscow: Nauka, 1988. p. 592.
4. Sale, A.J. and Hamilton, W.A., *Effects of high electric fields on microorganism. III. Lysis of Erythrocytes and Photoplasts* Biochimica et Biophysica Acta, 1968. vol. 163, no. 1, p. 37–43.
5. Polivanov, K.M., (Teoriya electromagnitnogo polya) part 3 *Teoreticheskie osnovy electrotehniki* Moscow: Energia, 1969, p. 352.
6. Smait, V., *Elektrostatika and electrodinamica* Moscow: IL, 1954, p. 604.
7. Benz, R. and Zimmermann, U., *Pulse-length dependence of the electrical breakdown in lipid bilayer membranes* Biochimica et Biophysica Acta, 1980, no 597, p. 637–642.

ISSN 1068-3755, Surface Engineering and Applied Electrochemistry, 2009, Vol. 45, No. 5, pp. 415–419. © Allerton Press, Inc., 2009.
Original Russian Text © M.K. Bologa, T.G. Stepurina, A.M. Bologa, A.A. Polikarpov, E.G. Sprinchan, 2009, published in Elektronnaya Obrabotka Materialov, 2009, No. 5, pp. 80–85.

# Optimization of Lactose Isomerization into Lactulose by the Electrophysical Method

**M. K. Bologa, T. G. Stepurina, A. M. Bologa, A. A. Polikarpov, and E. G. Sprinchan**

*Institute of Applied Physics, Academy of Sciences of Moldova, ul. Academiei 5, Chisinau, MD-2028 Republic of Moldova*
*e-mail: mbologa@phys.asm.md*

Received May 22, 2009

**Abstract**—The analysis of the possibilities for the lactose isomerization into lactulose and of mechanisms for its realization has been performed. The optimization of the electrophysical method to increase the obtained inverted end-product quantity is presented. The role of the amino-acid content and the nitrogen compounds in the course of the transformation and the quantitative composition of the carbohydrates are described. The electrophysical characteristics and lactose isomerization degree are defined at two processing stages.

**DOI:** 10.3103/S1068375509050135

## INTRODUCTION

Now, lactulose is the most effective prebiotic widely used as a prophylactic and therapeutic remedy for a number of diseases, especially in cases of disbiotic phenomena formation. It is only found in mother's milk, while lactose is the predominant carbohydrate in animal milk. Lactulose was first synthesized by Montgomery and Hudson during the investigation of the disaccharide structure by means of lactose thermoprocessing by an alkaline solution in 1929. In 1945–1948 Petuely and Cristan separated out a substance activating the growth of bifidobacteria from woman's milk and, not knowing its structure, defined it as the bifidus factor. It was not until 1957 that Petuely determined the chemical structure of this factor as that for a carbohydrate of the disaccharide group.

Lactulose consumers are enterprises–producers of child and therapeutic-dietary nutrition and also medicine, manufacturing more than 60 medications based on lactulose and its property as that of a strong bifidogene factor to restore the normal gut microflora. For these purposes, lactulose can be used as syrup or in the crystalline form.

The most effective way to synthesize lactulose is to transform its closest isomer lactose, which is considered to be the best but an expensive raw material. The reaction of lactose isomerization into lactulose is realized, as is known from carbohydrate chemistry, by two mechanisms. By the first one, the LA transformation of aldolase (lactose) into ketose (lactulose) occurs in an alkaline medium through the formation of intermediate epilactose and lactose of the enol form. By the second one, the Amadori rearrangement takes place and the lactose interacts with amines and forms lactosamine, which is then rearranged and turned into lactulosamine, splitting into lactulose and an initial amine [1].

The industrial production of lactose–lactulose syrups from lactose solutions is mainly based on the lactose intramolecular rearrangement by the mechanism of LA transformation in an alkaline medium. An analysis of the literary data permits one to distinguish three groups of catalysts for this reaction. Hydroxides of alkali and alkali-earth metals, which are available and inexpensive reagents permitting one to transform 30% of the lactose, belong to the first group. The high rate of the by-product formation should be classified as a disadvantage of these catalysts. The second group includes sulphites, phosphites, and other weak-alkali reagents, which predetermin decreased side reaction rates and provide a low degree of lactose isomerization into lactulose. Aluminates and borates, which are highly effective, isomerize up to 80% of the lactose, but they are toxic and hard to remove. They enter into the third group [2, 3].

Milk whey containing almost all lactose of milk belongs to the group of relatively cheap lactose-containing raw materials meeting the requirements for lactose production. A prospective method of milk whey lactose isomerization into lactulose is its electroactivation, on which the most attention was concentrated on at the International Dairy Federation Symposium (2007, Moscow). Milk whey is of especial interest as a solution for electrochemical processes. Having a relatively high content of mineral components, it possesses the properties necessary to quickly and effectively accumulate charged particles while an electrical current passes through it. It is known that the basis of electrochemical reactions is the decomposition of water and the dissociating components. Hydroxide ions forming in the catholyte play the role of proton acceptors in the reaction of lactose isomerization, and the excess internal potential energy of the activated solution intensifies the reaction of the lactose transformation into lactulose [1].

**Table 1.** Amino acid composition of IMW proteins, PMC, and irreplaceable amino acids of a standard protein (% in the protein)

| No. | Amino acids | IMW | PMC | Standard protein |
|---|---|---|---|---|
| 1 | Asparagine | 12.39 | 12.71 | |
| 2 | Serine | 4.58 | 4.39 | |
| 3 | Glutamine | 17.54 | 17.31 | |
| 4 | Proline | 3.81 | 2.73 | |
| 5 | Glycine | 2.03 | 2.13 | |
| 6 | Alanine | 4.77 | 3.77 | |
| 7 | Histidine | 1.58 | 1.97 | |
| 8 | Arginine | 2.32 | 1.83 | |
| 9 | Threonine | 5.16 | 5.08 | 4 |
| 10 | Valine | 5.27 | 4.86 | 5 |
| 11 | Isoleucine | 5.10 | 5.66 | 4 |
| 12 | Leucine | 10.38 | 10.79 | 7 |
| 13 | Tryptopha | 1.91 | 2.78 | 1 |
| 14 | Lysine | 9.29 | 9.54 | 5.5 |
| 15 | Phenylalanine | 2.94 | 3.40 | |
| 16 | Tyrosine | 3.56 | 3.83 | |
| | Phenylalanine + tyrosine | | | 6 |
| 17 | Cystine | 2.68 | 3.12 | |
| 18 | Methionine | 1.90 | 1.09 | |
| | Cystine + methionine | | | 3.5 |

It should be noted that electroactivation permits one to reach a higher degree of lactose isomerization (in curd whey up to 32%) in comparison with that for alkali catalysis (18%). The gained effect is probably reached not only due to the changes in the activation energy under the action of the electric field but owing to that the milk acid ions migrate from the catholyte, thus inhibiting the reaction of the isomerization [1].

A number of investigations were performed,and methods to increase the degree of lactose isomerization under electroactivation were developed. In particular, the addition of 1–5% of carbamide into processed whey intensifies the reaction by the second mechanism (Amadori rearrangement) [1, 4]. However, the known methods of lactose transformation by electroactivation of milk whey permit one to obtain a concentrate containing both a carbohydrate constituent enriched by lactulose and a protein fraction, thus limiting its application. Moreover, the preliminary heating of the whey to a temperature of more than 55°C induces the thermal denaturation of the proteins.

The authors [5, 6] suggested a method of milk whey electrophysical processing with the simultaneous production of a protein–mineral concentrate (PMC) and residual whey (RW) containing inverted lactulose. However, the lactose concentration in the partially deproteinized and demineralized residual whey is relatively high, and this predetermines the continuation of investigations on the optimization of the residual lactose isomerization process. For this purpose, the stage-by-stage electroactivation of whey was conducted, while varying the composition of the anodic and cathodic liquids.

## RESULTS AND DISCUSSION

Curd whey cooled to 8–10°C and purified from casein powder using a mass force field was used for the processing. The main parameters regulating the processes of the PMC production and the lactose isomerization into lactulose are the electric current density, the composition of the anodic and cathodic solutions, the feed rate of the liquid entering into the chambers, and the membrane type. The combination of these factors defines the degree of increase in the temperature and the actual acidity in the cathodic chamber and also the change in the voltage and membrane state. The process of the electroactivation was conducted in two stages. At the first stage, the initial milk whey (IMW) was processed in the cathodic chamber (CC) of an MK-40 diaphragm electrolizer with an ion-exchange chamber in steady-state conditions at the electric current density of 0.02 A/cm$^2$ for 30 min. A 2% solution of calcium chloride in distilled water served as the anodic liquid. The PMC foam was separated from the RW in a mass force field.

The choice of calcium chloride, first, to provide the electroconductivity and, second, to increase the amount of protein transferring into the PMC is caused by the role of the calcium ions, i.e., their migration into the cathodic chamber in the process of the protein complexing and also by its availability and nontoxicity. Furthermore, the obtained product is enriched by mineral components, whose role in the vital functions of organisms is widely known.

It has been established that the maximal protein amount (up to 65%) transfers into the PMC at 2% of calcium chloride in the anodic solution. At this concentration, the process of foaming becomes more intensive from the very beginning of the treatment with the resulting formation of more stable foam, and this correlates with the protein transfer into the concentrate. The whey processing within the interval of temperatures below the thermal protein denaturation threshold of 55–65°C is one of the purposes of the investigation, as only in this case is the activity of the amino groups taking part in the reaction of the lactose transformation into lactulose conserved [5].

All the IMW protein fractions are present in the MC, as the electrophoretic spectrum of its proteins indicates. This provides balanced amino acid compositions of the PMC proteins confirmed by the results of Table 1. The distinctions between the contents of some amino acids in the PMC and IMW show that the degrees of transfer of the whey protein's main fractions into the concentrate are different. The PMC protein contains all the irreplaceable amino acids present in standard protein, which is the etalon of the irreplaceable amino acid content in complete protein, and basically exceeds their content in the latter.

The carbohydrate contents in the lyophilized PMC samples, which were taken as the actual acidity increased in the cathodic chamber, were summarized in Table 2. It can be seen from the table that the carbohydrate constituent content changes nonlinearly, increasing gradually by the end of the process. In the summary of the lyophilized PMC, the quantity of carbohydrates does not exceed 2.1%; at that, only 0.4% of the IMW carbohydrates transfer in the concentrate. It is most likely that their greater part passes into the PMC together with the protein at the stage of lactose amination by active protein amino groups. However, such a low content of carbohydrates does not interfere with the prolonged dry concentrate storage.

At the first stage of the IMW electroactivation, the lactose isomerization into lactulose is realized by two mechanisms but to a greater extent according to the mechanisms of the LA transformation induced by the accumulation of proton acceptors arising from the electrochemical reactions. Moreover, the albuminous components and amines (free animo acids, urea, uric acid, creatine, etc.), which are contained in whey, can benefit the reaction by the mechanism of Amadori rearrangement. Some amines passing into whey in the form of free amino acids are formed during the partial hydrolysis of proteins as a result of the primary technological processes of the milk processing (the milk and curd production) and also as the products of the vital activity of the microorganisms used for the milk fermentation.

Aminestaking part in the reaction of lactose isomerization into lactuloseare released with this reaction completed as a result of the actulosamine splitting. The significant changes in the concentrations of the nonprotein amino compounds in RW in the course of its processing demonstrate (Table 3) which of them are bounded with the carbohydrate base, i.e., are in one of the intermediate forms of the reaction.

As the whey treatment conditions observed at the first processing stage (Figs. 1 and 2) do not exceed the optimal values for the process of the lactose isomerization into lactulose [7, 8] by the temperature and actual acidity and partially or completely exclude the formation of by-products, the isomerization degree was judged from the decrease in the lactose concentration in the RW. The residual protein was precipitated by trichloracetic acid in the RW samples taken as the pH value increased and also in the whey taken from the cathodic chamber after the processing; then, the lactose concentration was determined by polarimetry and calculated from the calibration curve.

**Table 2.** Carbohydrate concentration by Dubois in the PMC at different pH values

| Processing time, min | pH | Carbohydrate concentration, % |
|---|---|---|
| 5 | 6.60 | 0.8 |
| 10 | 7.30 | 1.29 |
| 15 | 7.75 | 1.20 |
| 20 | 9.75 | 2.10 |
| 25 | 10.95 | 2.54 |
| 30 | 11.25 | 2.61 |

**Table 3.** Nonprotein nitrous component concentrations in processed (residual) milk whey

| Processing time, min | pH | Urea, mg/% | Creatine + creatinine, mg/% | Uric acid, mg/% |
|---|---|---|---|---|
| 0(IMW) | 5.05 | 11.03 | 5.98 | 1.15 |
| 5 | 6.60 | 7.41 | 4.01 | 0.36 |
| 10 | 7.30 | 6.52 | 3.56 | 0.18 |
| 15 | 7.75 | 6.07 | 3.47 | 0.11 |
| 20 | 9.75 | 6.05 | 5.15 | 0.90 |
| 25 | 10.95 | 3.38 | 5.85 | 0.35 |
| 30 | 11.25 | 1.91 | 4.85 | 0.04 |

A significant decrease in the quantity of the lactose in the processed whey is observed when the pH exceeds 9.5 (Fig. 4a). Its concentration in the overall volume of the RW samples and the cathodic residual whey (CRW) is approximately 40% of the IMW. The absence of typical indications for the by-products of the isomerization permits one to suppose that about 60% of the whey lactose transforms into lactulose.

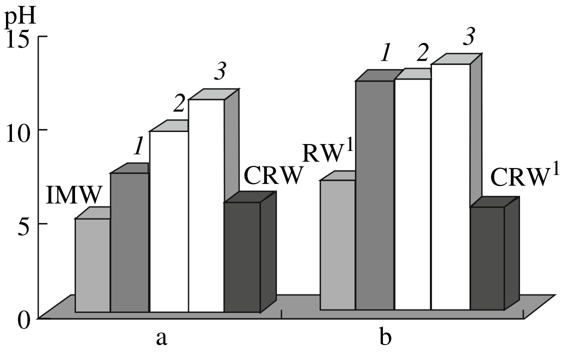

**Fig. 1.** Processed whey's pH changes under electroactivation; (a) first processing stage: the cathodic liquid is IMW, the anodic liquid is 2% calcium chloride. (b) second processing stage: the cathodic liquid is 1% carbamide in RW (RW$^1$), the anodic liquid is 1% calcium chloride. Processing time, min: (*1*) 10; (*2*) 20; (*3*) 30.

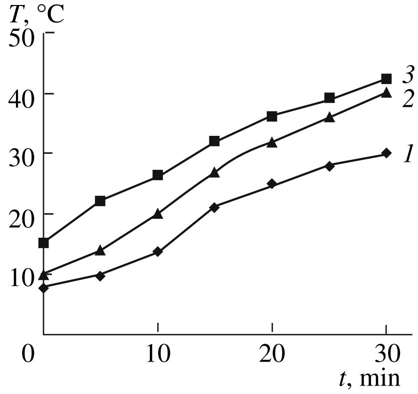

**Fig. 2.** Processed whey's temperature changes under electroactivation. First processing stage: (*1*) the cathodic liquid is IMW, the anodic liquid is 2% calcium chloride. Second processing stage: (*2*) the cathodic liquid is 1% carbamide in RW (RW$^1$), the anodic liquid is 1% calcium chloride; (*3*) the cathodic liquid is 1% carbamide in RW (RW$^1$), the anodic liquid is 0.5% calcium chloride.

1% carbamide was added to the partially deproteinized and demineralized RW (RW$^1$) that was obtained at the first electroactivation stage and had an actual acidity of 7 and contained 40% lactose and 35–40% whey protein, whereupon the RW$^1$ was processed again in the CC. The addition of carbamide in the RW, in which the amine concentration decreased considerably in comparison with that in the IMW, induced the reaction of lactose isomerization into lactulose by the mechanism of Amadori rearrangement along with the reaction by the pattern of LA transformation. In one variant, a 0.5% calcium chloride solution was used as the anodic liquid and, in the other variant, a 1% calcium chloride solution was used.

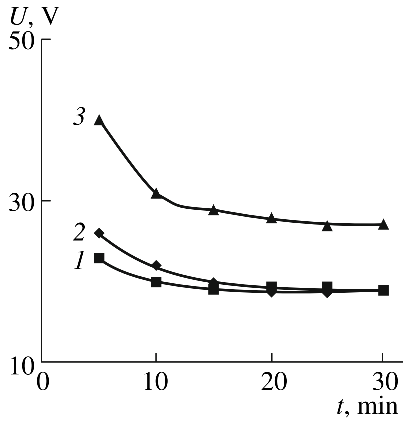

**Fig. 3.** Voltage changes under electroactivation. First processing stage: (*1*) the cathodic liquid is IMW, the anodic liquid is 2% calcium chloride. Second processing stage: (*2*) the cathodic liquid is 1% carbamide in RW (RW$^1$), the anodic liquid is 1% calcium chloride; (*3*) the cathodic liquid is 1% carbamide in RW (RW$^1$), the anodic liquid is 0.5% calcium chloride.

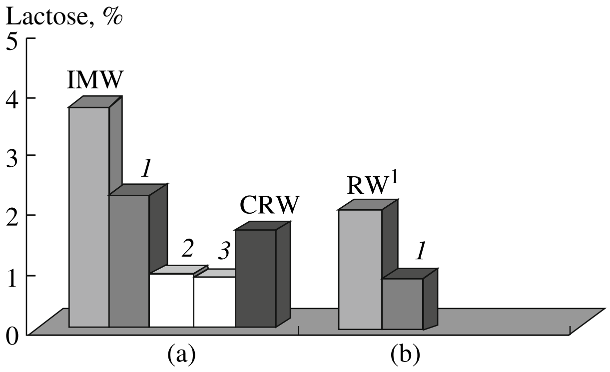

**Fig. 4.** Changes of the lactose concentration in processed whey under electroactivation; (a) first processing stage: the cathodic liquid is IMW, the anodic liquid is 2% calcium chloride; (b) the second processing stage: the cathodic liquid is 1% carbamide in RW (RW$^1$), the anodic liquid is 1% calcium chloride. Processing time, min: (*1*) 10; (*2*) 20; (*3*) 30.

At the second processing stage, the calcium chloride concentration in the anodic solution was decreased in connection with the RW enrichment by calcium ions. The electroactivation process was conducted under the same conditions as that for the first stage.

At the second processing stage, the temperature in the CC increases more quickly for the variant with the lower calcium chloride concentration (0.5%) in the anodic liquid. It is evident that, in this case, the quantity of energy resourses decreases faster in comparison with the second variant with the use of a 1% calcium chloride solution (Fig. 1, curves *3* and *2*). The calcium chloride concentration also defines the value and degree of the voltage changes in the electroactivation process (Fig. 3, curves *3* and *2*).

Already within 5–7 min from the beginning of the second processing stage, a sharp increase in the pH of the RW$^1$ to the value corresponding to the lactose inversion optimum (pH of 11.0–11.5) is observed (Fig. 1b). In the further course of the process, the actual acidity increases much more lowly, and this is caused by the formation of colored isomerization by-products having the acidic properties of the RW$^1$ [1]. The degree of their accumulation is so high that, by the end of the process, the pH of the whey from the CC is lower than that for the nitial RW$^1$. It is obvious that the reprocessing of the RW should be conducted under the given conditions no longer than for 7 min to convert the lactose into lactulose. In this time interval, the lactose content in the RW$^1$ is reduced by 55% (Fig. 4b). As a result of the two electroactivation stages, the decrease of the lactose reaches 80%.

At the second stage, the formation of the MC is also observed. The quantity of protein that passes into the concentrate in the first 7 minutes of the process correlates with the calcium chloride concentration in the anodic solution and reaches 15–25% of the protein in the RW[1].

Consequently, the stage-by-stage electrophysical processing of the milk whey permits one not only to increase the lactose–lactulose product yield but to obtain two types of protein concentrate.

## REFERENCES

1. Khramtsov, A.G., Ryabtseva, S.A. and Suyuncheva, B.O., Investigation of the Process of Lactose Isomerization into Lactulose under Milk Whey Electroactivation, *Vestnik SevKavkGTU, ser. "Prodovol'stvie"*, 2004, no. 7, pp. 20–27.
2. Khramtsov, A.G., Sinel'nikov, B.M., Evdokimov, I.A., Ryabtseva, S.A. and Serov, A.V., Scientific and Technical Foundations of Lactulose Technology, *Vestnik SevKavkGTU, ser. "Prodovol'stvie"*, 2004, no. 7, pp. 12–18.
3. Khramtsov, A.G., Evdokimov, I.A., Ryabtseva, S.A., Serov, A.V., Lodygin, D.N., Polischuk, D.O., Kharitonov, D.V., Samoilov, V.A., Nesterenko, P.G. and Zhurba, L.N., Analysis of Information File Data on the Methods for the Lactulose Concentrate Production, *Vestnik SevKavkGTU, ser. "Prodovol'stvie"*, 2003, no. 6, pp. 61–64.
4. Khramtsov, A.G., Ryabtseva, S.A., Suyuncheva, B.O., Evdokimov, I.A., Nesterenko, P.G., Lodygin, A.D., Myachin, A.F. and Panova, N.M., RF Patent 2260286, 2005.
5. Sprinchan, E.G., Optimization of technological regimes for obtaining protein-mineral concentrated products from secondary milk raw materials, *Elektronnaya obrabotka materialov*, 2009, no. 1, pp. 73–80 [*Surf. Eng. Appl. Electrochem.*, (Engl. Transl.), vol. 45, no. 1, pp. 63–70].
6. Bologa, M.K., Stepurina, T.G., Bologa, A.M., Polikarpov, A.A. and Sprinchan, E.G., MD Inventor's Certificate no. 0065, 2009 (unpublished).
7. Khramtsov, A.G., Ryabtseva, S.A. and Zhurba, L.N., Regularities of the Process of Lactose Isomerization into Lactulose in Cheese Whey, *Vestnik SevKavkGTU, ser. "Prodovol'stvie"*, 2003, no. 6, pp. 16–20.
8. Khramtsov, A.G., Panova, N.M., Ryabtseva, S.A., Evdokimov, I.A., Lodygin, A.D., Chabaev, M.G., Development of the Technology of Bifidoactive Feedstuff Additives Based on Milk Protein-Carbohydrate Raw Materials, *Vestnik SevKavkGTU, ser. "Prodovol'stvie"*, 2002, no. 5, pp. 67–68.

ISSN 1068-3755, Surface Engineering and Applied Electrochemistry, 2009, Vol. 45, No. 5, pp. 420–423. © Allerton Press, Inc., 2009.
Original Russian Text © Yu.A. Dashkovskii, 2009, published in Elektronnaya Obrabotka Materialov, 2009, No. 5, pp. 86–90.

## ELECTRICAL PROCESSING OF BIOLOGICAL OBJECTS AND FOOD PRODUCTS

# Mechanism of Microorganism Destruction by the Influence of Shock Waves

**Yu. A. Dashkovskii**
*National University of Food Technologies, ul. Vladimirskaya 68, Kiev, 01033 Ukraine*
*e-mail: a_marinin@ukr.net*

Received June 20, 2009

**Abstract**—At a powerful impulse discharge in the medium with the thickness of front much less than a characteristic size of microorganisms, that can be explained as a mechanism of microorganisms destruction by a shock wave. The most creadible mechanisme of the destruction is the crushing due to the development of instability within the overflow region.

**DOI:** 10.3103/S1068375509050147

The knowledge-intensive application of electrospark columns for the changing of foodstuff properties and semiproducts is carried out at the State University of Nutrimental Technologies in Kiev. In the course of the experiments, the influence of the electrohydraulic effect on the life support of nutritive sphere microflora is established.

In this investigation, the possible mechanisms of microorganism destruction using the influence of the electrohydraulic effect (EHE) are considered.

In many cases, the changing of the multiphase sphere is accompanied by a change of the functional structure of the discrete containments owing to the coagulation and splitting up of particles. This phenomenon is extremely important for studying the streaming structure and its laws, as the particles' dispersion and their concentration make a defining impact on the process intensity carrying over in multiphase systems and, finally, on the basic integrated characteristics.

At the experimental and theoretical researching of gas particles of the condensed phase, one of the main parameters is defining the character of the value for the particles [1, 2].

In work [1], it is noticed that the starting of the splitting up of the drops is defined by the Weber number value in the shock waves:

$$We^* = \rho u^2 d(2\sigma)^{-1} \approx 5–8, \tag{1}$$

where $\rho$ and $u$ are the density and the speed of the gas, $d$ is the value of the drops, and $\sigma$ is the superficial tension of the liquid at $P_0 = 0.5–1.2$ MPa.

The researchers of the liquids took the water $\rho_f = 1000$ kg/m$^3$, the viscosity $\mu_f = 1$ MPa s, and $\sigma = 75$ MN/m. The droplet diameter in the experiments was $d = 2$ mm during the time moments of 100 and 200 μs.

The sound speed and density values are determined according to the following formulas:

$$\frac{a}{a_0} = \left(\frac{P}{P_0}\right)^{\beta}; \quad \frac{\rho}{\rho_0} = \left(\frac{P}{P_0}\right)^{\frac{1}{\gamma}}; \quad \beta = \frac{(\gamma - 1)}{2\gamma}, \tag{2}$$

The value of the Reynolds number is determined according to the following formula:

$$Re = \frac{\rho u d_0}{\mu},$$

where $\mu$ is the gas viscosity.

In E. Mauer's study [3], the microparticles' sizes are estimated by a value proportional to the average length of the wave perturbations:

$$d_1 = A\lambda_i \tag{3}$$

where $A = 0.2$.

At low motion energy $\varepsilon_v$, the splitting up almost always occurs in the form of threadlike sputtering, and it is equal to $0.9 \times 10^{-6}$ J. Splitting up in the form of the electron-beam evaporated film occurs at the superficial energy $W \geq W_e^* = 0.86$.

However, this list of parameters is apparently not full: the destruction conditions depend on the Mach and Bond numbers [2], on rate of the turbulence stream increase, and on the aerodynamic forces.

The cell's structure is damaged owing to the thermal or mechanical effect according to the general principle of the destruction: the value of the major factor of the destroying influence should simultaneously surpass some values in intensity and duration and could be one of the reasons for the bacterial destruction. For this reason, it is necessary to search for the generalized criterion of the destruction in the following relation:

$$(We - We^*)(I - I^*) = \text{const}, \quad I = \int_0^t \rho u^2 dt, \qquad (4)$$

where $I$ is the dynamic pressure impulse in the wave.

Until then, while $We < We^*$ or $I < I$ , the drops do not collapse. But, at $We \geq We^*$, the final time for the destruction is required.

The front gage is defined by the density value before and behind the front connected by the formula for the rupture:

$$\delta = (\rho_2 - \rho_1)/(d\rho/dx)_{\max}.$$

With the differential pressure increase, the gage front decreases within $\delta \approx (60 - 4)$ nm.

At $\Delta P \geq 50$ MPa [9], the front gage is essentially less than the characteristic value of the microorganisms (~1–10 nm); for the estimation of the specified effects, the hydrostatic and dynamic approaches are applicable. The microorganisms' heating as a result of the shock wave passage can be estimated according to the formula [4]

$$T/T_0 = (V/V_0)^{-\Gamma_0}.$$

At this point, the change of the specific volume $V/V_0$ is defined from the Tate equation and the Grunaizen factor:

$$\Gamma_0 = \frac{\beta}{\rho k_m c_v},$$

where $k_m$ is the isothermal factor of the compressibility, $\beta$ is the volumetric coefficient of the thermal expansion, and $c_v$ is the specific heat capacity.

For water, $\Gamma_0 = 108.85$; for the organic liquid, $\Gamma_0 = 952.40$.

One of the distinctive features of the turbulent structural courses is connected with the presence of a distinct nonstationary surface that differentiates the turbulent swirling flow in the stream from the not turbulent (laminar) flow out of the stream. A swirling flow can be transferred in a potential liquid only at direct contact through the action of viscous shifting forces.

At the expense of the viscous forces in this layer, the swirling flow sharply changes from zero to the final value.

The gage of this layer has an order on Kolmogorov's scale [10] and is defined by the formula

$$l \approx \left(\frac{\nu^3}{E}\right)^{1/4}, \qquad (5)$$

where $\nu$ is the kinematic viscosity, and $E$ is the dissipation rate of the oscillatory energy in the turbulent liquid.

It is possible to connect $E$ with the least square speed $u'$ and approximately integrated the scale $L$:

$$E \approx (0.2\text{–}0.4)\frac{(u')^3}{L}.$$

If the energy entered into the circumference turns to warmth, the energy dissipation can be approximately presented as

$$E = \frac{N}{V_{\text{liquid}}}, \qquad (6)$$

where $N$ is the columny capacity.

For our calculations, $L \approx R$, where $R$ is the chamber radius. Then, (5) will be copied differently:

$$\frac{1}{L} \approx \frac{1}{\text{Re}_L^{3/4}},$$

where $\text{Re}_L = \dfrac{u'l}{\nu}$.

That is to say the relative gage of this viscous layer (interface) with growth of Re decreases quickly enough and makes up millimeters, as a rule, it is almost commensurable with the sizes of the microorganisms.

For the mechanical effect estimation, we suggest microorganisms as spheres with the diameter $d$, and we will take advantage of the split-up condition of the globes of liquid at the density $\rho_0$ owing to the development of Kelvin–Helmholtz instability at the density flow $\rho$ [5]:

$$\Delta P > \rho^{1/2} D \left(\frac{2\pi\sigma}{d}\frac{\rho}{\rho_0}\right)^{1/2}, \qquad (7)$$

where $D$ is the shock-wave speed, and $\sigma$ is the surface tension force on border section. $D = \dfrac{1}{2}\left(\dfrac{W_0}{\alpha\rho_0}\right)^{1/4} t_p^{-1/2}$, where $W_0$ is the explosive energy, $\alpha = 0.01$ for water, and $\alpha = 0.002$ for the system's water and chipping.

The gage of the microorganisms' cellular wall, having a polymeric structure, is $\Delta = 10\text{–}25$ nm, and, as the pressure of the rupture for the liquid $\sigma_p = \dfrac{2\sigma}{r_0}$ is connected with the superficial tension with the approximate relationship [5], formula (7) can be applied in the considered case if we formally replace the value $\sigma$ on $\sigma^* = \dfrac{\sigma_1\Delta}{r_0}$ or $\sigma^* = \sigma_p\Delta$, where $\sigma_1$ and $\sigma_p$ are the surface tension and strength on breaking of the material of the cellular wall. The typical values of $\sigma_p$ for polymers are ~20 MPa [7], and, according to [7], we obtain the split-up conditions of the globes at the differential pressure $\Delta P > (0.6\text{–}1.35) \times 10^2$ MPa.

With the knowledge of thedissipation of the oscillatory energy in the turbulent stream and using "the law

**Table 1**

| $r$, cm | 2 | 4 | 6 |
|---|---|---|---|
| $P$, atm | 12750 | 3187 | 1417 |
| $\varepsilon$, J | 83 | 19.6 | 8.7 |

**Table 2**

| $r_2$, sm | 8.4 | 11.2 | 14.0 | 16.8 |
|---|---|---|---|---|
| $P_2$, atm | 846.8 | 521.6 | 361.5 | 270.7 |

of two-thirds" of Kolmogorov and Obuhov [10], let us define the least pulsation scale $l_0$ and compare it with the size of the microorganisms that underwent the treatment. This value we find from the condition of the comparison of the speed energy of the turbulent pulsation transformation on the volume unit $\Delta E$ and the capillary by the pressure $P^*$, which infers deformation and rupture [11]:

$$\Delta E = P^*, \quad \Delta E = \frac{\rho \upsilon_l^2}{2}. \tag{8}$$

As the gas density is less than the liquid density, the gas speed is close to the average oscillatory speed of the adjoining liquid, and the former, according to "the law of two-thirds," can be found from the expression $\upsilon_l^2 = \left(\frac{\varepsilon l_0}{\rho}\right)^{2/3}$, which is the law of two-thirds.

At $l \le l_0$, where $l_0 = \sqrt[4]{\frac{\nu^3}{\varepsilon_0}}$, $\varepsilon_0$ is the average energy dissipation on the mass unit, W/kg, and $\varepsilon_0 = \frac{\varepsilon}{\rho}$, where $l_0$ is the internal pulsation scale.

Capillary pressure is

$$P^* = \frac{2\sigma}{d_{\rm P}} \tag{9}$$

where $d_{\rm P}$ is the droplet diameter.

At $l_0 \sim d_{\rm P}$, the simultaneous solution of equations (8) and (9) will lead to

$$\frac{2\sigma}{d_{\rm P}} = \frac{\rho}{2}\left(\frac{\varepsilon d_{\rm P}}{\rho}\right)^{2/3},$$

whence it follows that $d_{\rm P} = 2.3 \times \sqrt[5]{\frac{\sigma^3}{\rho\varepsilon^2}}$.

For the origination of shock wave's basic characteristics that influence the microorganisms, the point explosion hypothesis in a compressed liquid is applicable. Thus, the energy of the electric columny is taken as the explosion energy.

The big capacity the condensed spark column, which is measured in thousands of kilovolts, occurs. For example, in the conditions of our experience, at $C = 4$ uF, $U = 35$ kv, and $t_p = 18$ mks, the average capacity of the columny $N = 1.36 \times 10^5$ kW.

At small distances from the axis of the columny channel, the shock wave extends with cylindrical symmetry ($r < 10$ sm), which corresponds to the columny symmetry, and, at great distances, the shock wave extends with spherical symmetry, as from a point source.

Let's calculate the explosion energy of $W_0$ at $l_{\rm P} = 4$ sm, which is the distance between the electrodes, where $W_0 = \frac{CU^2}{2l_{\rm P}} = 0.6 \times 10^{10}$ erg/sm.

Let's assume that, at the moment $t = 0$ in the sphere at rest, in the symmetry center an explosion occurs.

The pressure of the shock wave [8] is

$$P = 8.2\frac{W_0}{r^2}, \tag{10}$$

where is shock wave radius.

For cylindrical symmetry,

$$r = \left(\frac{W_0}{\alpha\rho_0}\right)^{1/4} t_p^{1/2}. \tag{11}$$

The calculation data according to formulas (11) and (10) are in Table 1.

The internal energy analysis we do according to the formula

$$\varepsilon = \frac{PV}{(\gamma - 1)}. \tag{12}$$

The shock wave extends with spherical symmetry at great distances from the place of the explosion. It is determined from the formula [8]

$$P_2 = \frac{P}{\bar{r}}\frac{1 + 4(ln\bar{r})^{1/2}}{\sqrt{1.15 ln\bar{r} - 0.5}}, \tag{13}$$

where $r_0$ are the shock wave radius changes according to the law $r_0 = \beta\left[\frac{W_0}{\rho_0 a_0^2}\right]^{1/3}$, $a_0 = \sqrt{\frac{3040 \times 7.15}{\rho_0}}$; $\beta = 0.3$, and $\bar{r} = \frac{r_2}{r_0}$, where $P_2$ is the pressure behind the wave front.

The parameter $\beta$ can be defined if we know $P_2$ for some distance $r_2$ from the explosion center set at $W_0$.

The $P_2$ calculation data according to formula (13) are in Table 2.

At a powerful columny pulse in the sphere, the shock wave arises and forms in the immediate proximity of the columny axis at a distance of ~3–5 mm from it.

At the differential pressure $\Delta P > 50$ MPa, the front capacity is much less than the characteristic size of the microorganisms. It is possible to consider it as the mechanism of the microorganisms destruction by the shock wave and the most probable is the split-up owing to the development of instability at the flow.

Thus, the differential pressure $\Delta P > (0.6–1.35) \times 10^2$ MPa serves as a reference point for the practical realization of the conditions of the microorganisms destruction at the unitary influence of the columny.

The dependence of the pressure on the shock wave from its radius for the given experiment allows us to estimate the source of the drops' rupture.

The microorganisms' diameters are almost commensurable with the gage of the viscous layer; therefore, it is possible to define the Reynolds number from (7) at which the drops splitting up occurs.

The resulting analysis testifies that there is a range of parameters of energies of the turbulent pulsations at which the order of the values of the pulsations is comparable with the values of the microorganisms on the basis of "the law of two-thirds." Thus, the more the speed value of the energy dissipation, the less the pulsations value; that is, processing energy with great power consumption is really capable of destroying or damaging the walls of microorganisms.

## REFERENCES

1. Loparev, V.P., *Eksperimentalnoe issledovanie drobleniya kapel zhidkosti v usloviyah postoyannogo narastaniya vneshnih sil* Izvestiya, Soviet Socialist Republic, 1975, no 3, p. 174–178.
2. Ivandaev, A.I., Kutushev, A.G., and Nigmatulin, R.I., *Gazovaya dinamica mnogofazovyh sred. Udarnye i detonatsionnye volny v gazovzvesyah* Itogi nauki i tehniki, All-Union Institute of Scientific and Technical Information of Mechanical liquid and gas, 1981, p. 209–290.
3. Mayer, E., *Theory of liquid atomization in high velocidy gas streams* ARSj, 1961, V. 31, no. 12.
4. Zeldovich, Ya.B. and Raizer, Yu.P., *Fizica udarnyh voln i vysokotemperaturnyh gidrodinamicheskih yavlenii* Moscow: Nauka, 1966, p. 688.
5. Gelfand, B.E, Gubin, S.A., Nigmatulin, R.I., et al., D. Academy of Sciences, Soviet Socialist Republic, 1977, vol. 233, no 2, p. 292–294.
6. Frenkel, Ya.I. *Kineticheskaya teoriya zhidkostei* Leningrad: Nauka, 1975, p. 592.
7. *Fizicheskie velichiny: Spravochnik*, Grigoreva, N.S., Meilihova, E.Z., et al., Eds., Moscow: Energoizdat, 1991, p. 1232.
8. Astrahan, I.M. *Davlenie na udarnoi volne pri silnom iskrovom razryade vody* Izvestiya vuzov, Neft i gaz, 1959, no 2, p. 27–32.
9. Yakovlev, U.S., *Gidrodinamica vzryva* Leningrad: Sudpromgiz, 1961, p. 316.
10. Kolmogorov, A.N., *Localnaya structura turbulentnosti v neszhomaemoi vyazkoi zhidkosti* D. Academy of Sciences, Soviet Socialist Republic, vol. XXX, no 4, 1941, p. 19–21.
11. Levich, V.G. *Fiziko himicheskaya gidrodinamica* Moscow: Fizmatgiz, 1959.

ISSN 1068-3755, Surface Engineering and Applied Electrochemistry, 2009, Vol. 45, No. 5, pp. 424–429. © Allerton Press, Inc., 2009.
Original Russian Text © V.N. Tsurkin, A.V. Mel'nik, 2009, published in Elektronnaya Obrabotka Materialov, 2009, No. 5, pp. 91–96.

EQUIPMENT
AND DEVICES

# Processes and Character of Melt Loading by Electrodischarge Generator of Vibrations on Resilient Elements: Part II (Propagation of Disturbances)

**V. N. Tsurkin and A. V. Mel'nik**

*Institute of Pulse Processes and Technologies, National Academy of Sciences of Ukraine,*
*Oktyabr'skii pr. 43-A, Nikolaev, 54018 Ukraine*
*e-mail: dpta@iipt.com.ua, iipt@iipt.com.ua*

Received June 2, 2009

**Abstract**—On the basis of numerical modeling of hydrodynamic processes occurring in melt under electrohydropulse treatment, the field of pressures in liquid metal at the postdischarge stage is calculated. It is shown that the application of waveguide attachments allows increasing the pressure levels at the initial stage of treatment, the share of energy being dissipated in the melt, and the cavitation duration. It is determined that the efficiency of treatment is stipulated by the geometrical size correlation of a working element and a ladle.

**DOI:** 10.3103/S1068375509050159

## INTRODUCTION

The functional possibilities of electrohydropulse treatment (EHPT) of the melt in a ladle are stipulated by the formation of various physical processes (interior structural kinetic alterations) in liquid metal which promote quality improvement of the casting metal [1, 2]. The melt is an acoustic medium; therefore, the pulse disturbances occurring under its loading create in this medium a nonstationary field of pressures—the main factor which affects the casting metal structure.

The source of disturbances in the melt during EHPT is an electrodischarge generator of resilient vibrations (EDGRV), which by means of a working element (a membrane with a waveguide) acts upon the metal by resilient waves.

A number of publications [3, 4] are devoted to investigations of hydrodynamic phenomena in liquid metal of the melt in a ladle during EHPT. However, the results displayed in these papers are limited to the standard calculation schemes of technological devices. Moreover, beyond the view of investigators remained the variant of constructive performance of a transfer element with a plane circular attachment, the diameter of which exceeds the one of a waveguide severalfold. The application of such a configuration may significantly expand the EHPT functional capacities.

The purpose of the present paper is to determine by the methods of numerical modeling the hydrodynamic processes occurring in the melt under the influence of working parameters of EDGRV on resilient elements and a nonstationary field of pressure originating in the metal under treatment at a postdischarge stage of the process.

## THEORETICAL INVESTIGATION

Suppose there is a plane two-dimensional axisymmetric problem on propagation of disturbances in an acoustic medium (melt) (Fig. 1). The geometrical parameters of constructive elements and physical properties of the melt correspond to the ones adopted in the first part of study [5]. Owing to the fact that the main contribution to formation of disturbances caused by the

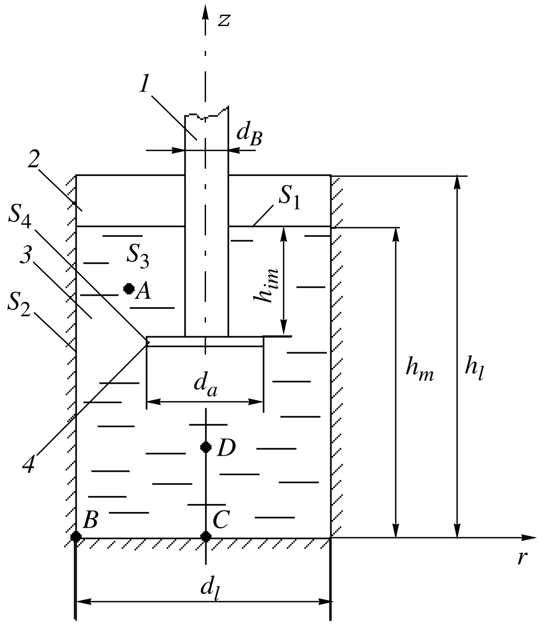

**Fig. 1.** Diagram of melt treatment in ladle by waveguide with attachment: (*1*) waveguide; (*2*) ladle; (*3*) melt; (*4*) waveguide attachment.

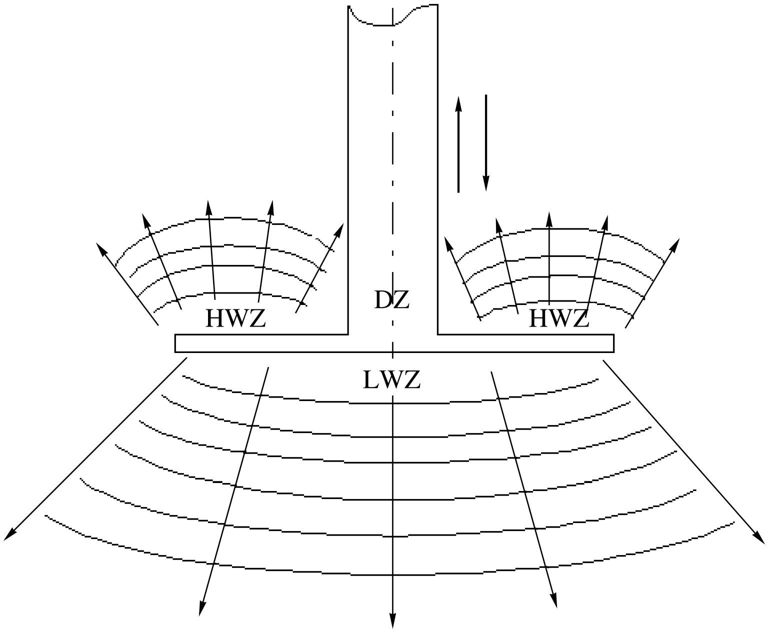

**Fig. 2.** Zones of influence on the melt during EHPT: (*LWZ*) lower working zone; (*HWZ*) higher working zone; (*DZ*) "dead" zone.

propagation of longitudinal waves is made by the end of the waveguide, and not by its side surface, we consider the influence of the waveguide attachment only in the form of a plane absolutely hard disk, immersed in the melt to a certain depth. In this case, the local working zones of effective action are considered to be the whole lower plane of the attachment as well as a part of its upper plane to its point of attachment to the end of the waveguide (see Fig. 2). The region of attachment directly under the waveguide end, where the effects of the action are insignificant, will by convention be called the "dead zone."

Since the rate of motion of the waveguide end is small in comparison with the sound velocity in the metal melt [3], and the value of vacuum pressure is limited by the mechanism of formation of cavitation processes [6], we shall describe the motion of the melt in the acoustic approximation by means of the wave equation in rate potentials under the condition of cavitation occurrence:

$$\frac{\partial^2\psi}{\partial t^2} - c_0^2\left[\frac{\partial^2\psi}{\partial z^2} + \frac{1}{r}\frac{\partial}{\partial r}\left(r\frac{\partial\psi}{\partial r}\right)\right] = 0 \quad P > P_{\mathrm{cr}}; \tag{1}$$

$$\frac{\partial^2\psi}{\partial t^2} + \frac{P_{\mathrm{cr}} - P}{\rho_0} = 0 \quad P \le P_{cr}, \tag{2}$$

where $\psi(r, z, t)$ is the potential of the rate; $V_z = \frac{\partial\psi}{\partial z}$, and $V_r = \frac{\partial\psi}{\partial r}$ are the axial and radial constituents of the rate; $\rho_0$ and $c_0$ are the density and sound velocity in undisturbed liquid metal, respectively; $r$ and $z$ are spatial coordinates; $t$ is time; and $P$ and $P_{\mathrm{cr}}$ are the pressure and strength at static stretching in the melt, respectively.

The pressure in the zone of developed cavitation is commensurable with the pressure of saturated vapor of the liquid; therefore, for the convenience of calculation, the supposition $P_{\mathrm{cr}} = 0$ is accepted.

The correlation of the rate potential with pressure is found to be

$$P = -\rho_0\frac{\partial\psi}{\partial t}.$$

On the walls of ladle $S_2$, the side surfaces of waveguide $S_3$, and attachment $S_4$, no-fluid-loss boundary conditions (normal components of the rate equal zero) are set:

$$\frac{\partial\psi}{\partial\vec{n}} = 0,$$

where $\vec{n}$ is a surface normal. At a free surface of the melt $\Pi_1$, the excess pressure equals zero; i.e., the condition $\frac{\partial\psi}{\partial t} = 0$ is met.

The initial conditions are the values of the waveguide end rates, calculated during examination of the dynamics of the waveguide-radiation system at the previous stage [5]. Note that Eq. (1) also takes into account the phenomenon of wave reflection from the ladle walls, the waveguide side surface, the upper and lower attachment planes, and the melt free surface.

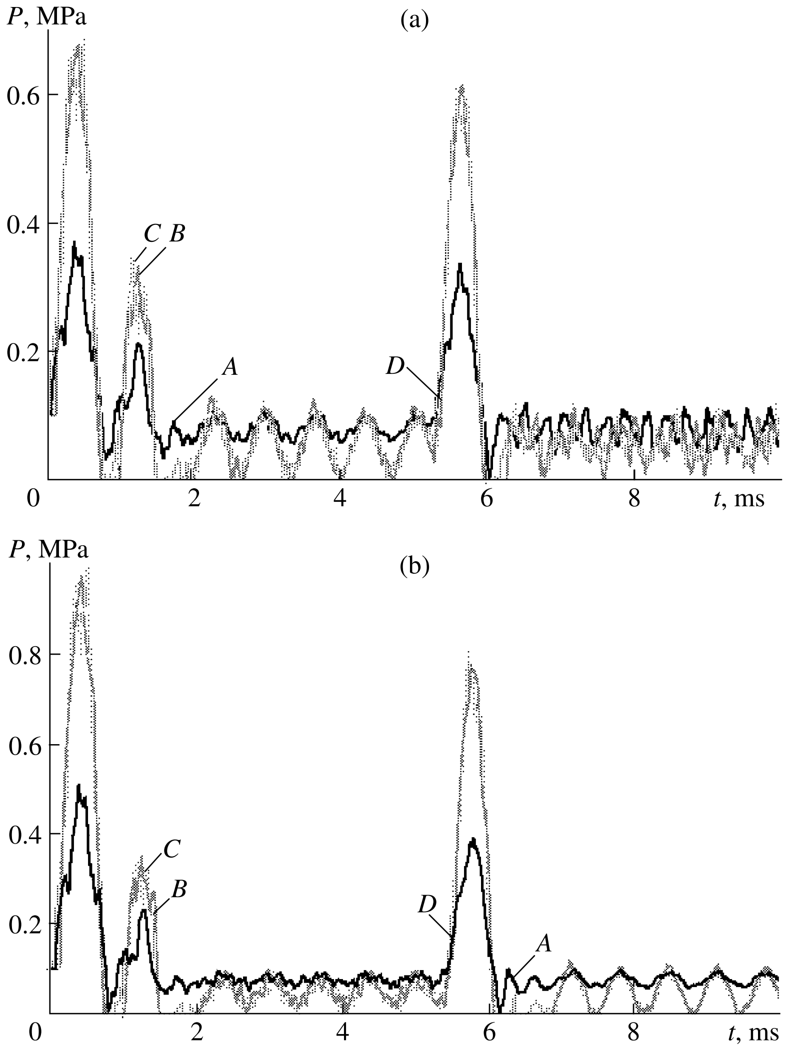

**Fig. 3.** Dependence of pressure on time in melt during EHPT in ladle: (a) treatment without waveguide attachment; (b) treatment by waveguide attachment with diameter of 30 mm; (c) treatment by waveguide attachment with diameter of 50 mm; (d) treatment by waveguide attachment with diameter of 70 mm.

On the basis of a numerical solution of Eqs. (1) and (2), the pressure dependences on time in the liquid metal at various points of the ladle are calculated (see Fig. 1). The varied parameter is the waveguide attachment diameter $d_a$.

The wave equation (1) was solved by the finite-difference method according to the explicit "cross" three-layer scheme.

## DISCUSSION OF RESULTS

The results of numerical modeling are presented in Fig. 3 in the form of graphical dependences of the pressure magnitude on time for three values of $d_a$, as well as for the waveguide lacking the attachment at preset points of the ladle (see Fig. 1). Point $A$ is located at a distance of $d_a/4$ from the symmetry axis of the ladle ($z$ axis) and at the depth of $h_{im}/2$.The location of point $D$ along the $z$ axis corresponds to the coordinate $(h_m - h_{im})/2$.The calculations are performed for Al melt, and the correlations of rigidity of the resilient elements and the membrane are $k_1/k_2 = 0.1$. The ladle is a cylindrical container with a diameter of 1 m equal to its height. The immersion depth of the waveguide equals half the height of the ladle. Sound velocity $c_0$ in the Al melt is taken to be equal to 4700 m/s, and its density $\rho_0$ is 2385 kg/m$^3$.

The analysis of the obtained results shows that the pressure in the melt is a sequence of pulses. At points $C$ and $D$, these pulses have two pronounced maxima, with the second maximum of the first pulse exceeding the first one. Point $B$ is characterized by one maximum. The pressure at point $A$ is almost two times lower than at other points, and the first pulse has four maxima. In between the pulses, the pressure of the liquid metal drops below atmospheric pressure and at certain moments of time it may be almost zero; i.e., cavitation

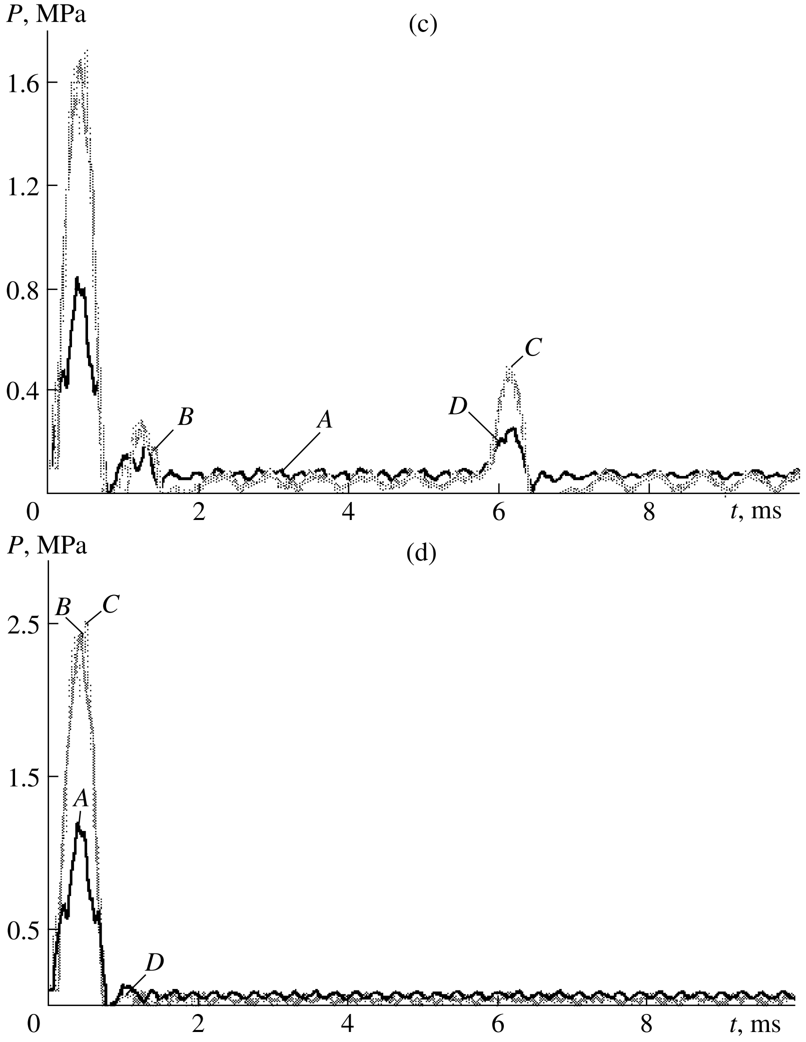

**Fig. 3.** Contd.

actually occurs over the entire volume of the ladle. The presence of the waveguide attachments increases the pressure levels at the initial stage of treatment. With an increase in the attachment diameter, e.g., from 30 to 70 mm, the pressure at point *C* at the first maximum increases from 1 to 2.5 MPa. With subsequent pulses, the pressure levels decline, which is indicative of a significant share of the energy of dissipation during the process of treatment of the waveguide attachments. Thus, for a waveguide 70 mm in diameter at a preset time interval, the second pulse completely fails to be registered. The cavitation processes at the examined points of the ladle seem to be different as well. At point *A*, the pressure drops to zero only at the end of the pressure pulse; during the rest of the time, the levels of pressure insignificantly differ from atmospheric pressure.

In an acoustic medium, the energy transfer is characterized by the energy flux. For characteristics of the energy transfer direction at a certain point of the wave field of the medium, a vector value (energy flux density) is used. The absolute value of this magnitude by the moment of time *t* for the pressure wave can be defined by the formula of [7]:

$$W_t = \frac{1}{\rho_0 c_0}\int_0^t P^2(t)dt.$$

On the basis of the obtained dependences of $P(t)$ (see Fig. 3), let us estimate the values of $W_t$ by the moment of time $t = 10$ ms both for the case of the waveguide attachment application and without it at specified points of the ladle. The results of the estimation are presented in Fig. 4 in the form of a graphical dependence of relative values of $W_a/W_w$ and $d_a/d_w$ where $W_a$ and $W_w$ are the flux density at a preset point of the ladle with application of a waveguide and without it, respectively; $d_a$ is the waveguide attachment diameter; and $d_w$ is the waveguide diameter ($d_w = 20$ mm). The value of $W_a/W_w$ varies proportionally to the value of $d_a/d_w$; e.g., for the points *B*, *C*, and *D* with application of an attachment with a diameter

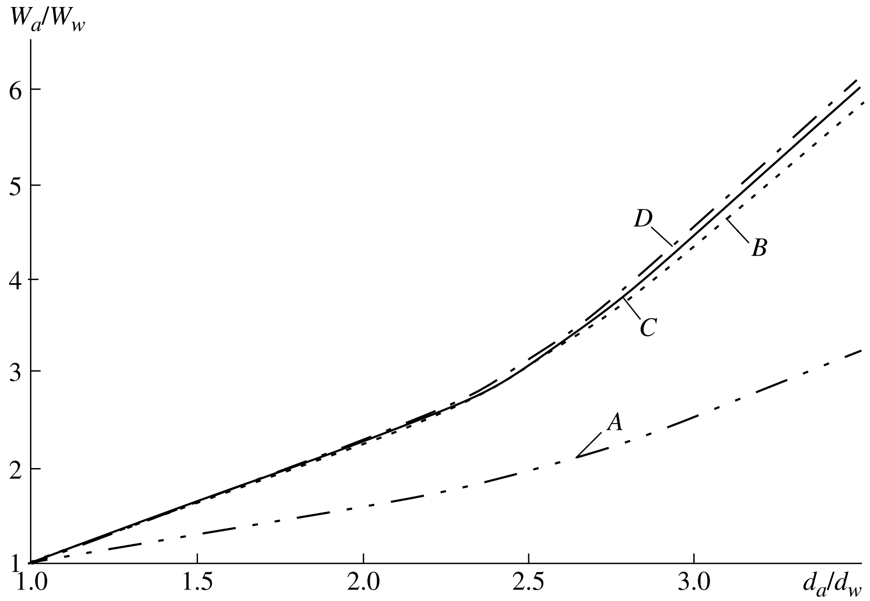

**Fig. 4.** Dependence of the energy flux density on the attachment diameter at preset points of the ladle during EHPT of the melt.

of 50 mm, the value of $W_a$ exceeds that of $W_w$ by approximately a factor of 3. With the attachment diameter increase up to 70 mm, $W_a$ grows already with respect to $W_w$ by approximately a factor of 6. For point A, this tendency occurs to a lesser degree.

In the first part of [5], it has been shown that the attachment application allows for a more intense damping of the waveguide vibrations in the melt and, hence, provides an increase in the share of dissipated energy. This fact is confirmed by the obtained results; i.e., the waveguide attachments significantly increase the energy transferred to the melt and, consequently, one of its constituents–the energy of dissipation.

Let us analyze the influence of the waveguides on the processes of cavitation in the melt. As an indicator of the effective treatment, the overall duration of cavitation occurrence (i.e., the total time during which the pressure in the melt approaches zero) is accepted. Using the dependences $P(t)$ (see Fig. 3), we find the relative time of cavitation occurrence $t_c/t$ (ratio of duration of cavitation occurrence $t_c$ to the overall duration of the process of pressure wave propagation $t$). The values of $t_c/t$ at specified points of the ladle with respect to diameter of the waveguide attachment are presented in the table.

Relative time of cavitation occurrence $t_l/t$ in the melt

| Point of the ladle | $d_a/d_w$ | | | |
|---|---|---|---|---|
| | 1 | 1.5 | 2.5 | 3.5 |
| *A* | 0 | 0 | 0.0044 | 0.0056 |
| *B* | 0.1137 | 0.1691 | 0.1428 | 0.0677 |
| *C* | 0.1092 | 0.1785 | 0.16 | 0.054 |
| *D* | 0.0444 | 0.0681 | 0.073 | 0.012 |

The process of occurrence and development of cavitation can be determined both by the zone of the melt treatment in the ladle and the diameter of the waveguide attachment. For point *A* located in the upper region of the ladle, cavitation occurs only at a ratio of $d_a/d_w \geq 2.5$. In the zones of treatment below the waveguide (points *B*, *C*, *D*), the application of a 30 mm attachment allows for the value of $t_c/t$ to be increased by about one and a half times. At $d_a$ enlargement up to 50 mm, the value of $t_c/t$ at points *B* and *C* somewhat decreases, and at point *D*, it increases. The treatment by means of an attachment with a diameter of 70 mm results in a considerable reduction of $t_c/t$ in the lower zone of the ladle below the waveguide in comparison with treatment without the attachment, which is indicative of the functional capacity limitation of treatment at a further increase in the attachment diameter.

In [8], it is shown that the main factors of effective influence on the melt are the geometrical parameters of the working space of the vessel, the plunger-vibrator, and the gap between them. Therefore, in the process of designing technological EHPT devices with respect to the required parameters of treatment, it is necessary to consider the correlation of the geometrical dimensions as well as the configuration of the EDGRV working element and ladle.

Thus, the presence of waveguide attachments results in a significant increase in pressure at the initial stage of treatment and in the share of dissipated energy in the melt and duration of cavitation occurrence.

## CONCLUSIONS

(1) Application of waveguide attachments allows for a significant increase in the pressure levels in the melt, but only at the initial stage of the treatment.

(2) With an increase in diameter of the waveguide attachments, the share of dissipated energy in the melt grows, which leads to interior structural kinetic changes in the liquid metal.

(3) The duration of cavitation processes in the melt depends on the geometrical characteristics of the wave-radiation system and the zone of treatment.

(4) The efficiency of EHPT of the melt is stipulated by the correlation of the geometrical dimensions, as well as the configuration of the EDGVR working element and ladle.

## REFERENCES

1. Tsurkin, V.N., and Mel'nik, A.V., System Analysis of the Factors Stabilizing the Parameters of Loading the Electrohydropulse Treatment of Melt, Surf. Eng. Appl. Electrochem., 2007, no. 2(244), pp. 52–59.
2. Tsurkin, V.N., Grabovyi, V.M. and Sinchuk, A.V., The Functional Possibilities of the Electrohydropulse Processing of the Melt in a Ladle, *Surf. Eng. Appl. Electrochem.*, 2006, no. 5, pp. 55–61.
3. Pozdeev, V.A., Tsarenko, P.I., Butakov, B.I. and Malyushevskii, P.P., Elektrorazryadnye generatory uprugikh kolebanii (Electric Discharge Generators of Resilient Vibrations), Kiev: Naukova dumka, 1985.
4. Galiev, Sh.U., Barbashova, G.A., Bilyanskii, Yu.S., Zhirnov, M.V. and Kosenkov, V.M., The Interaction of the Electric Discharge Generator of Vibrations with Liquid Metal in a Ladle, Problemy Prochnosti, 1991, no. 11, pp. 78–82.
5. Tsurkin, V.N., and Mel'nik, A.V., Processes and Character of Melt Loading by Electrodischarge Generator of Vibrations on Resilient Elements. Part I. (Waveguide dynamics), Surf. Eng. Appl. Electrohem., 2008, no.4(252), pp. 82–92.
6. Galiev, Sh.U., Nelineinye volny in ogranichnnykh sploshnykh sredakh (Non-Linear Waves in Limited Solid Media), Kiev: Naukova dumka, 1988.
7. Krivitskii, E.V., and Shamko, V.V., Perehodnye protsessy pri vysokovol'tnom razryade v vode (Transient Phenomena at High Voltage Discharge in Water), Kiev: Naukova dumka, 1979.
8. Ignat'ev, I.E., Kiselev, A.V., Dolmatov, A.V., et al. Mathematical Modelling of Liquid Motion Induced by Plunger-Vibrator in a Cylindrical Vessel, Melts, 2005, no. 6, pp. 3–11.

*ISSN 1068-3755, Surface Engineering and Applied Electrochemistry, 2009, Vol. 45, No. 5, pp. 430–432. © Allerton Press, Inc., 2009.*
*Original Russian Text © T.A. Manko, 2009, published in Elektronnaya Obrabotka Materialov, 2009, No. 5, pp. 97–99.*

## OPERATING EXPERIENCE

# Infrared Radiation Use in Formation of Constructions from Fiberglass Materials

**T. A. Manko**
*Dnepropetrovsk State University, Nauchnyi per. 13, Dnepropetrovsk, 49050 Ukraine*
*e-mail: naza@ua.fm*

Received August 5, 2009

**Abstract**—Results of research into the formation of coiled products made from fiberglass materials using infrared radiation are presented. The efficiency of the infrared method of heating is shown.

**DOI:** 10.3103/S1068375509050160

Existing techniques of manufacturing constructions from fiberglass materials on the basis of thermojet binding include long lasting curing of the generated products in furnaces with convective means of heat transfer. Recently, processes of accelerated curing with application of nonconventional methods of heating based on use of currents of high frequency and processes of radiation curing with the usage of a stream of accelerated electrons and infrared radiation have been intensively investigated. At high-frequency heating, internal warming up of the material occurs; the heating rate does not depend on the heat conductivity and dimensions but is defined by supplied specific capacity. This allows the process of curing to be accelerated considerably; however, it leads to an appreciable decrease in interbranch durability of fiberglass materials [1]. In radiation curing by accelerated electrons, the curing time of fiberglass materials is reduced by tens of times at the curing stage, comparable with what is obtained according to current technology. Noting the prospects for applying electronic curing in manufacturing fiberglass materials, one should emphasize that analysis of the feasibility of using the given method is necessary in each specific case because of the high cost of equipment.

The most universal and technically comparatively easily implemented way is the method of infrared heating. The relative simplicity and low cost of infrared radiators and the possibility creating considerable specific radiation capacities in a blanket at high efficiency allow it to be used effectively for accelerated curing [2].

With reference to practical realization of the method for manufacturing coiled products from fiberglass, we studied the possibility of using infrared heating in level-by-level formation of a shell construction with subsequent curing by way of concentrated locally consecutive supply of energy. As objects of research, materials having various strength and thermophysical characteristics were chosen: silica material CAT-11-maintenance A, LOG strap from aluminoborosilicate material, and polycondensation and polymerizing bindings LBS-4 and Electronic Data Interchange, respectively.

In investigation of processes that occur upon infrared heating in binding and fiberglass materials on their basis, infrared spectroscopy and X-ray structure analysis were applied, and interbranch durability on shift, density, and degree of curing was determined. Spectroscopic investigations were conducted on a SPECORD spectrometer, radiographic investigations were conducted on a DRON-3 X-ray diffraction meter, and strength tests were performed on a MR-05-1 tension testing machine at a loading speed of $8 \times 10^5$ m/s.

The comparative analysis of infrared spectra of uncured and cured bindings allows one to assert that, under infrared irradiation and convection heating, the reactions of curing are the same. This leads to obtainment of materials with identical structure, which is corroborated by data of radiographic investigations.

An important condition of creating a strong construction from fiberglass materials is carrying out curing according to optimum modes. Modes of curing were chosen on the basis of study of the dependence of interbranch durability on shift of microplastic samples on temperature $T$ and time $t$ of infrared heating. According to the results of tests, graphs of change in average values of forces $P$ of rupture versus parameters of infrared heating of fiberglass on the basis of binding LBS-4 (Fig. 1) and fiberglass on the basis of binding Electronic Data Interchange (Fig. 2) are constructed. Data are averaged by test results of ten samples.

From analysis of data cited in Figs. 1 and 2, it follows that the greatest interbranch fiberglass durability on the basis of binding LBS-4 is assured by carrying out curing at a temperature of 430 K for 0.5 h, and for fiberglass on the basis of binding Electronic Data Interchange, at a temperature of 440K for 1.5 h.

Comparison of the test results of samples cured in a furnace using the convection method of heat transfer according to modes of operating technology and infra-

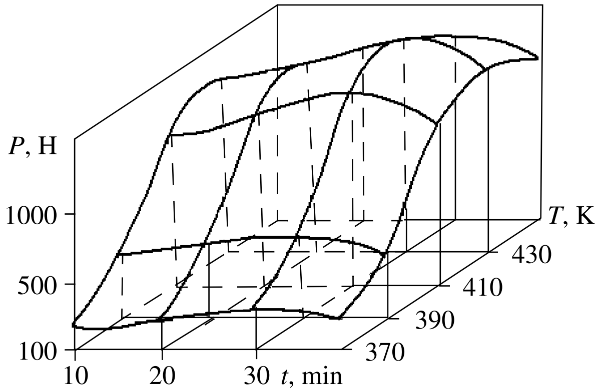

**Fig. 1.**

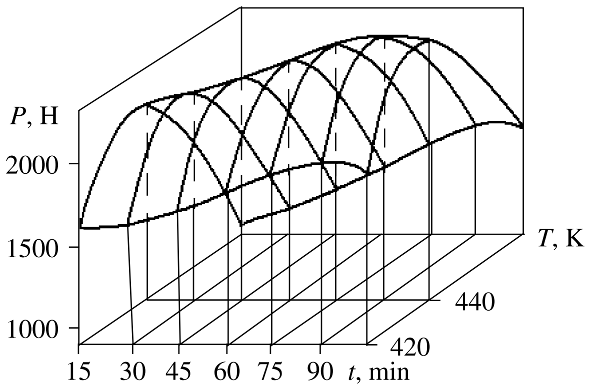

**Fig. 2.**

red heating has shown that the local infrared irradiation allows one to reduce the curing time considerably in preserving the values of interbranch durability. Acceleration of curing occurs at the expense of creating high radiation rates in a material layer and deeper influence on molecular structure. Under the action of radiation with a frequency close to frequencies of characteristic fluctuations of atoms, the induced fluctuations increase; thus, the factor of absorption of energy of radiation increases.

The chosen modes were used in manufacturing thin-walled (1.5–2 mm) glass and plastic covers with local curing by infrared heating. Covers were cast at the plant for manufacturing microplastics by winding on a cylindrical arbor 215 mm in diameter at a speed of rotation of the arbor of 0.13 rps. At the first stage, irradiation at level-by-level formation of a cover was performed, at the second stage, rotation of the formed cover in a field of infrared radiators was carried out before curing. Control products after winding were cured in the furnace with the convection method of heat transfer. The results of physicomechanical tests of the samples obtained from these covers and the modes of curing are presented in the table.

These experimental investigations showed the possibility of applying local infrared heating for obtaining coiled products from fiberglass materials on the basis of thermojet binding with a fairly high degree of curing (94.0–97.2%) at a considerable reduction of manufacturing time (by 3–4 times).

Uncured bindings have a high factor of infrared radiation absorption, which leads to fast heating. This is a property of bindings, and also creation of favorable conditions for escape of volatile components at level-by-level formation and large specific capacities of radiation in layers being coiled allows one to use infrared heating in the course of winding effectively. At layer-by-layer and consecutive formation with application of infrared heating, each subsequent layer is laid down on a partially cured preceding one, additional curing of which occurs after irradiation of the subsequent ones. Thus curing of the inside layers comes as a result of heat transfer from the metal arbor. Thanks to the large density of the energy stream created in the product, the temperature of the last one rises much more intensely than in convection heating. The difference of temperatures of the internal and external surfaces of the cover is reduced, and the polymerization process occurs simultaneously on the entire mass of material.

**Table**

| Binding | Heating structure | Curing mode | | Density, kg/dm$^3$ | Degree of curing, % |
|---|---|---|---|---|---|
| | | Temperature, K | Time, h | | |
| LBS-4 | Infrared | 433 | 1.5 | 1.48 | 97.2 |
| | Convection | (293–433) | 6 | 1.43 | 98.3 |
| | | 433 | 1 | | |
| Electronic Data Interchange | Infrared | 443 | 4.5 | 1.65 | 94.0 |
| | Convection | 363 | 3 | | |
| | | 393 | 3.5 | | |
| | | 423 | 1 | | |
| | | 443 | 2 | 1.65 | 96.0 |

The investigations of accelerated curing of bindings in fiberglass materials with application of infrared heating allow the following conclusions to be drawn:

(1) Use of infrared radiation is effective in the process of winding products of fiberglass materials owing to high absorbing ability of uncured binding, with the possibility of creating considerable specific capacities of radiation in layers being coiled and improvement of conditions of escape of binding volatiles.

(2) Acceleration of curing of fiberglass materials on the basis of thermojet binding upon local infrared heating occurs at the expense of a deep influence on molecular structure of the material, causing an increase in the factor of absorption of infrared radiation.

(3) Upon curing of a wound construction with infrared irradiation, stationary heat exchange comes much faster than under convection heating.

According to results of investigations, a facility for layer-by-layer and consecutive formation of products of fiberglass materials with application of local infrared heating is developed.

## REFERENCES

1. Borhert, R., Yubits, V., *Tehnika infrakrasnogo nagreva* Moscow, Leningrad: Gosenergoizdat, 1963. p. 278.
2. Fedorova I.G., (Application of high-frequency heating at pipes manufacturing from fiberglass) *Plasticheskie massy*, 1961, no. 1. p. 35–37.

ISSN 1068-3755, Surface Engineering and Applied Electrochemistry, 2009, Vol. 45, No. 5, pp. 433–436. © Allerton Press, Inc., 2009.
Original Russian Text © P.I. Baranskii, G.P. Gaidar, A.V. Fedosov, 2009, published in Elektronnaya Obrabotka Materialov, 2009, No. 5, pp. 100–104.

## OPERATING EXPERIENCE

# Magnetic Storms, Long-Term Space Flights, and Aircraft Crashes

**P. I. Baranskii**[a], **G. P. Gaidar**[b], **and A. V. Fedosov**[c]

[a]*V. Lashkarev Institute of Semiconductor Physics, National Academy of Sciences of Ukraine, pr. Nauki 41, Kiev, 03680 Ukraine*
[b]*Institute of Nuclear Studies, National Academy of Sciences of Ukraine, pr. Nauki 47, Kiev, 03680 Ukraine*
*e-mail: gaidar@kinr.kiev.ua*
[c]*Lutsk National Technical University, ul. Lvovskaya 75, Lutsk, 43018 Ukraine*

Received June 20, 2009

**Abstract**—The familiar aircraft crashes that occurred during the last 15 years were divided by the authors into two groups: (1) those due to technical failures of the aircraft, and (2) those having resulted from aircraft collisions. Supposedly, the crashes in the second case are caused by humans. Taking into account the well documented correlation between severe traffic accidents (with lethal outcomes) and magnetic storms, it can be conjectured that, provided that the assumption made is correct, the aircraft crashes in the second group will cluster in the time domain of high solar activity in dependence on the Wolff index versus the time $W = W(t)$, while the aircraft crashes in the first group will be uniformly distributed over the time scale; i.e., they will also have occurred in the regions of $W(t)$ minima. Precisely this hypothesis is confirmed by the data presented by the authors. A 15-year time period was already sufficient to acquire enough statistical material concerning the crashes, and so the large differences in the flying-performance characteristics and technical parameters of the aircraft are of little importance.

**DOI:** 10.3103/S1068375509050172

The nature of magnetic storms (MSs) is described extensively in a number of scientific papers and monographs (see, e.g., [1–3]), so it will not be pursued here. The influence of MSs associated with the effects of solar activity on biologic (including human) objects was first studied by A.L. Chizhevskii, who is the commonly recognized founder of heliobiology, in his pioneering works [4–6]. The problems that would appear due to changes of the magnetic situation and cosmic ray effects in the practical implementation of a long-term flight of American astronauts to Mars (to be launched in 2014) were discussed in [7] in length.

Possessing reliable data (obtained with the help of the modern methods of physical study) about the influence of extremely low-intensity magnetic fields (MFs), both constant [8] and alternating [9], and considering the very high sensitivity of the human central nervous system (CNS) to alternating magnetic fields of very low intensity [10] (characteristic for MSs of ~300–500 $\gamma$, where $1 \times \gamma = 10^{-9}$ tesla), the authors of works [11, 12] (echoing national [13] and Japanese [14] researchers) revealed the complete correlation between MS events and traffic accidents (TAs) with lethal outcomes.

In addition to the above-mentioned MS–TA correlations, of note is the rich evidence available from medical research institutions and the physicians of many therapeutic institutions that constant MFs and electromagnetic waves in a broad frequency range (from 1–10 Hz to the SHF millimeter range with $\nu \sim 10^{10}$–$10^{11}$ Hz) influence the cardiovascular system [15–17] and the very blood of humans [15, 17–19]. There was also studied the nonthermal therapeutic effect of electromagnetic fields in a wide frequency range [20–23] on living organisms, whose possible mechanism was discussed in [24]. The literature contains a quite detailed overview of the works devoted to the study of the problem under discussion here [25].

This report elucidates the relation between the MSs and familiar aircraft crashes that occurred during 1988–2002 in different countries around the world (and even on different continents).

The 15-year time interval chosen for the analysis contained two maxima of solar activity (with a minimum in between; see Fig. 1) and was not too large for the aircraft to differ drastically in their construction features and in the strength characteristics of the materials they were made from.

All the analyzed aircraft crashes were divided into two notably distinct groups. The crashes in the first group were due to technical failures of the aircraft, consequently; they, naturally, could depend neither on the MSs nor on any other external factors. They include the following incidents: June 27, 1988, France, Airbus A320 Plane Crash; September 9, 1990, 60 km away

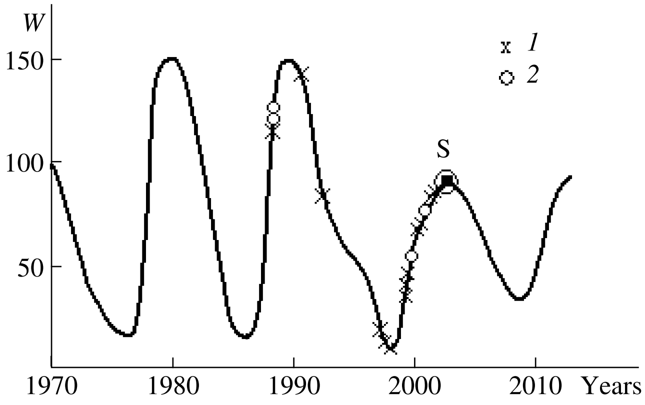

**Fig. 1.** The time dependence of the Wolf index as an indicator of the solar activity (solid line), the aircraft crashes associated with technical failures (group *1*, crosses), the aircraft collisions (air crash group *2*, open circles), and the Sknilov air crash (the symbol S).

from Venice, Su-27; June 28, 1992, Omsk, Yak-52; June 3, 1997, Colorado, A-86; July 26, 1997, Belgium, Ostende airport, X-T-300; September 1997, Baltimore, F-117A Nighthawk; May 30, 1999, Australia, single-engine aircraft; June 6, 1999, Bratislava (Slovakia), Hawk 200; September 18, 1999, Ermelo Airport (Republic of South Africa); March 19, 2000, Kingsville, Texas, F-16; June 18, 2000, Willow Grow, Pennsylvania, F-14 Tomcat; June 3, 2001, Bremen, Kent, Great Britain, King Kobra; July 17, 2001, near Pskov, Su-33; April 20, 2002, near Point Mugu, California, OF-4. These crashes, which are denoted by crosses, are arranged quite uniformly along the $W = W(t)$ curve both in terms of the position of the maxima and the position of the minimum (Fig. 1).

The second group of crashes includes in-flight collisions of two (or more) aircraft. On August 28, 1988, in the Federal Republic of Germany, three aircraft collided, while two-aircraft collisions took place on April 19, 1998, near Kissimmee, Florida; on July 29, 1999, in Oshkosh, Wisconsin; and on June 10, 2001, in Levashovo aerodrome in the Saint Petersburg suburbs.

The discrimination of the aircraft collisions into a separate crash group was motivated by the well-established correlation of TAs with magnetic storms (i.e., with $W$). In addition, because the basis of this correlation is the certain MS-induced delay of the pilot's responses, it can be expected that the simultaneous exposure of the regulatory system (and central nervous system as a whole) of the pilots flying two (or three) aircraft to this factor (i.e., MSs) will lead to an increase of the collision probability. This is why the open circles superimposed on the $W(t)$ curve in Fig. 1 (and arranged along the X-axis in accordance with the aircraft crash dates) are well away from the minima of the $W(t)$ curve and correspond to elevated $W$ values. This just supports the above hypothesis that MSs affected the aircraft crashes involving collisions.

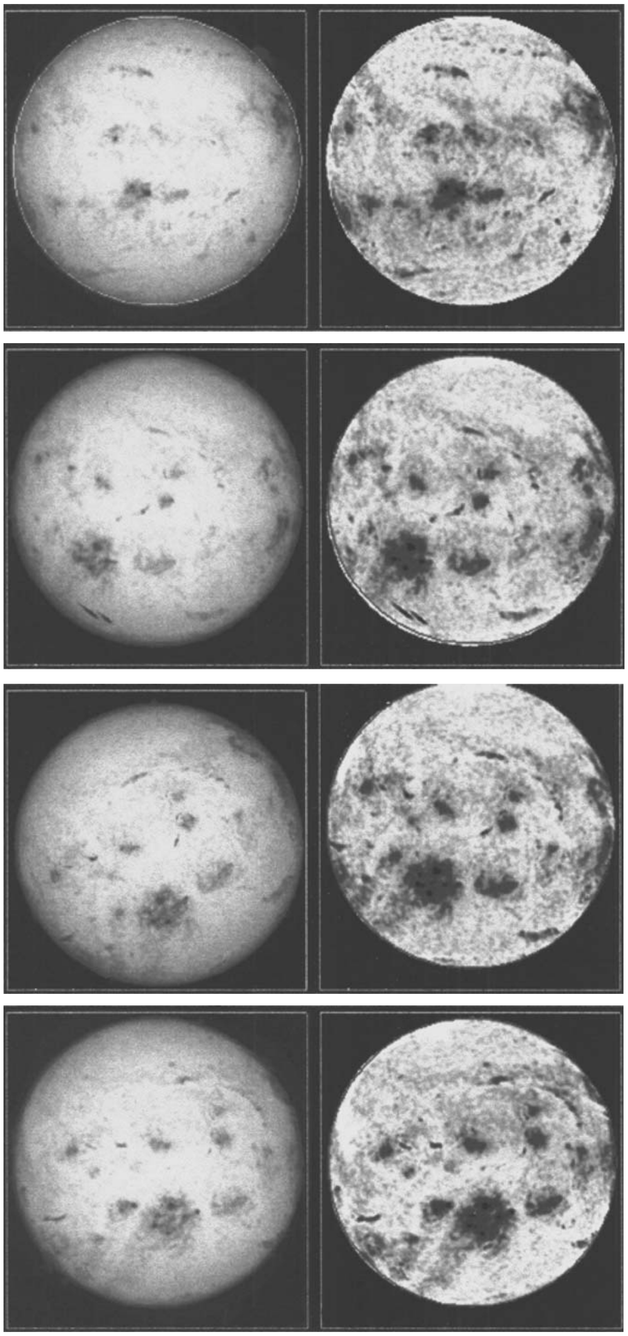

**Fig. 2.** Image of the solar disk (in different spectral ranges) in the period from July 21, 2002 to July 28, 2002 (according to the Crimean Astrophysical Observatory data).

Of special note is the terrible aircraft crash that occurred on July 27, 2002 (at approximately 12:52 Kiev local time) during an air show in honor of Aviation Day at the Sknilov aerodrome near Lvov in Ukraine. A Ukrainian Air Force Su-27 performing an advanced maneuver plunged into the crowd of air show spectators.

Actually, in the context of the classification adopted by us, this aircraft crash can neither be referred to the first (for the aircraft was permitted by the technical inspector to perform demonstration flights) nor to the second group (for it collided not with another aircraft but rather with the ground).

However, of note is the very serious circumstance that this aircraft crash is coincident in time with the maxima of solar activity and, hence, with a *W* maximum not only on the months scale but also in full agreement with the diurnal increases of the sunspot (the inevitable concomitant of solar protuberances) density (SSD). In addition, in accordance with the Crimean Astrophysical Observatory data (accessible via the Internet), for a few days preceding the Sknilov aircraft crash, the SSD had stably increased (see Fig. 2).

Furthermore, if the organizers of this show are judicious, besides all the other things they take into account, they should consult with astrophysics about when is the most safe calendar time for the demonstration of advanced maneuvers (known to produce great overloading of all the regulatory systems of the human body, causing one to become extremely sensitive to trace abnormalities in the environmental characteristics). If they had done so, they would have been given the dates indicated by the vertical arrows in Fig. 1.

Then, on account of the results of the studies of the MS effect on TAs, which have been well known since 1971 [2, 10–12, 14], this scheduled air show would be much more likely to proceed without a crash and human losses, and the pilots (who seemed to have been saved by a miracle) would avoid possibly having to suffer criminal proceedings, which is not very deserved in view of the above mentioned.

Naturally, when grieving about the 2002 Sknilov disaster, we can now change nothing. However, the future preparations for aircraft (spacecraft) holidays and demonstration flights should take into consideration absolutely all the deep scientific knowledge and rich experience gained from the exploitation of modern technical devices.

## REFERENCES

1. Pochtarev, V.I., *Magnetizm zemli i kosmicheskogo prostranstva* (Magnetism of Earth and Cosmic Space), Moscow: Nauka, 1966.
2. *Vliyanie solnechnoi aktivnosti na atmospferu i biosferu zemli* (Effect of Solar Activity on the Atmosphere and Biosphere of Earth), Collected papers, Gnevyshev, M.N., Ol, A.I., Eds., Moscow: Nauka, 1971.
3. *Elektromagnitnye polya v biosfere* (Electromagnetic Fields in the Biosphere), Collected papers, Krasnogorskay, N.V., Ed., Moscow: Nauka, 1984, vols. 1 and 2.
4. Chizhevskii, A.L., *Fizicheskie factory istoricheskogo protcessa* (Physical Factors of Historic Process), Kaluga: Pervaya Gostipografiya, 1924.
5. Chizhevskii, A.L., and Shishina, Yu.G., *V ritme Solntca* (At Solar Rhythm), Moscow: Nauka, 1969.
6. Chizhevskii, A.L., *Kosmicheskii puls zhemli. Zemlya v obyatiyakh Solntsa* (Cosmic Pulse of Earth, Earth in Embraces of Sun), Geliotaraksiya, Moscow: Mysl, 1995.
7. Baranskii, P.I., Vegner, E.F., and Gaidar, O.V., Problems Associated with Long-Term Stay of Manned Spacecrafts in Cosmic Space, *Kosmichna Nauka i Tekhnologia*, 2002, vol. 8, no. 4, pp. 86–95.
8. Baranskii, P.I., and Mishchenko, L.T., Change Electron Spin Resonance Spectra in Resting Seeds of Certain Agricultural Plants Exposed to Constant External Magnetic Fields, Dokl. Akad. Nauk Ukrainian Soviet Socialist Republic, 1979, no. 10, ser. B, pp. 843–845.
9. Mikhailovskii, V.M., Krasnogorskii, M.M., Voichishin, K.S., Grabar, L.I., and Zhegar, V.M., On Perception by Humans of Weak Magnetic Fields, Dop. Akad. Nauk URSR, 1969. vol. 106, no. 10, ser. B, pp. 929–934.
10. Kholodov, Yu.A., Brain in Electromagnetic Fields, Moscow: Nauka, 1982.
11. Baranskii, P.I., Venger, E.F., and Gaidar, O.V., Effect of Solar-Terrestrial Relations on Human Regulatory System and Accident State in Highways, Dopovidi Natsionalnoi Akad. Nauk Ukrainy, 1999, no. 8, pp. 176–179.
12. Baranskii, P.I., Venger, E.F, Gaidar, O.V., and Zabudskii, T.A, Effect of Solar Activity (Geomagnetic Storms) on Human Regulatory Systems and Adequacy of his Behavior in Stress Situations on the Earth and in Space, Elektronnaya Obrabotka Materialov, 2004, no. 5, pp. 65–69.
13. Romanchuk, P.R., Effect of Solar Activity on Traffic Accidents, Avtoshlyakhovik Ukraini, 1999, no. 1, p. 27.
14. Masamura, Sh., *Silny effect solnechnoi aktivnosti v dorozhnykh proisshestviyakh. In: Vliyanie solnechnoi aktivnosti na atmosferu i biosferu zemli* (Strong Effect of Solar Activity in Traffic Accidents. In: Effect of Solar Activity on the Earth's Atmosphere and Biosphere). Collected papers, Gnevysheva, M.N., and Ol, A.I., Eds., Moscow: Nauka, 1971, pp. 209–210.
15. *Vliyanie magnitnykh polei na biologicheskie obyekty* (Effect of Magnetic Fields on Biologic Objects), Proceedings of third All-Union symposium. July 17-19, 1975, Kaliningrad: Kaliningrad State University, 1975.
16. Vladimirskii, B.M., *O vozmozhnykh faktorakh solnechnoi aktivnosti, vliyayushchikh na processy v biosfere. In: Vliyanie solnechnoi aktivnosti na atmosferu i biosferu zemli* (On Possible Factors of Solar Activity Influencing the Biospheric Processes. In: Effect of Solar Activity on the Earth's Atmosphere and Biosphere). Collected papers, Gnevysheva, M.N., and Ol, A.I., Eds., Moscow: Nauka, 1971, pp. 126–141.
17. Kholodov, Yu.A., *Magnetism v biologii* (Magnetism in Biology), Moscow: Nauka, 1970.
18. Shults, N., *Solntse i krov* (Sun and Blood), Znanie – Sila, 1967, p. 17.
19. Chizhevskii, A.L., *Elektricheskie i magnitnye svoistva eritrotsitov* (Electric and Magnetic Properties of Erythrocytes), Kiev: Naukova Dumka, 1973.
20. Desyatkov, N.D., Influence of Electromagnetic Radiation in Millimeter Wavelength Range on Biologic Objects, Uspekhi Fiz. Nauk, 1973, vol. 109, no. 3, pp. 453–454.

21. Gaiduk, V.I., Khurgin, Yu.I., and Kudryashova, V.A., Prospects of Study of Mechanisms of Non-Thermal Effect of Electromagnetic Radiation in Millimeter and Sub-Millimeter Range on Biologically Active Compounds, Uspekhi Fiz. Nauk, 1973, vol. 109, no. 3, pp. 466–468.
22. *Fundamentalnye i prikladnye aspekty primeneniya millimetrovogo elektromagnitnogo izlucheniya v meditsine* (Basic and Applied Aspects of Use of Millimeter-Range Electromagnetic Radiation in Medicine), Abstracts of first All-Union symposium with international contributrers, Kiev, May 10–13, 1989.
23. Certificate of authorship no. 733697 of May 15, 1980 (USSR). *Sposob lecheniya povrezhdennykh biologicheskikh tkanei* (Method of Treatment of Damaged Biologic Tissues), Cherkasov, I.S., and Nedvzetskii, S.V., Published in Bul.: Discoveries, Inventions, no. 18, 1980.
24. Sitko, S.P., and Sugakov, V.I., On the Role of Spin States of Albuminous Molecules, Dokl. Akad. Nauk of Ukrainian Soviet Socialist Republic, 1984, Ser. A, no. 6, pp. 65–67.
25. Bingi, V.N., and Savin A.V., Physical Problems of Effect of Weak Magnetic Fields on Biologic Objects, Uspekhi Fiz. Nauk, 2003, vol. 173, no. 3, pp. 265–300.

ISSN 1068-3755, Surface Engineering and Applied Electrochemistry, 2009, Vol. 45, No. 5, pp. 437–440. © Allerton Press, Inc., 2009.
Original Russian Text © A.M. Magerramov, M.A. Nuriev, F.I. Akhmedov, I.M. Ismailov, 2009, published in Elektronnaya Obrabotka Materialov, 2009, No. 5, pp. 105–108.

## OPERATING EXPERIENCE

# Radiothermoluminescence of γ-Irradiated Composites of Polypropilene and Dispersed Oxides

**A. M. Magerramov, M. A. Nuriev, F. I. Akhmedov, and I. M. Ismailov**
*Institute of Radiation Problems, National Academy of Sciences of Azerbaijan, ul. F. Agaeva 9, Baku, Az-1143 Azerbaijan*
*e-mail: musa_nuriev@mail.ru*

Received June 30, 2009

**Abstract**—The peculiarities of stabilization of the excess charges in composites based on PP and dispersed metal oxides are investigated using the method of radiothermoluminescence (RTL). It is shown that introduction of fillers such as BeO and $ZrO_2$ into PP leads to change in the intensity and temperature of realization of the $\beta_1$, β, α, and $\alpha_1$ peaks on the RTL curves, and this can be used to predict the electroactive, dielectric and physical mechanical properties of the composites based on them.

**DOI:** 10.3103/S1068375509050184

## INTRODUCTION

Studying the radiation modification of polymer materials and products is of great interest for the electronics, cable, and electromechanical industry. Certain requirements such as radiation and heat resistance, low dielectric loss, and the like [1, 2] are imposed on these materials. Radiation exposure does not always lead to deterioration of some properties of polymer materials [1–3]. Radiation-cross-linked polyolefins have found application in cable engineering. No less important are the problems of radiation modification of composite materials based on polymers dispersed with the oxides BeO, $ZrO_2$, and $TiO_2$ and aerosil A-380 [1–3, 6, 7]. Studying the peculiarities of charge stabilization and interphase and polarization phenomena in these composite materials is also of current concern for prediction of their operating properties. Using different fillers like alundum A, muscovite, and so on, composite polymer materials with stable dielectric parameters and moisture resistance under UHF fields up to $10^{10}$ Hz [4] were obtained. It should be noted that the effectiveness of the influence of fine-dispersed fillers from these metal oxides on polypropylene (PP) or other polyolefins substantially depends also on the crystallization conditions and method of composite production (extrusion, pressing). The compositions obtained under conditions of deep hardening of the melt at $T = 273$ K have more homogeneous structure [4–6, 19] and are easily processed, and they are distinguished by mechanical [1–3, 10] and electric strength [19].

No less important is the problem of prediction of the degree of radiation-induced alteration of polymer structure and properties. For these purposes, the method of radiothermoluminescence (RTL) is widely used [6]. From the RTL photon emission curves and β-peak positions (beginning of the devitrification temperatures) of filled polymers, the degree of influence of electrons and γ irradiation on a polymer structure can be judged.

The goal of the present work is to investigate the radiation resistance and peculiarities of stabilization of the excess charges in composites based on polypropylene (PP) and the influence of oxide fillers, namely, BeO, $ZrO_2$, and $TiO_2$, on these properties.

## EXPERIMENTAL

Composite samples in the form of films with width of 200 ± 10 μm were obtained through hot pressing (under pressure of 15 MPa for 5 min at temperature 10–20°C higher than $T_{mp}$ of the polymer matrix) of premixed powders of the polymer and filler. The content of filler in the composite was up to 10–15 vol %. Powders of beryllium oxide and zirconium and titanium dioxides with sizes of $1 < d \leq 10$ μ served as fillers. These engineering ceramics are radiation-resistant [8]. The thermoluminescence investigations were carried out with a TLG-69M apparatus. The samples were irradiated at 77 K in tubes preevacuated at $1.3 \times 10^{-3}$ Pa using a $Co^{60}$ γ-irradiation source on a PXM-γ-25 setup.

## RESULTS AND DISCUSSION

Figure 1a shows the RTL curves of the samples of PP/BeO compositions at different contents of BeO. As can be seen, the typical β-relaxation peak of pure PP (curve *1*) at 267 ± 0.5 K shifts to the low-temperature region as the content of BeO increases. At the content of BeO in the composite φ = 10 vol %, the shift values reach 5–6 K. Another important peculiarity is the high-temperature region of the RTL curves, where a peak at 289–305 K, a shoulder at 320 ± 2 K, and a well-defined peak at ~410–420 K are observed. It is obvious that the intensity of these peaks rises as the content of BeO in PP increases. Moreover, the growth of luminous intensity at $T > 425$ K related to the filler is seen. The earlier

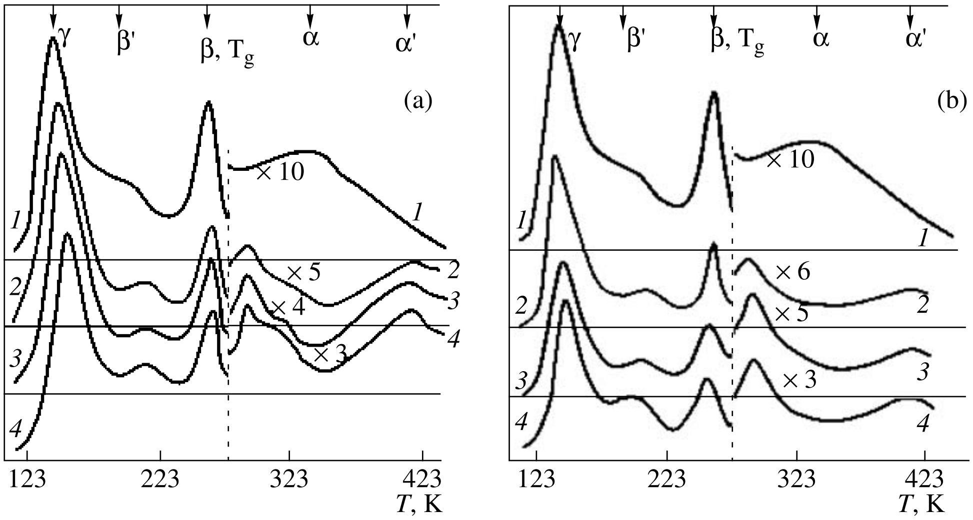

RTL spectra of PP/metal oxide compositions for different contents of (*a*) BeO and (*b*) $ZrO_2$: (*1*) PP; (*2*) 3%; (*3*) 5%; (*4*) 10%.

studies show [12] that the RTL curves of pure BeO contain typically four peaks at the temperatures of 155, 203, 276 (most intensive peak), and 290 K (small peak). However, according to the data from [9, 15], in the range of 77–300 K, the thermoluminescence curves are characterized by two main peaks at 155 and 290 K with the activation energies of 0.59 and 0.87 eV, respectively. As can be seen from Fig. 1a, for the PP/BeO compositions, the corresponding luminous peaks coincide with the luminescence zone of PP, associated with β-relaxation processes of the polymer, and in the temperature range of 250–290 K, they are connected with BeO. Also, as the content of BeO increases, the growth of the intensity of RTL luminescence in high-temperature regions at $T > 260$ K occurs in the composition. Moreover, at a temperature of 415 ± 2 K, there is a clear peak followed by decay of the luminescence intensity. According to [9, 15], the peak at 290 K with the activation energy 0.87 eV is associated with characteristic and heterovalent impurity defects in BeO and is concentrated in the band of 4.9 eV. In the case of the compositions, this RTL peak appears at 289 K, while its intensity grows as the volume content of BeO increases.

X-ray luminescence spectra of zirconium dioxide in the region of 300–750 nm contain a stepped peak at 389 nm, while under excitation with a UV laser (337 nm) the luminescence is observed in the region 450–520 nm [17]. Comparison of the obtained RTL spectra (Fig. 1b) with photo- and X-ray luminescence spectra, as well as with RTL spectra from the literature, shows that the nature and mechanism of these luminescences occurring under different excitation sources differ significantly. Apparently, the peaks at 289 ± 1 K and 412 K observed in the RTL spectra relate to the filler $ZrO_2$, and the high-temperature peaks are connected predominantly with PP. It is characteristic that introduction of $ZrO_2$ into PP leads to the decrease in $T_g$ (β-transition position) to low temperatures by 2–3 K, while the position of the most low-temperature peak shifts to the high-temperature region by 5–7 K. As the content of $ZrO_2$ in PP increases, the intensity of the peak at 285 K grows approximately in a linear fashion, and for this composition a high-temperature fuzzy peak is also observed. At the present time, the nature of these peaks is not well established. In our opinion, the most high-temperature and fuzzy peak at 410–415 K for these composites is associated with the processes occurring in an interphase layer of the polymer matrix with the filler. Analyzing the obtained RTL spectra of the composites, we can say that the peak reproduced at 289–290 K corresponds to the luminescence of the filler. It is our opinion that the peak at 319–320 K results from the luminescence in the surface traps of the composite, and the peaks reproduced at 413–415 K are likely the result of electron–ion processes proceeding in the interphase layer of the polymer matrix with the filler after excitation with γ irradiation. The table presents the activation energy values *W* corresponding to each luminescence peak of the polymer and composite. Calculation of *W* was performed both by the method of initial rates [6] and the method of partial peak half-width [20] using the following formula:

$$W = G_- \frac{kT_m(T_m - \Delta T_-)}{\Delta T_-},$$

where $G_- = 1.45$, $k = 1.38 \times 10^{-23}$ J/K, $\Delta T$ is the half-width of the luminescence peak in the region of intensity growth, and $T_m$ is the luminescence peak temperature.

As can be seen from the table, the increase in the filler content Φ leads to the reduction of the activation energy *W* of the corresponding relaxation process of PP. The observed reduction in *W* can be associated with the

Temperature range $\Delta T_{\max}$ and activation energy $W$ (eV) of the composites based on PP with different contents of fillers

| $T_{\max}$, $K$ | PP | 3% | | 5% | | 10% | |
|---|---|---|---|---|---|---|---|
| | | BeO | $ZrO_2$ | BeO | $ZrO_2$ | BeO | $ZrO_2$ |
| 197–213 | 0.155 | 0.17 | 0.12 | 0.10 | 0.10 | 0.10 | 0.10 |
| 259–264 | 0.68 | 0.55 | 0.66 | 0.45 | 0.39 | 0.37 | 0.28 |
| 289–305 | – | 0.34 | 0.28 | 0.325 | 0.29 | 0.26 | 0.26 |
| 315–341 | 0.19 | 0.38 | – | 0.37 | – | 0.18 | – |
| 413 ± 2 | – | 0.31 | 0.38 | 0.28 | 0.36 | 0.23 | 0.31 |

increase in overstrains in amorphous regions of PP. At low contents of the filler (5 vol %), the radiation cross-linking (at dose of $10^4$ Gy) causes a slow change in the activation energy $W$, and the filler play a structure-forming role.

The modifying effect of the fillers (both BeO and $ZrO_2$) on PP (estimated by the reduction of $T_g$ values of the polymer) can relate to the changes in supramolecular structure of the polymer (as the spherulite sizes decrease), as well as the reduction of internal overstrains. The compositions of PP with metal oxides such as $TiO_2$, ZnO, $ZrO_2$, $Al_2O_3$, and BeO are easily processed and have improved frost resistance (up to 250–253 K) [1, 2, 10–12]. The comparative data in Figs. 1a and 1b show that both fillers significantly affect the $\beta_1$ and β- and α-relaxation peaks in PP. In the case of the PP/BeO composition, there is also a significant change in RTL in the region of the α process, where the luminescence peak at 300–320 K is well defined (curves *2*–*4*). From Fig. 1a, it is apparent that this peak is intermediate between the α and β peaks of PP, i.e., it is closely related to the BeO filler.

Hence, introduction of fillers like BeO and $ZrO_2$ into PP leads to change in the intensity and temperature of realization of the $\beta^1$, β, α, and $\alpha^1$ peaks on the RTL curves, which can be used to predict the electroactive, dielectric, and physicomechanical properties of composites based on them.

## REFERENCES

1. Ivanyukov, D.V. and Fridman, M.L., *Polipropilen* (Polypropylene), Moscow: Khimiya, 1974, p. 272.
2. Gordienko, V.P., *Radiatsionnoe modifitsirovanie kompozitsionnykh materialov na osnove poliolefinov* (Radiation modification of composite materials based on polyolefins), Kiev: Naukova Dumka, 1985, p. 175.
3. Sadovnichii, D.N. et al., Radiatsionnaya electroprovodnost' polimernykh kompozitsii, napolnennykh dispersnymi oxidami (Radiation-Induced Conductivity of Polymer Compositions Filled with Dispersed Oxides), *Khim. Vys. Energii*, 2003, vol. 37, no. 6, pp. 436–441 [*High Energy Chem.* (Engl. Transl.), vol. 37, no.6, p. 389].
4. Magerramov, A.M., Lobanov, A.M. et al., Vliyanie vlagi na dielektricheskie svoistva pri sverkhvysokikh chastotakh vysokonapolnennykh kompozitakh na osnove polipropilena (Effect of Moisture on Dielectric Properties of High-filled Composites Based on Polypropylene under Super High Frequencies), *Plast. massy*, 1993, no. 5, pp. 19–21.
5. Godzhaev, E.M., Magerramov, A.M., Osmanova, S.S., and Nuriev, M.A., Zaryadovoe sostoyanie kompozitsii na osnove polietilena s poluprovodnikovym napolnitelem $TlInSe_2$ (Charge State of Compositions Based on Polyethylene with Semiconducting Filler $TlInSe_2$), *Elektronnaya obrabotka materialov*, 2007, no. 2, pp. 84–88.
6. Kuleshov, I.V. and Nikol'skii, V.G., *Radiotermolyuminestsentsiya polimerov* (Polymer Radiothermoluminescence), Moscow: Khimiya, 1991, p. 128.
7. Magerramov, A.M., Dashdamirov, M.K., Ismailov, I.M. et al., Radiotermolyuminestsentsiya elektroaktivnykh kompozitov polimer—p'ezokeramika (Radiothermoluminescence of Electroactive Composites based on Polymer–Piezoelectric Ceramics), *Izv. Bakinskogo Gos. Univ., ser. fiz.-mat. nauk*, 2006, no. 1, pp. 158–168.
8. Balkevich, V.L., *Tekhnicheskaya keramika* (Technical Ceramics), Moscow: Stroiizdat, 1984, p. 236.
9. Kruzhalov, A.V., Ogorodnikov, I.N., and Kudyakov, S.V., Izluchatel'naya relaxatsiya nizkoenergeticheskikh vozbuzhdenii I tochechnyi defekty v oxide berilliya (Radiative Relaxation of Low-energy Electron Excitations and Point Defects in Beryllium Oxide), *Izv. Vuzov, Fizika*, 1996, no. 11, pp. 76–93.
10. Dubnikova, I.L., Kedrina, N.F., Solov'eva, A.B. et al., Vliyanie prirody napolnitelya na kristallizatsiyu i mekhanicheskie svoistva napolnennogo polipropilena (The Effect of Filler Nature on the Crystallization Behavior and Mechanical Properties of Filled Polypropylene), *Vysokomol. Soed., Ser. A*., 2003, vol. 45, no. 3, pp. 468–475 [*Polymer Science, Ser. A* (Engl. Transl.), 2003, vol. 45, no. 3, pp. 281–286]
11. Magerramov, A.M., Akhmedov, F.I., Nuriev, M.A., and Bagirbekov, Kh.V., The Effect of γ-Irradiation on Dielectric Properties of Composites Based on Polyolefins with a BeO Filler, 6-aya Mezhdunarodnaya konferentsiya "Yadernaya i radiatsionnaya Fizika" (6th Int. Conf. "Nuclear and Radiation Physics"), Almaty, 2007, pp. 210–211.
12. Gadzhieva, N.N., Nuriev, M.A., and Magerramov, A.M., The Features of Radiothermoluminescence of the Thermally Processed Beryllium Oxide, *8th Int. Conf. "Solid St. Physics"*, Almaty, 2004, pp. 317–318.
13. Babin, P.A., Gavrilov, A.V., and Kozlenkova, N.A., The Luminescent Properties of Zirconium Oxide, *9-ya Mezhdunarodnaya konferentsiya "Fiziko-khimicheskie prot-*

*sessy v neorganicheskikh materialakh"* (9th Int. Conf. "Physical-chemical Processes in Inorganic Materials"), Kemerovo, 2004, vol. 1, pp. 330–331.

14. Aliev, M.M. and Zelenkova, E.A., The Effect of $ZrO_2$ Granules on UV Reflection Spectrum, *9-ya Mezhdunarodnaya konferentsiya "Fiziko-khimicheskie protsessy v neorganicheskikh materialakh"* (9th Int. Conf. "Physical-chemical Processes in Inorganic Materials"), Kemerovo, 2004, vol. 1, pp. 320–322.
15. Ogorodnikov, I.N., Kruzhalov, A.V., and Maslov, A.V., Osobennosti termostimulirovannoi lyuminestsentsii BeO v oblasti transformatsii avtolokalizovannykh exitonov (The peculiarities of Thermostimulated Luminescence of BeO in the Region of Transformation of Self-Trapped Exitons), *Zhurn. Tekh. Fiz.*, 1994, vol. 64, no. 3, pp. 100–108.
16. Ogorodnikov, I.N., Kirina, V.I., and Kruzhalov, A.V., Spontannaya emissiya BeO. Fluktuatsionnaya perestroika struktury (Spontaneous Emission of BeO. Fluctuation Reorganization of a Sctructure), *Zhurn. Tekh. Fiz.*, 1993, vol. 63, no. 5, pp. 70–80.
17. Chistoforova, N.V., Radzhabov, E.A., Yarovoi, P.N., and Es'kina, I.M., The Comparative Characteristics of Photo- and X-ray Luminescence of Oxide Fillers for Catalysts, *9-ya Mezhdunarodnaya konferentsiya "Fiziko-khimicheskie protsessy v neorganicheskikh materialakh"* (9th Int. Conf. "Physical-chemical Processes in Inorganic Materials"), Kemerovo, 2004, vol. 2, pp. 90–92.
18. Andrievskii, R.A. and Ragulya, A.V., *Nanostrukturnye materially* (Nanostructural Materials), Moscow, 2005.
19. Megarramov, A.M., Strukturnoe i radiatsionnoe modifitsirovanie elektretnykh, p'ezoelektricheskikh svoistv polimernykh kompozitov (Structure and Radiation Modification of Electret, Piezoelectric Properties of Polymer Composites), Baku: Elm, 2007, 325 p.
20. Gorokhovatskii, Yu.A. and Bordovskii, G.A., *Termoaktivatsionnaya tokovaya spektroskopiya vysokoomnykh poluprovodnikov i dielektrikov* (Thermoactivated Current Spectroscopy of High-resistant Semiconductors and Dielectrics), Moscow: Nauka, 1991, 248 p.